VSEBINA – CONTENTS

MATERIAL FAILURE OF AN AISI 316L STAINLESS STEEL HIP PROSTHESIS

NAPAKE MATERIALA V KOLČNI PROTEZI IZ NERJAVNEGA JEKLA AISI 316L

Matjaž Godec

Institute of Metals and Technology, Lepi pot 11, 1000 Ljubljana, Slovenia
matjaz.godec@imt.si

One of the major successes of modern surgery is the total replacement of joints by timplantation of prosthetic components by which the pain is relieved and deformity is corrected. The aseptic loosening of a prosthetic-joint component is the most common reason for joint-revision surgery. Furthermore, it is thought that wear particles are one of the major contributors to the development and perpetuation of aseptic loosening. It was ascertained that besides wear particles originated from polyethylene acetabular cup, the main reason of loosening hip prosthesis was due to the material failure. Based on stem material examination by different techniques it was found out that improper microstructure caused additional abrasion by hard particles and aseptic loosening took place.

Keywords: hip prosthesis, aseptic loosening, wear, stainless steel, polyethylene, non-metallic inclusions

Velik uspeh moderne kirurgije je med drugimi tudi popolna nadomestitev sklepov s protetičnimi nadomestki, s katerimi se omilijo bolečine in korigira deformacija. Pogosto pride do aseptičnega omajanja in potrebe po ponovni operaciji. Vzrok za to je ravno v obrabi in nastanku drobnih obrabnih delcev, ki večinoma vodijo do komplikacij in omajanja proteze. V raziskavi smo pokazali, da je poleg delcev, ki so izvirali iz polietilenske čašice bil glavni razlog omajanja ravno v napaki materiala. Na osnovi analize stebla materiala z različnimi tehnikami smo pokazali, da je neustrezna mikrostruktura povzročila dodatno abrazijo, zaradi trdih delcev in tako povzročila omajanje.

Ključne besede: kolčna, proteza, aseptično omajanje, obraba, nerjavno jeklo, polietilen, nekovinski vključki

1 INTRODUCTION

A total hip replacement is a surgical procedure whereby the diseased cartilage and bone of the hip joint is surgically replaced with artificial materials. An increasingly ageing population means that absolute numbers of people with a predilection for osteoarthritis is set to rise [1]. Hip joint replacement is usually done in people age 60 and older. It is expected that total hip replacement will increase due to population ageing.

Two types of arthroplasty are carried out nowadays with reference to mode of fixation; cemented und uncemented. Furthermore, two types of bearing surfaces have been utilised in total hip replacement. Hard-on-soft bearings have included couplings where the acetabular liner has been polyethylene (PE) and the femoral heads have been metallic, usually cobalt-chrome alloy, or ceramic. In order to assure lower abrasive wear and reduce the rate of aseptic loosening ceramic-on-ceramic or metal-on-metal bearing have been applied recently. There are three main materials used for implant stem: cobalt-chrome, stainless steel and titanium alloy. Although cobalt-chrome alloys are extensively used for manufacture of implants they have among good corrosion resistance and easily workability also some less desirable properties. One of them is high modulus of elasticity and not completely known long-term effects of metallosis arising from cobalt-chrome alloy [2,3]. Stainless steel is easy to work, has high strength and low price, however lower fatigue strength and tendency to corrosion cannot put it on the top [4–23]. One of the best is titanium alloy due to superior biocompatibility, relatively low elastic modulus and good corrosion performances [4,24–26]. However, it is softer than other metals and cannot be used for femoral heads due to wear [1].

Younger people who have a hip replaced may put extra stress on the artificial hip. That extra stress can cause it to wear out. The main cause of failure in these patients remains loosening due to osteolysis and the focus in future is going to be on extending the durability and survivorship of these components in a younger patient age group [1]. The aseptic loosening of a prosthetic-joint component is the most common reason for joint-revision surgery among all group of patient. However, there have been a few reported cases where a fracture of the stem neck has occurred, most likely due to the development of an inappropriate microstructure [27,28]. While abnormal wear at the bearing surface might give rise to excessive particle generation, the bone loss in relation to inflammation caused by these particles might in turn result in the loosening of the device and subsequent abnormal mechanical loading. In any case, wear particles are now considered to be one of the major contributors to the development and perpetuation of aseptic loosening [29]. Metal implants usually exhibit a low level of wear (40–100 times lower than ultra-high-

molecular-weight-polyethylene UHMWPE), a good surface finish and excellent mechanical properties. The drawbacks of metals are the metallic, electrochemical corrosion risks (low bio-compatibility) accelerated by the ions present in the body fluids and the presence of oxygen [2,4,5].

In the present study an AISI 316L stainless steel total hip prosthesis with unusual microstructure regarding the presence of non-metallic inclusions was investigated in order to find eventual connections with aseptic loosening and material microstructure.

2 EXPERIMENTAL DETAILS

A 63 years old male patient underwent total hip arthroplasty revision surgery due to aseptic loosening of both the femoral and acetabular components. The prosthesis was 106 months in use before exchange due to severe pain caused by loosening of stem. The femoral component was AISI 316L stainless steel stem (0.03 wt% C, 16–18 wt% Cr, 10–14 wt% Ni, 2–3 wt% Mo) and UHMWPE acetabular cup cemented with poly-methylmethacrylate (PMMA). The hip prosthesis was immediately cleaned, using only distilled water, after surgical removal. The specimens for the surface examination were cut from the hip stem and the polyethylene cup and cleaned in ethanol in an ultrasonic bath. The metal specimen for the microstructural examination was metallographically prepared by a standard procedure using 3 and 1 μm diamond polishing paste, and then etched by glyceregia to reveal the grain boundaries. The specimens for electron backscatter diffraction (EBSD) analyses were, after polishing, given an additional polish with colloidal silica oxide for 3 min and cleaned in ultrasonic bath. Furthermore, ion etching was performed in PECS 682 Gatan using 2,5 kV beam energy in rotation mode at 50° gracing angle. The specimens were analyzed using a light microscope Microphot FXA (Nikon) and with a FE-SEM JEOL JSM 6500F field-emission scanning electron microscope with attached EDX (an INCA X-SIGHT LN2 type detector, INCA ENERGY 450 software and an HKL Nordlys II EBSD camera using Channel5 software). For the EDX analysis, a 15 kV accelerating voltage and a probe current of 0.8 nA were used. The EBSD was performed at a 20 kV accelerating voltage and 2.7 nA probe current. The polyethylene specimen was covered with a 4 nm AuPd conductive layer for a subsequent SEM examination.

3 RESULTS AND DISCUSSION

After stainless steel (AISI 316L) total hip prosthesis had been surgical replaced, it was microscopically and spectroscopically examined. Polyethylene acetabular cup as well as stainless steel stem were studied together with the cement binder in order to find out the cause of its loosening (**Figure 1**). Bone cement (PMMA) is an

Figure 1: Hip prosthesis together with acetabular cup and residues of cement after being surgery removed
Slika 1: Kolčna proteza z acetabularno čašico in ostanki cementa po operaciji

excellent type of fixation for the hip prostheses, especially for elderly, relatively inactive patients who are usually also suffering from osteoporosis. During patient movement the wear between the polyethylene acetabular cup and the metallic head caused formation of very fine, irregularly shaped and elongated particles not longer than 1 μm. Furthermore, tribological activity of the acetabular cup and the metallic head caused tearing of larger particles from the inner acetabular cup wall. It is supposed that in overload situations adhesion caused conditions that part of the acetabular cup can be pulled out. As a result, the polished surface of the inner wall of the polyethylene acetabular cup with 300 μm deep cavities randomly distributed was formed (**Figure 2**) and consecutively looseness the hip joint.

Accurate stainless stem surface examination showed that original rough surface, caused by sand-blasting as a last step in manufacturing process of the stem, in some areas transformed into smooth surface with some rough islands residues. During this process the metallic particles and ions accumulate in the body tissues and fluids. Debonding between the cement and implant might reduce the life-time of the implant fixation. Small

Figure 2: Surface modification of the polyethylene acetabular cup's inner wall with deep cavities, SE image
Slika 2:. Sprememba površine polietilenske čašice z globokimi jamicami, SE slika
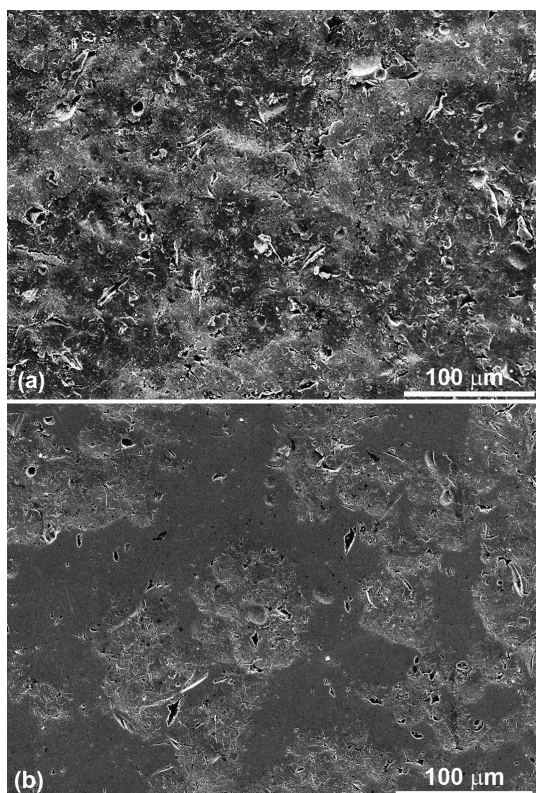
Figure 3: (a) Original sand blasted surface, SE image; (b) surface modification due to wear process, SE image
Slika 3: (a) Originalna površina po peskanju, SE slika; (b) sprememba površine zaradi obrabe, SE slika
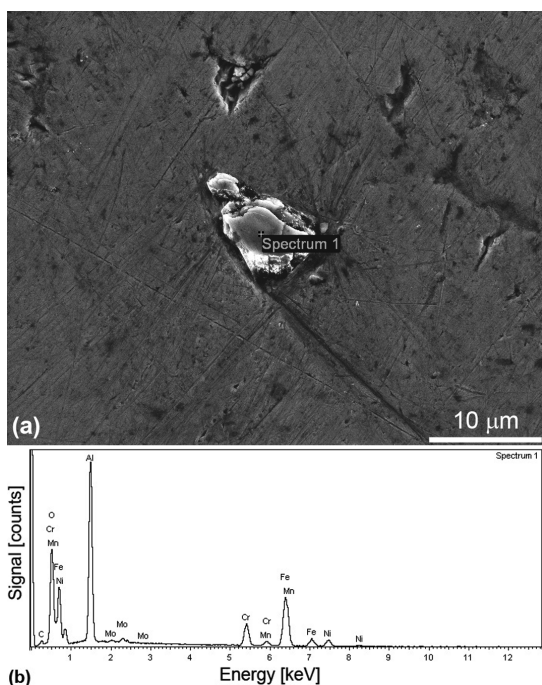
Figure 4: (*a*) SE image of alumina particle due to residue of surface sand blasting with marked spot of the EDX analysis; (*b*) EDX spot analysis of an alumina particle
Slika 4: (a) SE slika aluminijevega oksida, ki je ostal na površini po peskanju, z označenim mestom EDX analize, (b) EDX točkovna analiza aluminijevega oksida
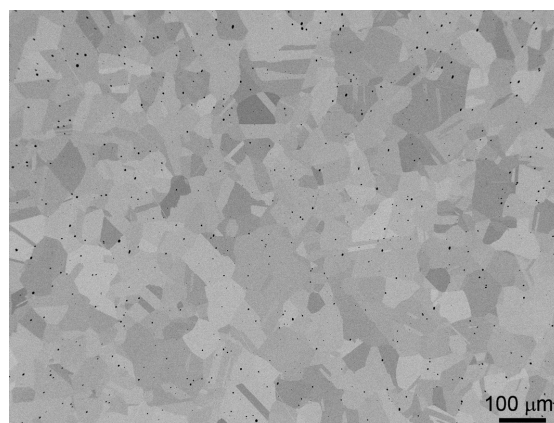
Figure 5: Microstructure of stem specimen showing plenty of Al$_2$O$_3$ non-metallic inclusions, BE image
Slika 5: Mikrostruktura vzorca stebla, ki prikazuje veliko Al$_2$O$_3$ nekovinskih vključkov, BE slika
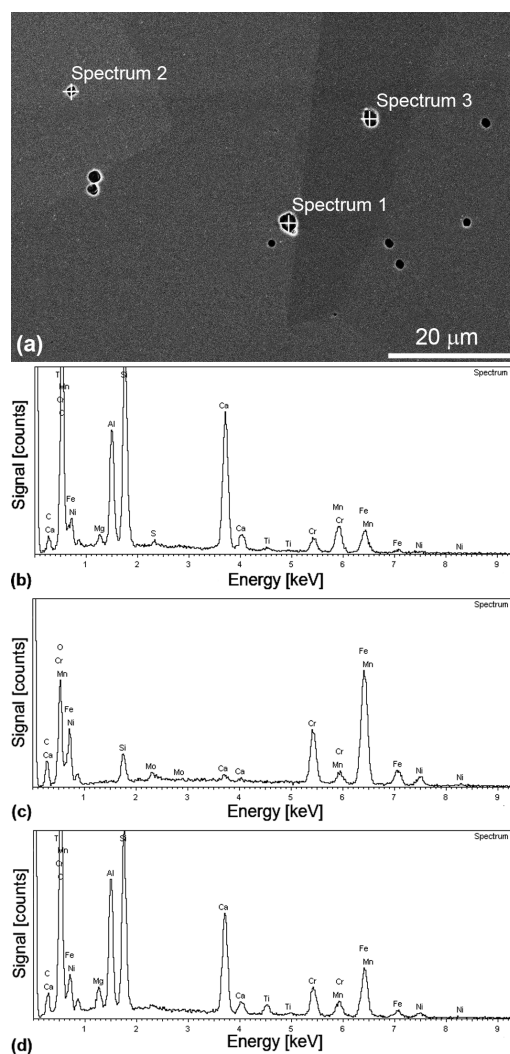
Figure 6: EDX spot analysis, (a) SE image of stem specimen with marked spots of EDX analysis, (b), (c) and (d) EDX spot analysis of non-metallic inclusions
Slika 6: EDX točkovna analiza stebla, (a) SE slika stebla z označenimi mesti EDX analize, (b), (c) in (d) EDX točkovne analize nekovinskih vključkov
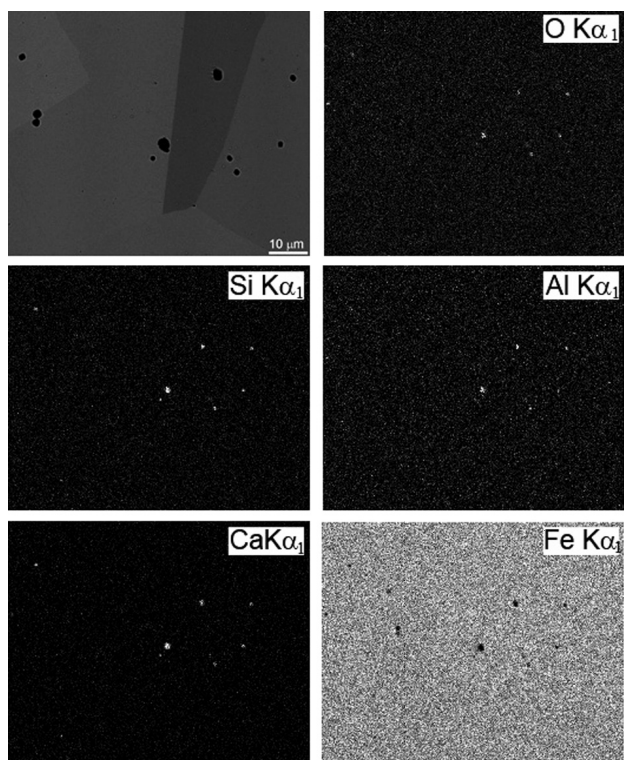
Figure 7: EDX mapping, (a) BE image of stem specimen with corresponding EDX images of (b) O Kα_1, (c) Si Kα_1 (d) Al Kα_1, Ca Kα_1 and Fe Kα_1
Slika 7: EDX ploskovna analiza, (a) BE slika vzorca stebla s pripadajočimi EDX slikami (b) O Kα_1, (c) Si Kα_1 (d) Al Kα_1, Ca Kα_1 in Fe Kα_1

cement fractures are thought to play a significant role in the initiation of the cement failure [1]. The prevailing stress between the stem and the cement is mostly caused by shear, whereas compressive-stress occurs in aceta-bulum, especially among active patients. The wear particles from the cement, the metal and the polyethylene (PE) are claimed to play a major role in the aseptic loosening. Osteolysis without any signs of infection is
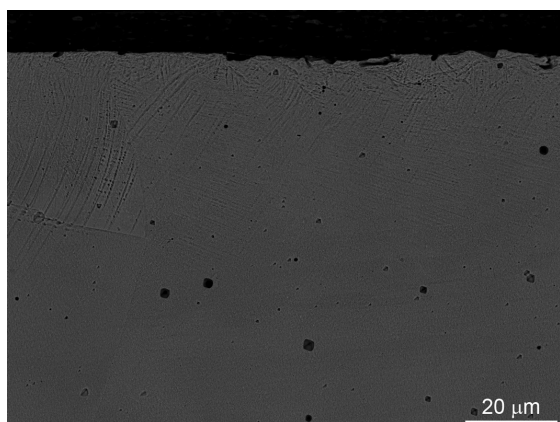
Figure 8: BE image of hip stem microstructure close to the surface with the slip lines due to surface deformation by sand-blasting
Slika 8: BE slika mikrostrukture stebla blizu površine z drsnimi črtami, zaradi deformacije povzročene s peskanjem
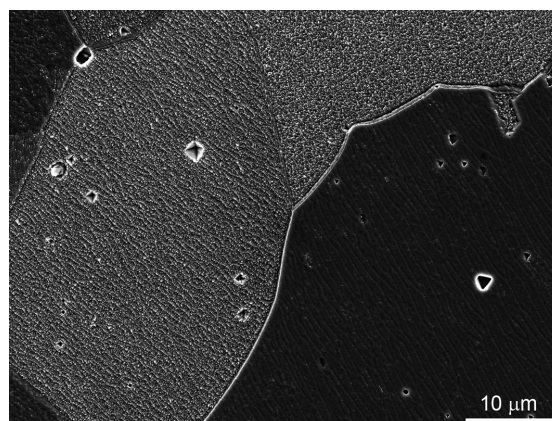
Figure 9: SE image of stem microstructure consist of austenite grains. Grain boundaries are free of any carbides and other phases. Etched by glyceregia
Slika 9: SE slika avstenitne mikrostrukture stebla. Na mejah ni karbidov in ostalih faz. Jedkano z zlatotopko

mostly related to release of PMMA debris in the tissues by micro-motion which initiates the cement failure. As a consequence a foreign-body reaction occurs and initiates osteolysis and finally leads to loosening. Once metallic particles are formed by wear, the new particles will be generated by friction and apart from causing a mild foreign-body reaction, such a metals debris can be involved in the process of aseptic loosening mostly due to cytoxine release from macrophages.

Analysed stainless steel stem indicated some of the surface areas not affected by wear while some parts of stem underwent significant changes due to wear process. **Figure 3 (a)** shows original sand blasted surface and **Figure 3(b)** demonstrated the surface which was
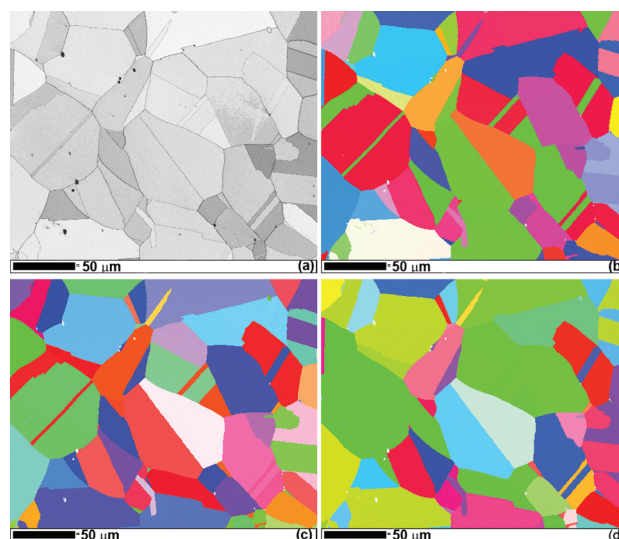
Figure 10: EBSD mapping (a) band contrast image (b) inverse pole figure in X direction, (c) inverse pole figure in Y direction, (c) inverse pole figure in Z direction
Slika 10: EBSD ploskovna analiza (a) slika kvalitete uklona (b) inverzna polova figura v X smeri, (c)) inverzna polova figura v Y smeri, (c) inverzna polova figura v Z smeri

exposed to wear process. Rougher surface had plenty of small mechanically produced pits visible at a higher magnification. There were also plenty of Al_2O_3 particles embedded in the material most likely due to sand blasting procedure in order to make the surface rougher and easier for bone tissue to grow into. Al_2O_3 particles were detected by EDX in the stem surface (**Figure 4**).

Stainless steel stem microstructure across whole inner and outer part of implant had plenty of non-metallic inclusions (**Figure 5**). The inclusions were analysed by EDX. The inclusions were combinations of Al_2O_3, SiO_2 and CaO particles and were consequences of problems during steel making. The presence of non-metallic oxide inclusions is a major cause of incompatibility between the attainable and desirable level of cleanliness in many grades of commercial steel. Generally, inclusions degrade the mechanical properties of the steel and thereby reduce the ductility of the cast metal and increase the risk for mechanical and/or corrosion failure of the final product. The number of these inclusions was too large for the AISI 316L steel grade particularly in an orthopaedic application. Oxide inclusions originate from two sources: (a) residual products resulting from intentionally added alloying elements to deoxidize the molten steel after oxygen treatment (endogenous or micro inclusions); (b) products resulting from reactions between the melt and atmosphere, slag, or refractory (exogenous or macro inclusions) [30]. Alumina inclusions occur as deoxidation products in the aluminum-based desoxidation of steel. Most grades of steel are treated with calcium using Ca-Si alloy is certain amount of silicon is permitted in steel. During calcium treatment, the alumina and silica inclusions are converted to molten calcium aluminates and silicate which are globular in shape because of the surface tension effect. The change in inclusion composition and shape is known as the inclusion morphology control. However, such high amount of that type of inclusions is an evidence of wrong desoxidation process. The size of inclusions was from less than 1 μm and up to 5 μm. **Figures 6** and **7** show EDX spot analyses and mapping of such inclusions, respectively. There were some pure Al_2O_3 as well as pure SiO_2, but most of them were combination of both with additional CaO content. During conventional metallographic sample preparation due to water presence a part of calcium inclusions might be lost. If calcium inclusions are of high interest of study the ion etching (cross-section polisher) or some similar techniques shall be used.

Stem microstructure consist of pure austenite phase. No other phases as delta ferrite, sigma phase and chi phase were observed and detected in the microstructure even though the specimens were etched or colloidal silica polished and observed by EBSD. Only in the very surface region in cross-section mode it was possible to observe slip lines caused by sand-blasting deformation (**Figure 8**). If deformation is enough high the defor-

mation martensite will take place. Such a microstructure is usually not desirable.

In some cases the formation of stress-induced martensite might lead to micro-crack formation, which, especially in combination with intercrystalline corrosion, leads to material fracture in overload situations [31]. Due to the low carbon content in the examined steel, the possibilities of intercrystalline corrosion are negligible in contrast to the stainless steels with a higher carbon content, where $Cr_{23}C_6$ carbides along the grain boundaries are formed. **Figure 9** shows grain boundary between two of austenite grains. The grain boundary was free of any carbide. EBSD was performed in order to find out any possible presence of other unwanted phases in stainless steel grades. However, the technique was primarily developed for texture analyses, but nowadays it is used for phase analyses, misorientation measurements as well as strain and stress detection [32–38]. **Figure 10** shows results of EBSD measurements. Band contrast (BC) image sometimes referred as pattern quality image and can tell us a lot of microstructure details mostly impossible revealed by chemical etching because of EBSD being a very surface sensitive techniques. Band contrast image of analysed sample (**Figure 10 (a)**) very precisely revealed all of those non-metallic inclusions based on aluminium, silicon and calcium oxides[39]. Unfortunately, it was almost impossible to obtain sufficiently good Kikuchi pattern for indexing it. Therefore, in EBSD map the only iron FCC crystal lattice was considered. All three inverse pole figure (IPF) images in X, Y and Z direction were performed. Analysed steel had no texture and had equiaxed austenite grains. Because of forging of stem part and further annealing it is expected to have such microstructure.

4 CONCLUSIONS

Shortly after total hip surgical replacement septic loosening might occur due to several reasons. If this is not about to happen the patient has good chances to undergo recovery successfully. However, after several years usually due to the process of adhesive and abrasive wear as well as to wear polishing, polyethylene and metallic debris occurs in between polyethylene acetabular cup and metallic ball as well as in between stainless steel stem and cement bond in the case of cemented prostheses. Based on the investigation performed on an AISI 316L stainless steel hip prosthesis it was found that in the present case wear polishing and adhesive wear played an important role. Acetabular cup areas exposed to adhesive wear had rough regions where larger pieces were pulled out while wear polishing of the polyethylene acetabular cup caused a very smooth, glossy-like appearance of the surface. Wear polishing of the femoral stem was observed to occur unevenly over the stem surface. Certain areas were higher exposed to wear and are seemed to be more curved part. The wear

polishing of the surface caused a loss of material from the surface of the implant, the formation of metallic particles and the possibility of metal-ion formation. The AISI 316L stainless steel microstructure is austenitic with typical twin grain boundaries but with no other usually unwanted phases. Also no carbides at grain boundaries were found. But an unusually large number of aluminium-silicon-calcium based non-metallic inclusions were detected. Such high amount of that type of inclusions is an evidence of wrong desoxidation process during steel production. However, the number of these inclusions is too large for the AISI 316L steel grade especially in an orthopaedic application. Furthermore, Al_2O_3 particles due to sand-blasting were found in the surface. The long-term wear polishing strengthened by hard Al_2O_3 particles in the surface and as such might digs out hard non-metallic inclusions as well and thus complementing the wear-polishing mechanism with abrasive wear. Usually the loosening of the components is triggered by the micromotion of cemented components which causes the abrasion of the implant's surface, producing metal-wear debris and a proliferative soft-tissue reaction. Based on case study investigation it is no doubt that such a bad quality stainless steel by huge amount of hard non-metallic inclusions accelerating the loosening process much faster due to potentially toxic and human body irritating debris formed during wear.

Acknowledgments

5 REFERENCES

[1] S. B. Mirza, D. G. Dunlop, S. S. Panesar, S. G. Naqvi, S. Gangoo, S. Salih, The Open Orthopaedics Journal, 4 (**2010**), 169–180

[2] A. Kocijan, I. Milosev, B. Pihlar, Journal of Materials Science-Materials in Medicine 15 (**2004**), 643–650

[3] A. Kocijan, I. Milosev, D. K. Merl, B. Pihlar, Journal of Applied Electrochemistry 34 (**2004**), 517–524

[4] A. Minovic, I. Milosev, V. Pisot, A. Cor, V. Antolic, Journal of Bone and Joint Surgery-British Volume 83B (**2001**), 1182–1190

[5] A. Kocijan, I. Milosev, B. Pihlar, Journal of Materials Science-Materials in Medicine 14 (**2003**), 69–77

[6] A. Kocijan, C. Donik, M. Jenko, Corrosion Science 49 (**2007**), 2083–2098

[7] D. Mandrino, M. Lamut, M. Godec, M. Torkar, M. Jenko, Surface and Interface Analysis 39 (**2007**), 438–444

[8] M. Torkar, M. Godec, M. Lamut, Engineering Failure Analysis 14 (**2007**), 1218–1223

[9] D. Mandrino, M. Godec, A. Kocijan, M. Lamut, M. Torkar, M. Jenko, Metalurgija 47 (**2008**), 119–123

[10] D. Mandrino, M. Godec, M. Torkar, M. Jenko, Surface and Interface Analysis 40 (**2008**), 285–289

[11] C. Donik, A. Kocijan, J. T. Grant, M. Jenko, A. Drenik, B. Pihlar, Corrosion Science 51 (**2009**), 827–832

[12] C. Donik, A. Kocijan, D. Mandrino, I. Paulin, M. Jenko, B. Pihlar, Applied Surface Science 255 (**2009**), 7056–7061

[13] C. Donik, A. Kocijan, I. Paulin, M. Jenko, Mater. Tehnol. 43 (**2009**), 137–142

[14] A. Kocijan, C. Donik, M. Jenko, Mater. Tehnol. 43 (**2009**), 195–199

[15] A. Kocijan, C. Donik, M. Jenko, Mater. Tehnol. 43 (**2009**), 39–42

[16] C. Donik, D. Mandrino, M. Jenko, Vacuum 84 (**2010**), 1266–1269

[17] C. Donik, I. Paulin, M. Jenko, Mater. Tehnol. 44 (**2010**), 67–72

[18] M. Godec, A. Kocijan, D. Dolinar, D. Mandrino, M. Jenko, V. Antolic, Biomedical Materials 5 (2010), sp. iss.

[19] L. Akesso, M. Pettitt, J. Callow, M. Callow, J. Stallard, D. Teer, C. Liu, S. Wang, Q. Zhao, F. D'Souza, P. Willemsen, G. Donnelly, C. Donik, A. Kocijan, M. Jenko, L. Jones and P. Guinaldo, Biofouling 25 (**2009**), 55–67

[20] A. Kocijan, M. Conradi, Materiali in Tehnologije 44 (**2010**), 21–24

[21] D. Mandrino, C. Donik, M. Jenko, Surface and Interface Analysis 42 (**2010**), 762–765

[22] A. Kocijan, D. K. Merl, M. Jenko, Corrosion Science 53 (**2011**), 776–783

[23] D. A. Skobir, M. Jenko, D. Mandrino, Surface and Interface Analysis 36 (**2004**), 941–944

[24] L. Milosev, V. Antolic, A. Minovic, A. Cor, S. Herman, V. Pavlovcic, P. Campbell, Journal of Bone and Joint Surgery-British 82B (**2000**), 352–357

[25] I. Milosev, A. Minovic, Annali Di Chimica 91 (**2001**), 343–354

[26] I. Paulin, D. Mandrino, C. Donik, M. Jenko, Mater. Tehnol. 44 (**2010**), 73–76

[27] S. Griza, M. Reis, Y. Reboh, A. Reguly, T. R. Strohaecker, Engineering Failure Analysis 15 (**2008**), 981–988

[28] J. Chao, V. Lopez, Engineering Failure Analysis 14 (**2007**), 822–830

[29] C. Kaddick, I. Catelas, P. H. Pennekamp, M. A. Wimmer, Orthopade 38 (**2009**) 690

[30] M. Godec, L. Kosec, M. Jenko, R. Mast, H. J. Grabke, Metall 51 (**1997**), 702–705

[31] M. Torkar, Engineering Failure Analysis 13 (**2006**), 624–628

[32] M. Godec, D. Mandrino, B. Sustarsic, D. Nolan, M. Jenko, Surface and Interface Analysis 40 (**2008**), 498–502

[33] M. Godec, B. Sustarsic, M. Jenko, Metalurgija 47 (**2008**), 9–12

[34] D. A. Skobir, M. Godec, M. Jenko, B. Markoli, Surface and Interface Analysis 40 (**2008**), 513–517

[35] B. S. Batic, M. Jenko, Surface and Interface Analysis 42 (**2010**), 703–706

[36] D. A. Skobir, M. Godec, A. Nagode, M. Jenko, Surface and Interface Analysis 42 (**2010**), 717–721

[37] B. S. Batic, M. Jenko, Journal of Vacuum Science & Technology A 28 (**2010**), 741–744

[38] V. Randle, International Materials Reviews 49 (**2004**), 1–11

[39] M. Kosec, D. Murko, J. Holc, B. Malič, M. Čeh, T. Hauke, H. Beige, Zeitschrift fur Metallkunde 92 (**2001**), 8

A COMPARISON OF THE CORROSION BEHAVIOUR OF AUSTENITIC STAINLESS STEELS IN ARTIFICIAL SEAWATER

PRIMERJAVA KOROZIJSKIH LASTNOSTI AVSTENITNIH NERJAVNIH JEKEL V SIMULIRANI MORSKI VODI

Aleksandra Kocijan

Institute of Metals and Technology, Lepi pot 11, SI-1000 Ljubljana, Slovenia
aleksandra.kocijan@imt.si

The evolution of the passive films formed on AISI 317LNM and AISI 316L stainless steels in artificial seawater was studied using the electrochemical techniques of cyclic voltammetry and potentiodynamic measurements. The extent of the passive range increased significantly for the AISI 317LNM stainless steel compared to the AISI 316L in the investigated solution. The cyclic voltammograms of the AISI 317 LMN and AISI 316L were recorded in artificial seawater. The current-density peaks formed during the cyclic voltammetry were ascribed to the corresponding electrochemical processes taking place on the surface of the investigated materials, and the influence of the potential scan rate was also studied. The current density of the peaks increased linearly with the scan rate. The potentials of the anodic and cathodic peaks moved slightly, with the increasing scan rate, towards more positive and negative values, respectively.

Keywords: stainless steel, sea water, chloride, cyclic voltammetry, potentiodynamic measurements

Z elektrokemijskimi tehnikami ciklične voltametrije in potenciodinamskih meritev smo raziskovali tvorbo pasivne plasti na površini nerjavnih jekel AISI 317LNM in AISI 316L v raztopini simulirane morske vode. Širina pasivnega območja je pri nerjavnem jeklu AISI 317 LMN bistveno večja kot pri AISI 316L v preiskovani raztopini. S ciklično voltametrijo smo opisali nastale vrhove s procesi, ki potekajo na površini preiskovanih vzorcev. Raziskovali smo tudi vpliv spreminjanja potenciala s časom na obliko cikličnih voltamogramov. Ugotovili smo, da z naraščajočo hitrostjo spreminjanja potenciala s časom prihaja do rahlega naraščanja in premika vrhov.

Ključne besede: nerjavno jeklo, morska voda, kloridi, ciklična voltametrija, potenciodinamske meritve

1 INTRODUCTION

The austenitic stainless steel AISI 316L is one of the most commonly used materials. Its mechanical properties, such as ductility and wear resistance, make it attractive for particular applications. The corrosion resistance of stainless steel is relatively good. However, it is challenged by the hostile environment in marine applications, as it is susceptible to localised corrosion in environments containing chloride [1].

The austenitic stainless steel AISI 317LNM is a nitrogen-alloyed austenitic stainless steel with a high molybdenum addition. It exhibits an austenitic microstructure free of deleterious carbide precipitations at the grain boundaries. The grade contains some residual ferrite, up to 2 % after solution annealing at temperatures 1100–1150 °C and water quenching. Its low carbon content avoids the intergranular corrosion, even on welded pieces without an ulterior water quenching. The high molybdenum content gives this steel a higher resistance to corrosion in chloride-containing environments than standard grades, i.e., AISI 316L. Nitrogen additions and a low silicon content have a stabilizing effect on the austenitic structure, reducing the precipitation of inter-metallic phases during welding. The nitrogen addition also increases the yield strength com-

pared to AISI 317L. Its main properties are a high ductility, an easy weldability and a high corrosion resistance. The main applications are chemical and petrochemical applications, pollution control equipment and chemical tankers [2].

Several techniques have been used to study the corrosion behaviour of stainless steels in different media [1,3–27]. The behaviour of AISI 316L stainless steel in chloride-containing solutions has been studied by various authors [28–31]. Platt et al. [28] compared the corrosion behaviour of 2205 duplex stainless steel and AISI 316L in a 0.9 % chloride solution. Electrochemical testing indicated that the 2205 duplex stainless steel had a wider passivation range than the AISI 316L. Blanco et al. [29] investigated the corrosion behaviour of two traditional austenitic stainless steels in reinforced concrete structures exposed to highly chloride-contaminated atmospheres. The effects of ion nitriding on the corrosion performance of a 316L stainless steel were evaluated in a 0.9 % sodium chloride solution by Gil et al. [30]. It was shown that an ion nitriding treatment in a 25 % N_2–75 % H_2 atmosphere performed at a temperature of 410 °C improves the surface hardness of the AISI 316L stainless steel. However, under the experimental conditions carried out in this research, the nitrided steel is as prone to localized corrosion as the untreated one. It is consi-

dered that this behaviour is mainly due to the presence of CrN, which precipitates during processing, contributing to the depletion of chromium from the adjacent matrix and leading to a galvanic corrosion mechanism. Hryniewicz et al. [31] compared the corrosion behaviour of austenitic stainless steels after two electropolishing processes carried out in the absence and presence of a magnetic field. It has been shown that the proposed magnetic field process shifts the corrosion potentials in the direction of greater corrosion resistance.

The influence of artificial seawater on the corrosion properties of AISI 317LMN stainless steel has not been investigated extensively. Among the more recent work, only one paper concerning the corrosion resistance of AISI 317LMN stainless steel for an application in pre-stressed concrete structures was published [2].

In the present work AISI 317LMN stainless steel and AISI 316L stainless steel were studied in artificial seawater. The study was conducted using the electrochemical techniques of cyclic voltammetry and potentiodynamic measurements.

2 EXPERIMENTAL

AISI 317 LMN stainless steel and AISI 316L stainless steel were investigated. Their compositions were confirmed by analytical chemical methods, as shown in **Table 1**. The concentrations of Cr, Ni, Mn and Mo were determined by using inductively coupled plasma atomic emission spectroscopy (ICP-AES, ICP-AES Perkin Elmer Optima 3100 RL instrument), the concentration of Si was determined gravimetrically (Mettler H35AR balance). A spectrophotometric method using the bismuth phosphomolybdate complex was applied for the determination of phosphorus. A blue complex formed was extracted with methyl isobutyl ketone. The absorbance was measured at 625 nm (Opton PM 6 spectrophotometer). The concentration of carbon was determined by the oxidation of the sample in an induction furnace by heating in an oxygen atmosphere to form CO_2, which was then measured with an infrared detector (Eltra CS-800 instrument). The measuring principle is based on the infrared-radiation-absorbing properties of the gases. In the case of the nitrogen determination the sample was melted at high temperatures up to 3000 °C in an electrically heated graphite crucible in the furnace. The concentration of nitrogen was determined with a thermal conductivity detector (Eltra ON-900 instrument).

The experiments were carried out in artificial seawater with a composition of 3.5 % NaCl (Merck, Darmstadt, Germany).

The test specimens were cut into discs of 15 mm diameter. The specimens were ground with SiC emery paper down to 1000 grit prior to the electrochemical studies, and then rinsed with distilled water. The specimens were then embedded in a Teflon PAR holder and employed as a working electrode. The reference electrode was a saturated calomel electrode (SCE, 0.242 V vs. SHE) and the counter electrode was a high-purity graphite rod.

The cyclic voltammetry and potentiodynamic measurements were recorded using an EG&G PAR PC-controlled potentiostat/galvanostat Model 273 with M252 Softcorr III computer programs. In the case of potentiodynamic measurements the specimens were immersed in the solution 1 h prior to the measurement in order to stabilize the surface at the open-circuit potential. The potentiodynamic curves were recorded, starting at 250 mV more negative than the open-circuit potential. The potential was then increased, using a scan rate of 1 mV/s, until the transpassive region was reached.

3 RESULTS AND DISSCUSION

The potentiodynamic behaviour of AISI 317LMN and AISI 316L stainless steels in artificial seawater is shown in **Figure 1**. The differences in the alloys' compositions affected the polarisation and the passivation behaviours of the tested materials. After 1 h of stabilization at the open-circuit potential, the corrosion potential (E_{corr}) for the AISI 317LMN in the artificial seawater was approximately –0.29 V. Following the Tafel region, the alloy exhibited a broad range of passivation. The breakdown potential (E_b) for the AISI 317LMN in artificial seawater was approximately 1.2 V. In the case of the AISI 316L, the E_{corr} in the artificial seawater was essentially the same as in the case of AISI 317LMN. The range of passivation was significantly narrowed compared to the AISI 317LMN specimen and the E_b was 0.20 V. The corrosion-current densities in the passive range were similar for both the tested specimens.

The cyclic voltammograms of the AISI 317LMN and AISI 316L recorded in the artificial seawater enabled us to ascribe the current-density peaks to the corresponding electrochemical processes taking place on the surface of the investigated materials, and the influence of the potential scan rate (v) was also studied (**Figures 2 and 3**). The cyclic voltammograms were recorded for the

Table 1: The composition of AISI 317LMN and AISI 316L stainless steels in mass fractions, $w/\%$
Tabela 1: Kemijska sestava nerjavnih jekel AISI 317LMN in AISI 316L, masni delež, $w/\%$

	w(Cr)	w(Ni)	w(Mn)	w(Si)	w(P)	w(S)	w(C)	w(Mo)
AISI 316L	17.00	10.00	1.40	0.38	0.041	< 0.005	0.021	2.10
AISI 317 LMN	17.33	12.82	1.64	0.39	0.027	< 0.0005	0.014	4.06
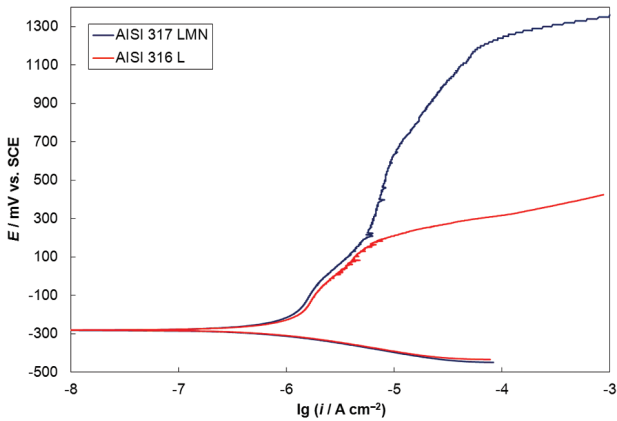
Figure 1: Polarisation curves recorded for AISI 317LMN and AISI 316L stainless steel in 3.5 % NaCl
Slika 1: Polarizacijske krivulje za nerjavni jekli AISI 317LMN in AISI 316L v 3,5-odstotni raztopini NaCl

AISI 316L and AISI 317LMN at different scan rates, in the potential ranges from –1.0 V to 0.4 V and 1.2 V, respectively. In the presence of the artificial seawater four peaks are observed in the cyclic voltammogram for the AISI 317 LMN (**Figure 2**). The first anodic peak A1 at a potential of –0.6 V can be ascribed to the electro-formation of Fe(II) oxide upon the Cr(III)-containing passivating layer, existing on the electrode at such negative potentials according to the reaction: $Fe + H_2O$ $\Leftrightarrow FeO + 2H^+ + 2e^-$ [32]. The second anodic peak A2 at the potential of –0.1 V is ascribed to the oxidation of the Fe(II) species to the Fe(III) species according to the reaction: $2Fe^{2+} + 3H_2O \Leftrightarrow Fe_2O_3 + 6H^+ + 2e^-$ [32]. This is followed by the narrow region with a constant current density, up to 0.5 V, where the current density starts to increase and the transpassive region is reached. In that region the transpassive oxidation of the Cr(III) species to the Cr(VI) species occurs, the Ni(II) species formed
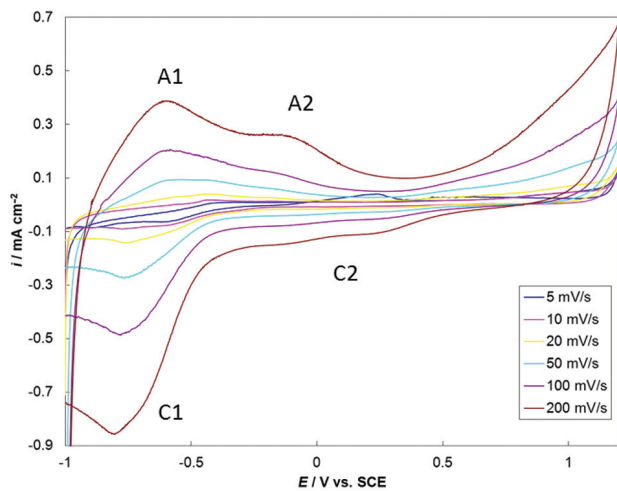
Figure 2: Cyclic voltammograms recorded for AISI 317LMN stainless steel with increasing scan rate in 3.5 % NaCl
Slika 2: Ciklični voltamogrami za nerjavno jeklo AISI 317LMN v 3,5-odstotni raztopini NaCl z naraščajočo hitrostjo spreminjanja potenciala s časom
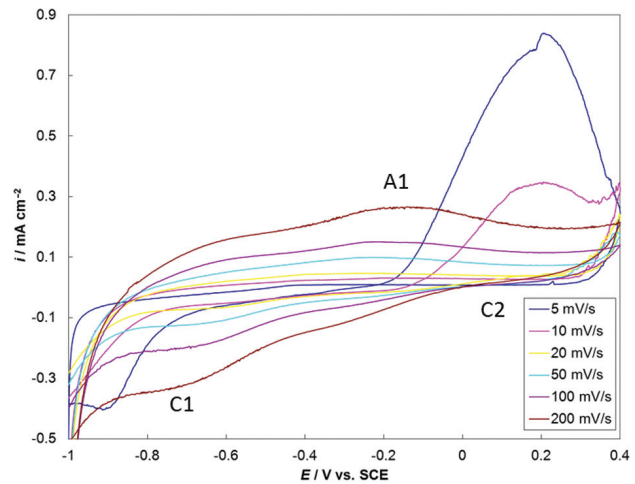
Figure 3: Cyclic voltammograms recorded for AISI 316L stainless steel with increasing scan rate in 3.5 % NaCl
Slika 3: Ciklični voltamogrami za nerjavno jeklo AISI 316L v 3,5-odstotni raztopini NaCl z naraščajočo hitrostjo spreminjanja potenciala s časom

during the passivation process might have been oxidised to Ni(IV) oxide (NiO_2) in this potential range, too [32]. In the reduction cycle in the potential range of peak C2 at 0.2 V the Cr(VI) is reduced to Cr(III) and the iron oxide-hydroxide layer is largely reduced in the potential range of the peak C1 at a potential of –0.8 V [20].

In the case of the AISI 316L in artificial seawater (Figure 3), the anodic peak at a potential of –0.1 V is observed in the cyclic voltammograms and can be ascribed to the electro-formation of Fe(II) oxide. After the passive region the range of the transpassive oxidation is reached at a potential of 0.35 V. In the case of slower scan rates, i.e., 5–10 mV/s, a hysteresis is formed in the reverse cycle, indicating the pronounced dissolution of the oxide layer formed at higher potentials. In the reduction cycle both peaks are less evident on that scale; however, in the potential range of peak C2 at 0.2 V the Cr(VI) is reduced to Cr(III) and the second peak in the cathodic cycle at –0.7 V corresponds to the reduction of the iron oxide-hydroxide layer.

The influence of the scan rate on the oxidation-reduction processes for both investigated materials in cyclic voltammograms is also presented in **Figures 2 and 3**. The current density of the anodic and cathodic peaks increases linearly with the scan rate. The potentials of the anodic and cathodic peaks move slightly, with the increasing scan rate, towards more positive and negative values, respectively.

4 CONCLUSIONS

The corrosion behaviours of the AISI 317LMN and AISI 316L stainless steels were studied in artificial seawater. The study was conducted using the electro-chemical techniques of cyclic voltammetry and potentio-dynamic measurements.

The potentiodynamic measurements showed the superior corrosion stability of AISI 317 LMN stainless steel in comparison to AISI 316L stainless steel. The range of passivation was significantly broader for the AISI 317LMN compared to the AISI 316L specimen. The corrosion-current densities in the passive range were similar for both the tested specimens.

The cyclic voltammograms revealed the similar electrochemical behaviour of both the tested materials in the presence of the artificial seawater, although in a different potential range. In the case of the AISI 317LMN stainless steel, four peaks were observed corresponding to the electro-formation of the Fe(II) and Fe(III) species, and subsequently to the reduction of Cr(VI) to Cr(III) oxide and the reduction of the iron oxide-hydroxide layer. In the case of the AISI 316L stainless steel the anodic peak was ascribed to the electro-formation of Fe(II) oxide. In the cathodic cycle the reduction of Cr(VI) and the reduction of the iron oxide-hydroxide layer occurs, similar to the results for the AISI 317LMN stainless steel.

The results of the present study show that the electrochemical characteristics of AISI 317LMN and AISI 316L stainless steel are similar. However, the corrosion resistance of AISI 317LMN stainless steel under the investigated conditions is superior compared to AISI 316L, which indicates the possibilities of its application in a marine environment.

5 REFERENCES

[1] C. Donik, I. Paulin, M. Jenko, Mater. Tehnol., 44 (**2010**), 67–72

[2] Y. Wu, U. Nurnberger, Materials and Corrosion-Werkstoffe Und Korrosion, 60 (**2009**), 771–780

[3] A. Kocijan, C. Donik, M. Jenko, Corrosion Science, 49 (**2007**), 2083–2098

[4] A. Kocijan, M. Conradi, Mater. Tehnol., 44 (**2010**), 21–24

[5] D. Mandrino, M. Lamut, M. Godec, M. Torkar, M. Jenko, Surface and Interface Analysis, 39 (**2007**), 438–444

[6] M. Torkar, M. Godec, M. Lamut, Engineering Failure Analysis, 14 (**2007**), 1218–1223

[7] D. Mandrino, M. Godec, A. Kocijan, M. Lamut, M. Torkar, M. Jenko, Metalurgija, 47 (**2008**), 119–123

[8] D. Mandrino, M. Godec, M. Torkar, M. Jenko, Surface and Interface Analysis, 40 (**2008**), 285–289

[9] C. Donik, A. Kocijan, D. Mandrino, I. Paulin, M. Jenko, B. Pihlar, Applied Surface Science, 255 (**2009**), 7056–7061

[10] C. Donik, A. Kocijan, I. Paulin, M. Jenko, Mater. Tehnol., 43 (**2009**), 137–142

[11] C. Donik, A. Kocijan, J. T. Grant, M. Jenko, A. Drenik, B. Pihlar, Corrosion Science, 51 (**2009**), 827–832

[12] M. Godec, A. Kocijan, D. Dolinar, D. Mandrino, M. Jenko, V. Antolic, Biomedical Materials, 5 (**2010**), sp. iss., doi: 10.1088/ 1748-6041/ 5/4/045012

[13] A. Minovic, I. Milosev, V. Pisot, A. Cor, V. Antolic, Journal of Bone and Joint Surgery-British, 83B (**2001**), 1182–1190

[14] A. Kocijan, I. Milosev, B. Pihlar, Journal of Materials Science-Materials in Medicine. 14 (**2003**), 69–77

[15] A. Kocijan, C. Donik, M. Jenko, Mater. Tehnol., 43 (**2009**), 195–199

[16] A. Kocijan, C. Donik, M. Jenko, Mater. Tehnol., 43 (**2009**), 39–42

[17] C. Donik, D. Mandrino, M. Jenko, Vacuum, 84 (**2010**), 1266–1269

[18] A. Kocijan, Mater. Tehnol., 44 (**2010**), 239–242

[19] D. Mandrino, C. Donik, M. Jenko, Surface and Interface Analysis, 42 (**2010**), 762–765

[20] A. Kocijan, D. K. Merl, M. Jenko, Corrosion Science, 53 (**2011**), 776–783

[21] D. A. Skobir, M. Godec, M. Jenko, B. Markoli, Surface and Interface Analysis, 40 (**2008**), 513–517

[22] M. Godec, D. Mandrino, M. Jenko, Engineering Failure Analysis, 16 (**2009**), 1252–1261

[23] D. A. Skobir, M. Godec, M. Balcar, M. Jenko, Vacuum, 84 (**2009**), 205–208

[24] D. A. Skobir, M. Godec, A. Nagode, M. Jenko, Surface and Interface Analysis, 42 (**2010**), 717–721

[25] D. A. Skobir, M. Jenko, D. Mandrino, Surface and Interface Analysis, 36 (**2004**), 941–944

[26] M. Jenko, F. Vodopivec, H. J. Grabke, H. Viefhaus, B. Pracek, M. Lucas, M. Godec, Steel Research, 65 (**1994**), 500–504

[27] P. Sevc, D. Mandrino, J. Blach, M. Jenko, J. Janovec, Kovove Materialy-Metallic Materials, 40 (**2002**), 35–44

[28] J. A. Platt, A. Guzman, A. Zuccari, D. W. Thornburg, B. F. Rhodes, Y. Oshida, B. K. Moore, American Journal of Orthodontics and Dentofacial Orthopedics, 112 (**1997**), 69–79

[29] G. Blanco, A. Bautista, H. Takenouti, Cement & Concrete Composites, 28 (**2006**), 212–219

[30] L. Gil, S. Bruhl, L. Jimenez, O. Leon, R. Guevara, M. H. Staia, Surface & Coatings Technology, 201 (**2006**), 4424–4429

[31] T. Hryniewicz, R. Rokicki, K. Rokosz, Corrosion, 64 (**2008**), 660–665

[32] R. M. Souto, I. C. M. Rosca, S. Gonzalez, Corrosion, 57 (**2001**), 300–306

INFLUENCE OF THE FOAMING PRECURSOR'S COMPOSITION AND DENSITY ON THE FOAMING EFFICIENCY, MICROSTRUCTURE DEVELOPMENT AND MECHANICAL PROPERTIES OF ALUMINIUM FOAMS

VPLIV SESTAVE IN GOSTOTE PREKURZORJEV ZA PENJENJE NA UČINKOVITOST PENJENJA TER RAZVOJ MIKROSTRUKTURE IN MEHANSKIH LASTNOSTI ALUMINIJSKIH PEN

Varužan Kevorkijan[1], Srečo Davor Škapin[2], Irena Paulin[3,4], Borivoj Šuštaršič[3], Monika Jenko[3], Marjana Lažeta[5]

[1]Zasebni raziskovalec, Betnavska cesta 6, 2000 Maribor, Slovenija
[2]Institut "Jožef Stefan", Odsek za raziskave sodobnih materialov, Jamova 39, 1000 Ljubljana, Slovenija
[3]Inštitut za kovinske materiale in tehnologije, Lepi pot 11, 1000 Ljubljana, Slovenija
[4]TALUM, d. d., Tovarniška cesta 10, 2325 Kidričevo, Slovenija
[5]Impol, d. o. o., Partizanska 38, 2310 Slovenska Bistrica, Slovenija
varuzan.kevorkijan@impol.si

In this work, the influence of the composition, density and porosity of foaming precursors on the foaming efficiency, microstructure development and mechanical properties of aluminium foams are presented and discussed. The foams were prepared, starting from precursors made either by powder metallurgy (PM) or by the melt route. Following the PM route, precursors were made by mixing Al powder and 3–10 % of volume fractions of dolomite or calcium carbonate particles of particle size from 20 μm to 120 μm and cold isostatically pressing the mixture at 700 MPa. In the case of the melting route, precursors were made by introducing dolomite or calcium carbonate particles directly into the molten aluminium at 700 °C. After melt stirring, the precursors were prepared by casting the semi-solid slurry into a cylindrical, water-cooled mould.

Finally, aluminium foams were made in all cases by inserting precursors into a cylindrical stainless-steel mould and heating the arrangement at 750 °C for 10 min. After that, the mould was removed from the furnace and the foaming process was stopped by cooling in air to room temperature.

The microstructure of the obtained foams was investigated by optical and scanning electron microscopy (SEM-EDS), while XRD was applied for a detailed identification of phases.

The quality of the precursors was evaluated by determining their mechanical properties (uniaxial room-temperature compression stress-strain curve, compressive strength and energy absorption after a 30 % strain) and the foaming efficiency (the relative density of the foam obtained). The concentration of the foaming agent and the density of precursors were found to have a detrimental influence on the foaming efficiency as well as on the foam's microstructure and mechanical properties. The foaming of precursors with open porosity were inefficient.

Key words: aluminium foams, foaming agents, calcium carbonate, dolomite, characterization

V delu poročamo o vplivu sestave ter gostote oz. poroznosti prekurzorja za penjenje na učinkovitost penjenja ter razvoj mikrostrukture in mehanskih lastnosti aluminijevih pen. Pene smo izdelovali z uporabo prekurzorjev na osnovi Al s homogeno porazdeljenimi delci dolomita ali kalcijevega karbonata. Prekurzorje smo pripravljali po postopku prašne metalurgije (PM) in z litjem taline, kar je cenejše, zagotavlja pa manj homogeno porazdelitev sredstva za penjenje. S PM-postopkom smo prekurzorje za penjenje izdelovali iz zmesi Al prahu in 3–10 % dolomita ali kalcijevega karbonata različne povprečne velikosti (od 20 μm do 120 μm), ki smo jo izostatsko stisnili pri 700 MPa. Z litjem smo prekurzorje pripravljali tako, da smo delce penila uvajali v Al-talino, segreto do največ 700 °C, premešali in nastalo suspenzijo ulili v cilindričen, vodno hlajen jekleni model. Pene smo iz obeh vrst prekurzorjev izdelovali tako, da smo prekurzor vstavili v zaprt jekleni model za penjenje, segrevali pri 750 °C 10 min. ter nato ohlajali na zraku do sobne temperature.

Mikrostrukturo nastalih pen smo preučevali z optično in elektronsko (SEM/EDS) mikroskopijo, in sicer tako, da smo ugotavljali morfologijo in povprečno velikost por, sestavo vsebovanih faz pa z metodo rentgenske (XRD) difrakcije. Gostoto prekurzorjev in pen smo določali na osnovi mase in izračunane prostornine strojno obdelanih vzorcev, učinkovitost penjenja (relativno gostoto dobljene pene) pa na osnovi primerjave dejansko dosežene gostote pene in gostote aluminija. Primerjalno smo gostoto pen določali tudi z Arhimedovo metodo.

Kakovost izdelanih pen smo ocenjevali na osnovi njihovih mehanskih lastnosti (krivulje napetost – deformacija pri sobni temperaturi, tlačne trdnosti in sposobnosti absorpcije energije pri 30-odstotni deformaciji). Ugotovili smo, da na učinkovitost penjenja ter razvoj mikrostrukture in mehanskih lastnosti vplivata predvsem kemijska sestava in gostota prekurzorja za penjenje, pri čemer je bilo prekurzorje z odprto poroznostjo nemogoče peniti.

Ključne besede: aluminijske pene, sredstvo za penjenje, kalcijev karbonat, dolomit, karakterizacija

1 INTRODUCTION

Closed-cell-foamed aluminium is a macro-composite material consisting of an aluminium alloy matrix, usually discontinuously reinforced with various ceramic particulates and closed pores filled with gas distributed throughout the matrix. This unique structure possesses an unusual combination of properties, such as a low density, a high weight-specific stiffness, extraordinary energy absorption and a remarkable vibration attenuation, which are important for a number of engineering applications. Aluminium foams are also non-flammable, ecologically harmless and easily recyclable.

Methods to produce closed-cell aluminium foams have been known for a number of years and can be generally separated into two fundamental groups: (i) foaming liquid metal (casting procedures) and (ii) foaming metallic precursors (powder metallurgy-PM procedures)[1].

Titanium hydride (TiH_2) was mainly applied as a blowing agent for both the casting and powder metallurgical procedures of foaming for aluminium and aluminium alloys. The role of the blowing agent in both – the casting and powder metallurgical procedures of foaming of aluminium – is to release gas, since the metal is transferred in the liquid or the semi-liquid viscous state. However, as discussed in detail by Gergely et al.[2], several factors are involved in the selection of a blowing agent for the foaming of aluminium alloys. These include: (i) the kinetics and thermodynamic characteristics of decomposition reactions and reactions between the blowing agent particles and the molten or semi-molten aluminium alloy; (ii) the wetting of foaming-agent particles with molten metal; (iii) the influence of decomposition products and foaming gas on the stabilisation of foams; and (iv) the availability, cost and user-friendly handling of the powdered agent concerned.

As a foaming agent for the production of aluminium alloy foams by the casting and powder metallurgical routes, TiH_2 has several limitations that significantly influence the mass application of Al foams. The main limitations of the foaming technologies using TiH_2 as a foaming agent are the following:

- TiH_2 is very expensive.
- The decomposition temperature of TiH_2 is very low – starting at about 400 °C for the untreated hydride.
- TiH_2 particles act only as a blowing agent and are not involved in the foam stability.
- The density of TiH_2 (approx. 3.9 g/cm³) is significantly higher than the density of molten aluminium (approx. 2.7 g/cm³). Thus, during foaming the settling of TiH_2 particles occurs by gravity, resulting in a non-uniform microstructure of the foam.

The cost-effective and highly promising alternatives to the TiH_2 blowing agent are $CaCO_3$, as a marble powder or synthetic calcium carbonate, and dolomite powder. In contrast to TiH_2, calcium carbonate and dolomite are of low cost, significantly lower than the cost of aluminium, and with a density (2.71 g/cm³ to 2.84 g/cm³) almost identical to the density of molten aluminium. Moreover, the $CaCO_3$ and dolomite decomposition temperatures are above the melting point of aluminium, usually in the temperature interval between 660 °C and 930 °C. Therefore, $CaCO_3$ and dolomite are particularly suitable for the melt-route, settling-free production of foamed aluminium-based materials.

The "Foamcarp" process of the indirect foaming of aluminium using $CaCO_3$ particles previously introduced into a solidified precursor and, more recently, an additional indirect foaming procedure of molten aluminium with a $CaCO_3$-containing preform isostatically pressed from a mixture of $CaCO_3$ and AA6061 powders were reported[2,3].

In some early patents[4] and in the recent work of Nakamura et al.[5], the use of $CaCO_3$ was found to be potentially suitable as a foaming agent for direct (melt-route) foam manufacturing. Moreover, Bryat et al.[6] reported that $CaCO_3$ acts in contact with the molten aluminium as a foaming agent and, at the same time, through the decomposition products has a significant effect on the foam stabilisation, enabling the formation of "self-stabilized aluminium foams" (i.e., foams solidified from a foamable suspension created through the controlled decomposition of carbonate powders with molten aluminium). A similar cell face stabilising mechanism operating in carbonate-foamed melts was also reported by Gergely et al.[2].

The additional advantage of $CaCO_3$ in comparison with a TiH_2 blowing agent of the same average particle size is in achieving foams with higher porosity levels and finer cell sizes[5]. Gergely et al.[2] showed that by replacing TiH_2 by $CaCO_3$ as a foaming agent, foams can be produced having appreciably finer cells and more uniform cell structures at a significantly reduced raw-material cost.

On the other hand, Alcoa patented[7] a method of making an aluminum foam product by adding reactive gas producing particles to a molten aluminum alloy at a temperature that is above the decomposition temperature of the reactive-gas producing particles. The reactive-gas producing particles are selected from the group consisting of magnesium carbonate, calcium carbonate, dolomite and mixtures thereof.

Although the applicability of $CaCO_3$ and dolomite powders as a foaming agent in the direct and indirect foaming of aluminium alloys and composites has already been investigated, there is a need for an additional study of the influence of the $CaCO_3$ and dolomite powder morphology (particularly the average particle size and particle size distribution) and the role of $CaCO_3$ and dolomite decomposition products on the achievement of a better foam stability and a higher foam quality.

Hence, in this paper, the performance of synthetic calcium carbonate and natural dolomite powders as

cost-effective foaming agents was investigated by both the powder metallurgical and the melt route of foam preparation. The influence of $CaCO_3$ and dolomite particle morphology and volume fraction on the foaming behaviour and the development of the foam micro-structure were also monitored. As a result, a clearer interrelation between the foam morphology and struc-ture, on the one hand, and its mechanical properties, on the other, was established.

2 EXPERIMENTAL

All the foams made in this work were prepared by indirect foaming methods starting from a solid foamable precursor consisting of a metallic matrix containing uniformly dispersed blowing-agent particles. Foamable precursors were made either by: (i) the powder metallur-gical route, or (ii) the melt route using the same blowing agent, i.e., $CaCO_3$ powders (types C-A, C-B and C-C) with various average particle sizes ((38, 72 and 120) μm, respectively) and dolomite powders (type D-A, D-B and D-C) with various average particle sizes ((44, 76 and 97) μm, respectively).

Following the powder metallurgical (PM) route, foamable precursors with $CaCO_3$ particles were made by mixing Al powder with an average particle size of 63 μm (purity (mass fractions, w: 99.7 %, oxygen content: 0.25 %) and (3, 5, 7 and 12) % of the blowing agent, followed by cold compaction in a lubricated 20-mm diameter die to a pressure of 600 MPa to 900 MPa.

In the case of the melt route, foamable precursors with the same concentration of $CaCO_3$ blowing agent ((3, 5, 7 and 12) %) and the same geometry were prepared by an induction-heated, batch-type, stir-casting method by which the aluminium powder (the same as used for the PM route) was induction melted, followed by the addition of $CaCO_3$ particles, stirring and casting. Once the molten aluminium had reached 750 °C, the power was switched off and the melt stirring was initiated until the temperature of the melt decreased to 700 °C. After that, the blowing agent/aluminium powder mixture (1 : 2 mass ratio) was introduced and the melt was stirred (at approximately 1200 r/min) for an addi-tional 30–90 s. Finally, the foamable precursors were prepared by casting the semi-solid slurry into a room-temperature mould with a diameter of 20 mm.

In the case of the powder metallurgy (P/M) route, the fabrication of foamable precursors with dolomite parti-cles was conducted by mixing Al powder with an average particle size of 63 μm (purity: 99.7 %, oxygen content: 0.25 %), 5 % of SiC particles with an average particle size of 10 μm and (3, 5, 7 and 12) % of blowing agent, followed by cold compaction, in a lubricated 20-mm diameter die to a pressure of 600 MPa to 900 MPa.

Following the melt route, foamable precursors with the same concentration of dolomite blowing agent ((3, 5,

7 and 12) %) and the same geometry were prepared by induction-heated, batch-type, stir-casting in which aluminium powder (the same as used for the P/M route) was induction melted, followed by the addition of dolomite particles, stirring and casting. Once the molten aluminium was heated to 700 °C, the power was switched off and melt stirring was initiated until the temperature of the melt decreased to 685 °C. After that, the blowing agent/aluminium powder mixture (1 : 2 mass ratio) was introduced and the melt was stirred (at appro-ximately 1200 r/min) for an additional 30–90 s. Finally, the foamable precursors were prepared by casting the semi-solid slurry into a room-temperature mould with 20-mm diameter.

The solidified precursors were machined and some of the samples were additionally cold isostatically pressed. The density of the foamable precursors as well as of the foams obtained was calculated from the mass and geometry of the samples and, in addition, measured by Archimedes' method. The distribution of the blowing-agent particles inside the Al matrix was examined by an assessment of the optical and scanning electron micrographs of as-polished bars.

All the precursors were foamed in a conventional batch furnace with air atmosphere circulation under the same experimental conditions (temperature, time, cooling method). Before foaming, the individual precursors were inserted into a cylindrical (40-mm diameter, 70-mm long) stainless-steel mould coated with a boron nitride suspension. The mould dimensions and the precursor size (20-mm diameter and 60-mm long) were selected to allow the expansion of the precursor to a foam with a theoretical density close to 0.6 g/cm³. The arrangement was placed inside a pre-heated batch furnace at 750 °C for 10 min. After that period of time, the mould was removed from the furnace and the foaming process was stopped by rapid cooling with pressurised air to room temperature. The thermal history of the foam sample was recorded, using a thermocouple located directly in the precursor material.

The porosity of the foam was calculated using equation: 1 – (foam density/ aluminium density). Macro and microstructural examinations were performed on sections obtained by precision wire-cutting across the samples and on samples mounted in epoxy resin using optical and scanning electron microscopy (SEM-EDS).

The average size of the pores in the foams was estimated by an assessment of the optical and scanning electron micrographs of as-polished foam bars using the point-counting method and image-analysis and pro-cessing software.

Regarding the mechanical properties of the foams, uniaxial room-temperature compressive tests were carried out on a Zwick 1474 testing machine at a con-stant 5-mm/min crosshead displacement. Testing was performed on standard prismatic foam specimens of 50 mm × 12 mm × 17 mm and each point of the stress-strain

curve was determined as an average of four individual measurements. Compression was stopped whenever either 80 % strain or 95 kN force (equivalent to 61.9 MPa) was reached. As a result of testing, the uniaxial compression stress-strain curve, compressive strength and energy absorption after a 30 % strain were determined and correlated with the density, the average pore size and microstructure of the foam samples.

3 RESULTS AND DISCUSSION

3.1 Characterisation of the foamable precursors

The measured and calculated densities of the foamable precursors obtained by the PM route, **Table 1a,b**, confirmed that under isostatic pressing with an applied pressure of 700 MPa the precursors prepared by PM possessed a closed porosity and densities above 98 % of theoretical, whereas as-machined precursors obtained by the melt route (**Table 2a,b**) had a significant fraction of open porosity and thus were not suitable for foaming to the desired foam densities (usually about 0.5 g/cm^3 to 0.7 g/cm^3). However, after additional isostatic pressing, the porosity in these precursors was successfully reduced to below 2.0 % (volume fraction φ/%) (**Table 3 a,b**) and foam samples with densities between 0.62 g/cm^3 and 0.80 g/cm^3 were obtained.

It is important to note that very high precursor densities (>99 % of theoretical) were achieved only in the precursors prepared by the powder metallurgical route with 3–7 % of CaCO$_3$ and dolomite particles of Type-C-A or Type D-A (**Table 1 a,b**). With a higher particle content, and by using coarser CaCO$_3$ or dolomite powders of Type-C-B or Type-C-C as well as Type D-B and Type D-C, this could not be achieved and resulted in a lower foaming efficiency, as evident in **Tables 4 a,b–6 a,b**.

The foaming efficiency of the precursors was evaluated from the relative density of the foam obtained, ρ, calculated by dividing the apparent density of the foam, ρ_F, by the density of aluminium, ρ_{Al}. Thus, the foaming efficiency is expressed as:

$$\eta = 1 - \rho = 1 - (\rho_F/\rho_A) \qquad (1)$$

which actually corresponds to the volume fraction of pores in the foam samples. The lower the foam density, the higher is the foaming efficiency.

In all cases the experimental results clearly indicate that the porosity measured in foamable precursors and the apparent density achieved in aluminium foam samples are inversely proportional. Generally, foamable precursors with a lower porosity resulted in foam samples with a higher apparent density and a lower foaming efficiency.

Under the same foaming conditions (temperature, time), the average pore size of the foam samples was influenced by the density of foaming precursors and the initial size of the foaming particles. As a rule, in foams made from precursors with high density ($\geq$99 % of theoretical), the average pore size remained below 1.0 mm. On the other hand, in foams made from precursors with a lower density (below 99 % of theoretical), the pores grew to a 20 % to 50 % higher average size pore.

Regarding the initial size of the foaming particles, which also influences the density of the precursor and, hence, the density of the foam samples, the increase of the average particle size of CaCO$_3$ or dolomite foaming agent was observed to have a detrimental influence on the average size of the pores. Coarser CaCO$_3$ and dolomite powders led to the formation of larger bubbles in the foam structure.

Table 1 a: Porosity of CaCO$_3$ particles containing foamable precursors obtained by the PM route
Tabela 1 a: Poroznost prekurzorjev s CaCO$_3$-penilom, izdelanih s postopkom prašne metalurgije

Chemical composition of precursors (w/%)		Porosity (φ/%)	
CaCO$_3$	Al powder	Calculated	Measured
Type C-A			
3	97	0.8 ± 0.08	0.7 ± 0.04
5	95	0.8 ± 0.08	0.8 ± 0.04
7	93	0.9 ± 0.09	1.0 ± 0.05
10	90	1.1 ± 0.11	1.2 ± 0.06
Type C-B			
3	97	1.1 ± 0.10	1.0 ± 0.05
5	95	1.1 ± 0.11	1.1 ± 0.06
7	93	1.3 ± 0.13	1.3 ± 0.07
10	90	1.7 ± 0.17	1.8 ± 0.09
Type C-C			
3	97	1.3 ± 0.11	1.4 ± 0.07
5	95	1.5 ± 0.15	1.4 ± 0.07
7	93	1.6 ± 0.16	1.7 ± 0.09
10	90	1.8 ± 0.18	2.0 ± 0.10

Table 1 b: Porosity of dolomite particles containing foamable precursors obtained by the PM route.
Tabela 1 b: Poroznost prekurzorjev z dolomitom kot penilom, izdelanih po postopku prašne metalurgije

Chemical composition of performs w/%			Porosity ρ/%	
Dolomite	SiC	Al powder	Calculated	Measured
Type D-A				
3	5	92	0.7 ± 0.07	0.7 ± 0.04
5	5	90	0.8 ± 0.08	0.8 ± 0.04
7	5	88	0.9 ± 0.09	1.0 ± 0.05
10	5	85	1.2 ± 0.12	1.3 ± 0.07
Type D-B				
3	5	92	1.0 ± 0.10	1.0 ± 0.05
5	5	90	1.0 ± 0.10	1.1 ± 0.06
7	5	88	1.2 ± 0.12	1.3 ± 0.07
10	5	85	1.6 ± 0.16	1.8 ± 0.09
Type D-C				
3	5	92	1.1 ± 0.11	1.1 ± 0.06
5	5	90	1.2 ± 0.12	1.3 ± 0.06
7	5	88	1.3 ± 0.13	1.4 ± 0.07
10	5	85	1.8 ± 0.18	2.0 ± 0.10

Table 2a: Porosity of as-machined $CaCO_3$ containing foamable precursors prepared by the melt route

Tabela 2a: Poroznost strojno obdelanih prekurzorjev s $CaCO_3$ penilom, izdelanih po livarskem postopku

Chemical composition of precursors (w/%)		Porosity (φ/%)	
$CaCO_3$	Al powder	Calculated	Measured
Type C-A			
3	97	4.2 ± 0.42	4.1 ± 0.21
5	95	4.6 ± 0.46	4.4 ± 0.22
7	93	4.9 ± 0.49	4.8 ± 0.24
10	90	5.3 ± 0.53	5.2 ± 0.26
Type C-B			
3	97	4.1 ± 0.41	4.2 ±0.21
5	95	4.7 ± 0.47	4.7 ± 0.24
7	93	5.0 ± 0.50	5.1 ± 0.26
10	90	5.4 ± 0.54	5.5 ± 0.28
Type C-C			
3	97	3.9 ± 0.39	4.1 ± 0.21
5	95	4.2 ± 0.42	4.2 ± 0.21
7	93	4.3 ± 0.43	4.4 ± 0.22
10	90	4.8 ± 0.48	4.9 ± 0.25

Table 2b: Porosity of as-machined dolomite particles containing foamable performs prepared by the melt route.

Tabela 2b: Poroznost strojno obdelanih prekurzorjev z dolomitom kot penilom, izdelanih po livarskem postopku.

Chemical composition of performs w/%			Porosity ρ/%	
Dolomite	SiC	Al powder	Calculated	Measured
Type D-A				
3	5	92	4.7 ± 0.47	4.9 ± 0.25
5	5	90	4.9 ± 0.49	5.1 ± 0.26
7	5	88	5.4 ± 0.54	5.8 ± 0.29
10	5	85	6.1 ± 0.61	6.6 ± 0.33
Type D-B				
3	5	92	4.5 ± 0.45	4.7 ± 0.24
5	5	90	4.7 ± 0.47	5.0 ± 0.25
7	5	88	5.0 ± 0.50	5.3 ± 0.27
10	5	85	5.7 ± 0.57	6.2 ± 0.31
Type D-C				
3	5	92	4.4 ± 0.44	4.5 ± 0.23
5	5	90	4.5 ± 0.45	4.7 ± 0.24
7	5	88	4.7 ± 0.47	5.0 ± 0.25
10	5	85	4.9 ± 0.49	5.3 ± 0.27

Table 3a: Porosity of $CaCO_3$ containing foamable precursors obtained by the melt route improved by additional isostatic pressing

Tabela 3a: Poroznost prekurzorjev s $CaCO_3$-penilom, izdelanih po livarskem postopku, izboljšana z dodatnim hladnim izostatskim stiskanjem

Chemical composition of precursors (w/%)		Porosity (φ/%)	
$CaCO_3$	Al powder	Calculated	Measured
Type C-A			
3	97	1.3 ± 0.13	1.3 ± 0.06
5	95	1.6 ± 0.16	1.7 ± 0.09
7	93	1.9 ± 0.19	2.0 ± 0.10
10	90	2.0 ± 0.20	2.2 ± 0.11
Type C-B			
3	97	1.1 ± 0.11	1.2 ± 0.06
5	95	1.2 ± 0.12	1.2 ± 0.06
7	93	1.4 ± 0.14	1.5 ± 0.08
10	90	1.7 ± 0.17	1.9 ± 0.09
Type C-C			
3	97	1.0 ± 0.10	1.0 ± 0.10
5	95	1.2 ± 0.12	1.1 ± 0.06
7	93	1.3 ± 0.13	1.4 ± 0.07
10	90	1.6 ± 0.16	1.8 ± 0.09

Table 3b: Porosity of dolomite particles containing foamable performs obtained by the melt route improved by additional isostatic pressing

Tabela 3b: Poroznost prekurzorjev z dolomitom kot penilom, izdelanih po livarskem postopku, izboljšana z dodatnim hladnim izostatskim stiskanjem

Chemical composition of performs w/%			Porosity ρ/%	
Dolomite	SiC	Al powder	Calculated	Measured
Type D-A				
3	5	92	0.9 ± 0.09	0.9 ± 0.05
5	5	90	0.9 ± 0.09	0.9 ± 0.05
7	5	88	1.0 ± 0.10	1.1 ± 0.06
10	5	85	1.1 ± 0.11	1.2 ± 0.06
Type D-B				
3	5	92	0.9 ± 0.09	0.9 ± 0.05
5	5	90	0.9 ± 0.09	0.9 ± 0.05
7	5	88	0.9 ± 0.09	1.0 ± 0.05
10	5	85	1.0 ± 0.10	1.1 ± 0.06
Type D-C				
3	5	92	0.8 ± 0.08	0.8 ± 0.04
5	5	90	0.8 ± 0.08	0.8 ± 0.04
7	5	88	0.8 ± 0.08	0.9 ± 0.05
10	5	85	0.9 ± 0.09	1.0 ± 0.05

Table 4a: Density, foaming efficiency and average pore size of aluminium foams prepared by the PM route using $CaCO_3$ foaming agent

Tabela 4a: Gostota, učinkovitost penjenja in povprečna velikost por v aluminijskih penah, izdelanih po postopku prašne metalurgije z uporabo $CaCO_3$ kot sredstva za penjenje

Initial composition of foamable precursors (w/%)		Selected properties of foamed samples		
$CaCO_3$	Al powder	Density (g/cm³)	Foaming efficiency (%)	Average pore size (mm)
Type D-A				
3	97	0.42 ± 0.02	84.4	0.8 ± 0.08
5	95	0.47 ± 0.03	82.6	0.9 ± 0.09
7	93	0.51 ± 0.03	81.1	1.0 ± 0.10
10	90	0.55 ± 0.03	79.6	1.2 ± 0.12
Type D-B				
3	97	0.46 ± 0.03	83.0	0.5 ± 0.05
5	95	0.49 ± 0.03	81.9	0.7 ± 0.07
7	93	0.53 ± 0.03	80.4	0.8 ± 0.08
10	90	0.59 ± 0.03	78.1	0.9 ± 0.09
Type D-C				
3	97	0.53 ± 0.03	80.4	0.5 ± 0.05
5	95	0.55 ± 0.03	79.6	0.5 ± 0.05
7	93	0.59 ± 0.03	78.1	0.6 ± 0.06
10	90	0.61 ± 0.03	77.4	0.8 ± 0.08

Table 4b: Density, foaming efficiency and the average pore size of aluminium foams prepared by the PM route using dolomite as foaming agent

Tabela 4b: Gostota, učinkovitost penjenja in povprečna velikost por v aluminijskih penah, izdelanih po postopku prašne metalurgije z uporabo dolomita kot sredstva za penjenje

Initial composition of foamable performs w/%			Selected properties of foamed samples		
Dolo-mite	SiC	Al powder	Density (g/cm³)	Foaming efficiency (%)	Average pore size (mm)
Type D-A					
3	5	92	0.56 ± 0.03	79,3	0.9 ± 0.09
5	5	90	0.59 ± 0.03	78,1	0.9 ± 0.09
7	5	88	0.63 ± 0.03	76,7	1.1 ± 0.11
10	5	85	0.69 ± 0.03	74,4	1.3 ± 0.13
Type D-B					
3	5	92	0.51 ± 0.03	81,1	0.6 ± 0.06
5	5	90	0.53 ± 0.03	80,4	0.7 ± 0.07
7	5	88	0.57 ± 0.03	78,9	0.9 ± 0.09
10	5	85	0.59 ± 0.03	78,1	0.9 ± 0.09
Type D-C					
3	5	92	0.50 ± 0.03	81,5	0.6 ± 0.06
5	5	90	0.52 ± 0.03	80,7	0.6 ± 0.06
7	5	88	0.55 ± 0.03	79,6	0.8 ± 0.08
10	5	85	0.56 ± 0.03	79,3	0.9 ± 0.09

Table 5a: Density, foaming efficiency and average pore size of aluminium foams prepared from as-machined foamable preforms fabricated by the melt route using $CaCO_3$ foaming agent

Tabela 5a: Gostota, učinkovitost penjenja in povprečna velikost por v aluminijskih penah, izdelanih iz strojno obdelanih prekurzorjev s $CaCO_3$ kot sredstvom za penjenje, dobljenih po livarskem postopku

Initial composition of foamable precursors (w/%)		Selected properties of foamed samples		
$CaCO_3$	Al powder	Density (g/cm³)	Foaming efficiency (%)	Average pore size (mm)
Type C-A				
3	97	0.89 ± 0.05	67.0	1.1 ± 0.11
5	95	0.92 ± 0.05	65.0	1.3 ± 0.13
7	93	0.97 ± 0.05	64.1	1.4 ± 0.14
10	90	0.99 ± 0.05	63.3	1.4 ± 0.14
Type C-B				
3	97	0.84 ± 0.03	68.9	0.8 ± 0.08
5	95	0.89 ± 0.03	67.0	0.9 ± 0.09
7	93	0.93 ± 0.04	65.6	0.9 ± 0.09
10	90	0.95 ± 0.04	64.8	1.1 ± 0.11
Type C-C				
3	97	0.79 ± 0.04	70.7	0.7 ± 0.07
5	95	0.81 ± 0.04	70.0	0.8 ± 0.08
7	93	0.85 ± 0.04	68.5	1.2 ± 0.12
10	90	0.88 ± 0.04	67.4	1.5 ± 0.15

Table 5b: Density, foaming efficiency and average pore size of aluminium foams prepared from as-machined foamable performs fabricated by the melt route using dolomite as foaming agent

Tabela 5b: Gostota, učinkovitost penjenja in povprečna velikost por v aluminijskih penah, izdelanih iz strojno obdelanih prekurzorjev z dolomitom kot sredstvom za penjenje, dobljenih po livarskem postopku

Initial composition of foamable performs w/%			Selected properties of foamed samples		
Dolo-mite	SiC	Al powder	Density (g/cm³)	Foaming efficiency (%)	Average pore size (mm)
Type D-A					
3	5	92	0.71 ± 0.04	73,7	1.2 ± 0.12
5	5	90	0.72 ± 0.04	73,3	1.4 ± 0.14
7	5	88	0.75 ± 0.04	72,2	1.4 ± 0.14
10	5	85	0.81 ± 0.04	70,0	1.5 ± 0.15
Type D-B					
3	5	92	0.61 ± 0.03	77,4	0.8 ± 0.08
5	5	90	0.63 ± 0.03	76,6	0.9 ± 0.09
7	5	88	0.66 ± 0.03	75,5	1.0 ± 0.10
10	5	85	0.70 ± 0.04	74,1	1.1 ± 0.11
Type D-C					
3	5	92	0.65 ± 0.03	75,9	0.8 ± 0.08
5	5	90	0.66 ± 0.03	75,5	0.9 ± 0.09
7	5	88	0.68 ± 0.03	74,8	1.1 ± 0.11
10	5	85	0.72 ± 0.04	73,3	1.5 ± 0.15

Table 6a: Density, foaming efficiency and average pore size of aluminium foams prepared by the melt route from as-machined and additionally isostatically pressed foamable precursors with $CaCO_3$ foaming agent

Tabela 6a: Gostota, učinkovitost penjenja in povprečna velikost por v aluminijskih penah, izdelanih iz strojno obdelanih in hladno izostatsko stisnjenih prekurzorjev s $CaCO_3$ kot sredstvom za penjenje, dobljenih po livarskem postopku

Initial composition of foamable precursors (w/%)		Selected properties of foamed samples		
$CaCO_3$	Al powder	Density (g/cm³)	Foaming efficiency (%)	Average pore size (mm)
Type C-A				
3	97	0.69 ± 0.03	74.4	1.1 ± 0.11
5	95	0.72 ± 0.04	73.3	1.2 ± 0.12
7	93	0.76 ± 0.04	71.9	1.3 ± 0.13
10	90	0.80 ± 0.04	70.4	1.6 ± 0.16
Type C-B				
3	97	0.64 ± 0.03	76.3	0.8 ± 0.08
5	95	0.69 ± 0.03	74.4	0.9 ± 0.09
7	93	0.72 ± 0.04	73.3	1.3 ± 0.13
10	90	0.74 ± 0.04	72.6	1.4 ± 0.14
Type C-C				
3	97	0.62 ± 0.03	77.0	0.9 ±0.09
5	95	0.67 ± 0.03	75.2	1.1 ± 0.11
7	93	0.71 ± 0.04	73.7	1.3 ± 0.13
10	90	0.73 ± 0.04	73.0	1.6 ± 0.16

Table 6b: Density, foaming efficiency and average pore size of aluminium foams prepared by the melt route from as-machined and additionally isostatically pressed foamable performs using dolomite as foaming agent

Tabela 6b: Gostota, učinkovitost penjenja in povprečna velikost por v aluminijskih penah, izdelanih iz strojno obdelanih in hladno izostatsko stisnjenih prekurzorjev z dolomitom kot sredstvom za penjenje, dobljenih po livarskem postopku

Initial composition of foamable performs w/%			Selected properties of foamed samples		
Dolo-mite	SiC	Al powder	Density (g/cm³)	Foaming efficiency (%)	Average pore size (mm)
Type D-A					
3	5	92	0.63 ± 0.03	76,7	1.1 ± 0.11
5	5	90	0.67 ± 0.03	75,2	1.2 ± 0.12
7	5	88	0.71 ± 0.03	73,7	1.3 ± 0.13
10	5	85	0.78 ± 0.03	71,1	1.6 ± 0.16
Type D-B					
3	5	92	0.57 ± 0.03	78,9	0.7 ± 0.07
5	5	90	0.59 ± 0.03	78,1	0.9 ± 0.09
7	5	88	0.62 ± 0.03	77,0	1.1 ± 0.11
10	5	85	0.63 ± 0.03	76,7	1.4 ± 0.14
Type D-C					
3	5	92	0.58 ± 0.03	78,5	0.7 ± 0.07
5	5	90	0.60 ± 0.03	77,8	0.8 ± 0.08
7	5	88	0.64 ± 0.03	76,3	1.0 ± 0.10
10	5	85	0.67 ± 0.03	75,2	1.1 ± 0.11

3.2 Microstructural investigation of aluminium foam samples

A similar cellular structural development with spherical, closed pores was obtained by both the powder metallurgy (**Figure 1**) and the melt processing route (**Figure 2**). However, as is evident in **Figure 1**, the samples obtained by the powder metallurgical route had a more uniform microstructure consisting of well-separated individual cells. On the other hand, the microstructure of the samples obtained by the melt processing route, **Figure 2**, revealed the presence of some individual, non-uniformities created by flow (the movement of bubbles with respect to each other), drainage (flow of liquid metal through the intersection of three foam
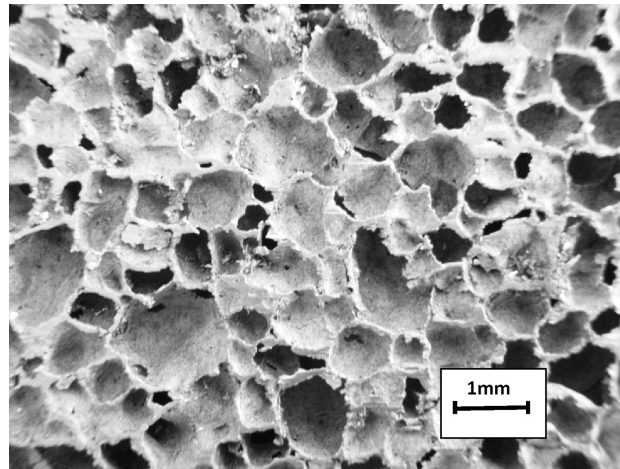

Figure 1: Cross-section of an aluminium foam obtained by the powder metallurgical route with well-separated individual cells and relatively uniform microstructure.
Slika 1: Posnetek prečnega prereza vzorca aluminijske pene, izdelanega po postopku prašne metalurgije, z izraženimi posameznimi porami in relativno enakomerno mikrostrukturo
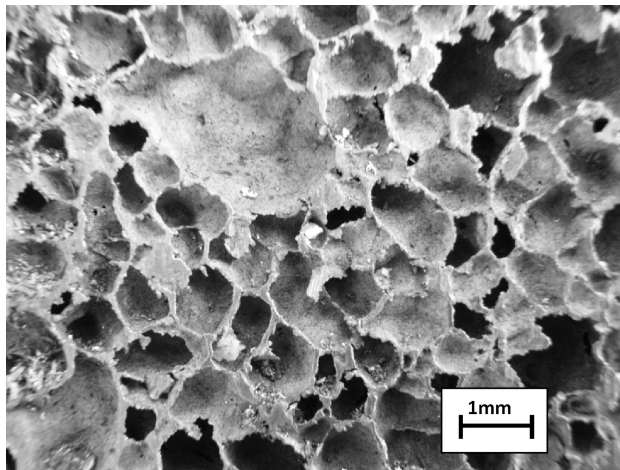

Figure 2: Cross-section of an aluminium foam obtained by the melt route with a characteristic channel network and foam drainage
Slika 2: Posnetek prečnega prereza vzorca aluminijske pene, izdelanega po livarskem postopku, na katerem so poleg posameznih por opazne tudi nehomogenosti, povzročene z zlitjem por in odtekanjem taline skozi značilne kanale v mikrostrukturi

films), coalescence (sudden instability in foam film) and coarsening (slow diffusion of gas from smaller bubbles to larger ones).

The absence of considerable pore coarsening and drainage suggests that there is a cell-face stabilising mechanism operating in the carbonate-foamed melts[2], slowing down the cell-face rupturing process and hence, inhibiting cell coarsening. The mechanism is likely to be a result of the foaming gas (CO_2)/melt or semi-solid slurry reaction during the foaming procedure, as was discussed in detail by Gergely et al.[2].

Concerning the average pore size and the uniformity in cell size distribution, foams made by the powder metallurgical route have finer pores and a more regular morphology than samples made by the melt route, particularly those from as-machined precursors. However, an additional cold isostatic pressing of the as-machined precursor obtained by the melt route was found to help in achieving more uniform foams with a smaller average pore size, similar to those obtained by the powder metallurgical route. The improvement is most probably caused by better compacting of the individual $CaCO_3$ or dolomite particles and the aluminium matrix, resulting in a higher density of the foamable precursor.

3.3 Mechanical properties

Figure 3 shows an example of the stress-strain response of samples foamed from preforms prepared by the PM route in which the compressive strength of the foams was correlated with their density.

Because of the closed cell structure, the compressive foam behaviour in all cases showed a typical stress-strain diagram with a division into three parts: a linear increase in stress mainly caused by elastic deformation, followed by a plateau caused by homogeneous plastic deformation and a final steep increase due to the collapse of the cells. The compressive strength was taken as the initial peak
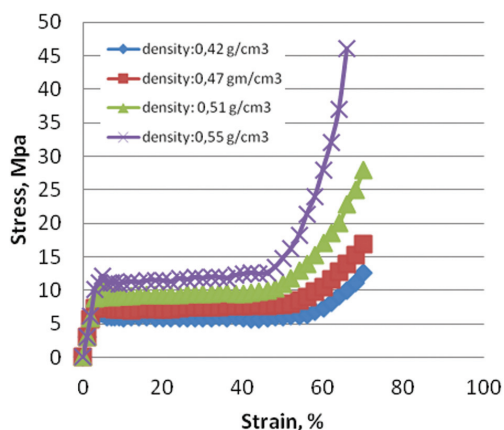

Figure 3: The stress-strain response of various aluminium foam samples from preforms obtained by the PM route using the $CaCO_3$ foaming agent.
Slika 3: Krivulja napetost – deformacija za vzorce aluminijskih pen na osnovi predoblik s $CaCO_3$ penilom, izdelanih po postopku prašne metalurgije
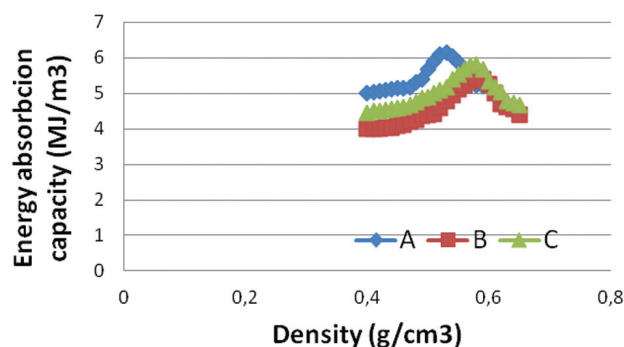

Figure 4: Example of optimization of the aluminium foam density range for the maximum energy absorption capacity: A)-foams obtained by powder metallurgy, B)-foams obtained from as-machined precursors fabricated by the melt route, and C)-foams obtained from as-machined and cold isostatically pressed precursors fabricated by the melt route. The foaming agent was $CaCO_3$.
Slika 4: Primer optimiziranja gostote vzorcev aluminijskih pen za doseganje največje sposobnosti absorpcije energije: A) pene, izdelane po postopku prašne metalurgije; B) pene iz strojno obdelanih prekuzorjev, narejenih po livarskem postopku; C) pene iz strojno obdelanih in hladno izostatsko stisnjenih prekurzorjev, narejenih po livarskem postopku. Kot sredstvo za penjenje je bil uporabljen $CaCO_3$.

stress. Foams made by the PM route possessed the highest compressive strength, while samples foamed from as-machined precursors had significantly lower values. For the interval of foam densities analysed in this work (from $0.42 g/cm^3$ to $0.55 g/cm^3$), it was found that in more dense foam samples the position of the plateau shifted toward higher stress values.

The energy absorbed per unit volume (E-energy absorption capacity), which is one of the most important characteristics of aluminium foams, was determined from the area under the stress-strain plots as follows[8]:

$$E = \int_0^l \sigma(\varepsilon)\,\mathrm{d}\varepsilon \qquad (2)$$

Where σ is the compressive stress, l is the limit of the strain concerned and ε is the compressive strain. The calculated values of energy-absorption capacity for samples are plotted in **Figure 2** and correlated with the foam density. The typical response was found to be a quasi-Gaussian function with a maximum energy-absorption capacity in a very narrow density range.

The maximum energy-absorption capacity for various foams is summarized in **Figure 3**. For foams made by the PM route, the maximum energy-absorption capacity of $6.14 MJ/m^3$ was achieved in foams with a density of $0.53 g/cm^3$. On the other hand, in samples foamed from as-machined precursors fabricated by melt route, a maximum energy-absorption capacity of only $5.41 MJ/m^3$ was found. The maximum appeared at a foam density of $0.58 g/cm^3$. Finally, in the melt route fabricated precursors, additionally isostatically pressed before foaming, an intermediate maximum energy-absorption capacity of $5.82 MJ/m^3$ was found in samples with a density of $0.58 g/cm^3$.

The foaming process does not materially affect the properties of the cell-wall material. However, it leads to a unique spatial distribution of the aluminium which results in significantly different properties of the foamed component in comparison with the bulk part. It is obvious that the properties of the aluminium foam significantly depend on its porosity, so that a desired property (or combination of properties) can be tailored by selecting the foam density.

The mechanical properties of the foams obtained by applying dolomite powder as a foaming agent are fully comparable with the corresponding properties of foams fabricated using TiH_2.

4 CONCLUSION

The following conclusions can be drawn from this work.

- TiH_2 powder as foaming agent was successfully replaced by commercial $CaCO_3$ or dolomite powders of a different average particle size.
- Foaming precursors with different proportions (φ = 3–10 %) of $CaCO_3$ or dolomite powder particles as a foaming agent were routinely prepared either by the powder metallurgical or melt route.
- Precursors obtained by powder metallurgy had superior homogeneity and densities ≥98% of theoretical. Moreover, in precursors obtained by the PM route containing φ = 3–7 % of $CaCO_3$ or dolomite particles of an average particle size of below 50 µm, densities ≥99 % of theoretical were achieved.
- With greater addition of $CaCO_3$ or dolomite particles and by using $CaCO_3$ or dolomite powders with a higher average particle size (above 70 µm), densities ≥99 % of theoretical could not be achieved.
- The foaming efficiency of experimentally prepared precursors was evaluated based on the relative density of foams obtained (the apparent density of the foam divided by the density of aluminium). The experimental findings showed that the apparent density of the foam samples is inversely proportional to the density of the foaming precursor. Thus, foamable precursors with a higher density resulted in foam samples with a lower apparent density and a higher foaming efficiency. On the other hand, the foaming efficiency and the average pore size of the foamed samples are generally reciprocally dependent.

Thus, a higher foaming efficiency results in a foam microstructure with finer pores.

- The mechanical properties (compression strength and energy absorption capacity) of the foamed samples are also strongly influenced by the foaming efficiency. For the range of foam densities analysed, the compression strength, considered as the initial peak stress, was found to be superior (approx. 13 MPa) in samples with increased density (0.55 g/cm^3) and hence, lower foaming efficiency (79.6 %). In contrast to this, the maximum energy-absorption capacity was achieved in foams with the highest foaming efficiency.
- From the experimental findings is obvious that the properties of an aluminium foam significantly depend on its porosity and the desired property (or combination of properties) can be tailored by the foam density.
- The experimental findings confirm that the microstructure, compression strength and energy-absorption capacity of aluminium foams prepared with $CaCO_3$ or dolomite powder as foaming agent are quite comparable with their counterparts foamed by TiH_2.

Acknowledgement

5 REFERENCES

[1] J. Banhart, Adv. Eng. Mater., 8 (**2006**) 9, 781
[2] V. Gergely, D. C. Curra, T. W. Clyne, Composites Science and Technology, 63 (**2003**) 2301
[3] L. E. G. Cambronero, J. M. Ruiz-Roman, F. A. Corpas, J. M. Ruiz Prieto, Journal of Materials Processing Technology, 209 (**2009**) 1803
[4] US Patent No. 2.751.289, June 19, 1956
[5] T. Nakamura, S. V. Gbyloskurenco, K. Savanto, A. V. Byakova, R. Ishikawa, Mater. Trans., 43 (**2002**) 5, 1191–1196
[6] J. D. Bryant, M. D. Clowley, M. D. Wilhelmy, J. A. Kallivayalil, W. Wang, In Metfoam 2007, DEStech Publications, Inc., Lancaster, PA, 2008, pp. 27
[7] US Patent No. 7.452.402, November 18, 2008
[8] S. Asavavisithchai, R. Tantisiriphaiboon, Chiang Mai J. Sci., 36 (**2009**) 3, 302

MULTI-OBJECTIVE OPTIMIZATION OF THE CUTTING FORCES IN TURNING OPERATIONS USING THE GREY-BASED TAGUCHI METHOD

MULTI NAMENSKA OPTIMIZACIJA STRUŽENJA Z UPORABO TAGUCHI METODE NA GREY PODLAGI

Yigit Kazancoglu[1], Ugur Esme[2], Melih Bayramoğlu[3], Onur Guven[4], Sueda Ozgun[5]

[1]Izmir University of Economics, Department of Business Administration, 35330, Balcova-Izmir/Turkey
[2]Mersin University, Tarsus Technical Education Faculty, Department of Mechanical Education, 33480, Tarsus-Mersin/Turkey
[3]Cukurova University, Engineering and Architecture Faculty, Department of Mechanical Engineering, 01030, Balcali-Adana/Turkey
[4]Mersin University, Engineering Faculty, Department of Mechanical Engineering, 33400, Mersin/Turkey
[5]Mersin University Vocational School of Gülnar, 33400, Gülnar-Mersin/Turkey
uguresme@gmail.com

This study investigated the multi-response optimization of the turning process for an optimal parametric combination to yield the minimum cutting forces and surface roughness with the maximum material-removal rate (MRR) using a combination of a Grey relational analysis (GRA) and the Taguchi method. Nine experimental runs based on an orthogonal array of the Taguchi method were performed to derive objective functions to be optimized within the experimental domain. The objective functions were selected in relation to the parameters of the cutting process: cutting force, surface roughness and MRR. The Taguchi approach was followed by the Grey relational analysis to solve the multi-response optimization problem. The significance of the factors on the overall quality characteristics of the cutting process was also evaluated quantitatively using the analysis-of-variance method (ANOVA). Optimal results were verified through additional experiments. This shows that a proper selection of the cutting parameters produces a high material-removal rate with a better surface roughness and a lower cutting force.

Keywords: turning, cutting, Grey relation analysis, Taguchi method, optimization

Raziskani so odgovori optimizacije procesa struženja z optimalno kombinacijo parametrov s ciljem doseči minimalne sile rezanja in hrapavost površine pri maksimalni odstranitvi materiala (MRR) z uporabo kombinacije Grey odvisnostne analize (GRA) in Taguchi metode. Devet preizkusov na podlagi ortogonale ureditve po Taguchi metodi je bilo izvršeno za razvoj objektivnih funkcij in njihovo optimizacijo v področju preizkusov. Objektivne funkcije so bile izbrane glede na proces rezanja: sila rezanja, hrapavost površine in MRR. Taguchi približek z Grey analizo odvisnosti je bil uporabljen za rešitev problema optimizacije z več odgovori. Pomen dejavnikov na kakovostne značilnosti procesa rezanja je bil kvantitativno ocenjen z uporabo metode analize variance (ANOVA). Optimalni rezultati so bili verificirani z dopolnilnimi preizkusi. Rezultati kažejo, da prava izbira parametrov rezanja zagotovi visoko hitrost odstranjevanja materiala pri boljši kakovosti površine in manjši sili rezanja.

Ključne besede: struženje, rezkanje, Grey analiza, Taguchi metoda, optimizacija

1 INTRODUCTION

Turning is a very important machining process in which a single-point cutting tool removes material from the surface of a rotating cylindrical workpiece. The cutting tool is fed linearly in a direction parallel to the axis of rotation [1].

As indicated in **Figure 1**, the turning is carried out on a lathe that provides the power to turn the workpiece at a given rotational speed and to feed the cutting tool at a specified rate and depth of cut. Therefore, three cutting parameters, i.e., cutting speed (V), feed rate (F), and depth of cut (d), should be properly selected for a better surface finish with a lower cutting force.

In a turning operation, it is an important task to select the cutting parameters to achieve a high cutting performance. Usually, the desired cutting parameters are determined based on experience or by using a handbook [1]. However, this does not ensure that the selected cutting parameters have optimal or near optimal cutting perfor-

mance for a particular machine and environment. To select the cutting parameters properly, several mathematical models [1–6] based on statistical regression techniques or neural computing have been constructed to establish
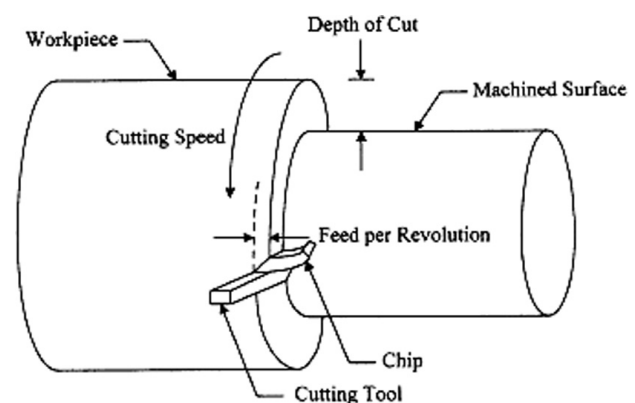

Figure 1: Schematic representation of the turning process [1]
Slika 1: Shema procesa struženja [1]

the relationship between the cutting performance and the cutting parameters. Then, an objective function with constraints is formulated to solve the optimal cutting parameters using optimization techniques. Therefore, considerable knowledge and experience are required to use this modern approach [1]. Furthermore, a large number of cutting experiments has to be performed and analyzed in order to build the mathematical models. Thus, the required model building is very costly in terms of time and materials [1].

Basically, the Taguchi method is a powerful tool for the design of high-quality systems. It provides a simple, efficient and systematic approach to optimize the designs for performance, quality, and cost [1–6]. The methodology is valuable when the design parameters are qualitative and discrete. Taguchi parameter design can optimize the performance characteristics through the settings of the design parameters and reduce the sensitivity of the system performance to sources of variation. In recent years, the rapid growth of interest in the Taguchi method has led to numerous applications of the method in a world-wide range of industries and countries [1,7,8].

Therefore, this study applied a Taguchi L_9 orthogonal array to plan the experiments on the turning process. The three controlling factors, including the cutting speed (V), the depth of cut (d) and feed rate (f), were selected. The Grey relational analysis is then applied to examine how the cutting factors influence the cutting force (F), the surface roughness (Ra) and the material removal rate (MRR). An optimal parameter combination was then obtained. Through analyzing the Grey relational grade matrix, the most influential factors for individual quality targets of the turning process can be identified. Additionally, an analysis of variance (ANOVA) was also utilized to examine the most significant factors for the F, Ra and MRR in the turning process.

2 GREY RELATIONAL ANALYSIS (GRA)

2.1 Data Preprocessing

In a Grey relational analysis, experimental data, i.e., measured features of the quality characteristics, are first normalized, ranging from zero to one. This process is known as Grey relational generation. Next, based on normalized experimental data, the Grey relational coefficient is calculated to represent the correlation between the desired and the actual experimental data. Then overall Grey relational grade is determined by averaging the Grey relational coefficient corresponding to selected responses [9]. The overall performance characteristic of the multiple response process depends on the calculated Grey relational grade. This approach converts a multiple-response process-optimization problem into a single-response optimization situation with the objective function of the overall Grey relational grade. The optimal parametric combination is then evaluated, which would result in the highest Grey relational grade.

The optimal factor setting for maximizing the overall Grey relational grade can be performed using the Taguchi method [9,10].

In Grey relational generation, the normalized F and Ra corresponding to the smaller-the-better (SB) criterion which can be expressed as:

$$x_i(k) = \frac{\max y_i(k) - y_i(k)}{\max y_i(k) - \min y_i(k)} \tag{1}$$

MRR should follow the larger-the-better (LB) criterion, which can be expressed as:

$$x_j(k) = \frac{y_j(k) - \min y_j(k)}{\max y_j(k) - \min y_j(k)} \tag{2}$$

where $x_i(k)$ and $x_j(k)$ are the value after the Grey relational generation for the SB and LB criteria, respectively. Min $y_i(k)$ is the smallest value of $y_i(k)$ and for the kth response, and max $y_i(k)$ is the largest value of $y_i(k)$ for the kth response [9]. An ideal sequence is $x_0(k)$ (k=1, 2,…,m) for the responses. The definition of the Grey relational grade in the course of the Grey relational analysis is to reveal the degree of relation between the 9 sequences [$x_0(k)$ and $x_i(k)$, $k = 1,2,…,m$ and $i = 1,2,…,9$]. The Grey relational coefficient $\xi_i(k)$ can be calculated as:

$$\xi_i(k) = \frac{\Delta_{\min} - \psi\Delta_{\max}}{\Delta_{0i}(k) + \psi\Delta_{\max}} \tag{3}$$

where $\Delta_{0i} = \left\|x_0(k) - x_i(k)\right\|$ is the difference of the absolute value $x_0(k)$ and $x_i(k)$; ψ is the distinguishing coefficient $0 \leq \psi \leq 1$; $\Delta_{\min}(k) = \forall j^{\min} \in i \forall k^{\min}$ $\left\|x_0(k) - x_j(k)\right\|$ is the smallest value of Δ_{0i}; and $\Delta_{\max}(k) = \forall j^{\max} \in i \forall k^{\max} \left\|x_0(k) - x_j(k)\right\|$ is the largest value of Δ_{0i}. After averaging the Grey relational coefficients, the Grey relational grade γ_i can be computed as:

$$\gamma_i = \frac{1}{n}\sum_{k=1}^{n}\xi_i(k) \tag{4}$$

where n is the number of process responses. The higher value of the Grey relational grade corresponds to an intense relational degree between the reference sequence $x_0(k)$ and the given sequence $x_i(k)$. The reference sequence $x_0(k)$ represents the best process sequence; therefore, a higher Grey relational grade means that the corresponding parameter combination is closer to the optimal [9]. The mean response for the Grey relational grade with its grand mean and the main effect plot of the Grey relational grade are very important because the optimal process condition can be evaluated from this plot [9].

3 EXPERIMENTAL PROCEDURE AND TEST RESULTS

3.1 Experimental Details

The cutting experiments were carried out on an experimental lathe setup using a HSS cutting tool for the machining of the AISI 1050 steel bar, which is 30 mm in diameter and 80 mm in length. The mechanical properties and percent composition of the workpiece material is listed in **Table 1**.

A *Phynix TR-100* model surface-roughness tester was used to measure the surface roughness of the machined samples. The cut-off length (λ) was chosen as 0.3 for each roughness measurement. An average of six measurements of the surface roughness was taken to use in the multi-criteria optimization. Also, the MRR (mm^3/min) was calculated using Eq. (5);

$$MRR = 1000 \ Vfd \qquad (5)$$

where f/(mm/r) denotes the feed rate, d/mm describes the cutting depth and V/(m/min) represents the cutting speed of the turning operation.

3.2 Process Parameters and Test Results

In full factorial design, the number of experimental runs exponentially increases as the number of factors, as well as their level increases. This results in a huge experimentation cost and considerable time periods [9]. So, in order to compromise these two adverse factors and to search for the optimal process condition through a limited number of experimental runs Taguchi's L_9 orthogonal array consisting of 9 sets of data was selected to optimize the multiple performance characteristics of the turning process. Experiments were conducted with the process parameters given in **Table 2**, to obtain the machined surface on the AISI 1050 medium-carbon steel. The feasible space for the cutting parameters was defined by varying the cutting speed in the range 110–600 m/min, the feed rate in the range 0.2–0.6 mm/min, and the depth of cut in the range 0.5–1.5 mm.

The initial cutting parameters were selected as: cutting speed of 110 m/min; feed rate of 0.20 mm/min; and depth of cut of 0.5 mm. In the cutting parameter design, three levels of the cutting parameters were selected, as shown in **Table 2**. In order to prevent a sudden increase of the cutting forces due to the dullness of the cutting edge, the HSS tool was changed after three repetitions of each experiment.

Table 3 shows the selected design matrix based on the Taguchi L_9 orthogonal array consisting of 9 sets of coded conditions and the experimental results for the responses of F, Ra and MRR. All these data were utilized for the analysis and evaluation of the optimal parameter combination required to achieve the desired quality within the experimental domain.

4 PARAMETRIC OPTIMIZATION OF THE CUTTING PROCESS

4.1 Evaluation of the Optimal Process Condition

First, by using Eqs. (1) and (2), the experimental data were normalized to obtain the Grey relational generation [9]. The normalized data and $\Delta_{0i}(k)$ for each of the responses are listed in **Table 4** and **Table 5**, respectively. For MRR the *larger-the-better (LB)* and for F and Ra the *smaller-the-better (SB)* criteria were selected.

Table 3: Orthogonal array L_9 of the experimental runs and results
Tabela 3: Ortogonalna razporeditev L_9 eksperimentov in rezultati

Run no	Parameter level			Experimental results		
	V	f	d	MRR/ (mm^3/min)	F/N	Ra/μm
1	1	1	1	0.11	123	0.87
2	1	2	2	0.44	179	2.33
3	1	3	3	0.99	364	6.62
4	2	1	2	0.60	166	1.98
5	2	2	3	1.80	295	3.82
6	2	3	1	0.90	255	3.96
7	3	1	3	1.80	340	0.92
8	3	2	1	1.20	218	1.22
9	3	3	2	3.60	268	5.60

Table 1: Chemical and mechanical properties of AISI 1050 medium carbon steel
Tabela 1: Kemična sestava in mehanske lastnosti jekla AISI 1050 s srednjim ogljikom

Chemical composition w/%	C	P	S	Mn	Cr	Fe	Ni	Cu
	0.49	0.02	0.02	0.78	0.08	97.99	0.10	0.26
Mechanical properties	Yield strength (MPa)		Tensile strength (MPa)		Elongation (%)		Vickers Hardness (HV)	
	365		636		24		261	

Table 2: Cutting parameters and their limits
Tabela 2: Parametri rezanja in njihove meje

Cutting Parameters	Notation	Unit	Levels of factors		
			1	2	3
Cutting speed	V	m/min	110*	300	600
Feed rate	f	mm/min	0.2*	0.4	0.6
Depth of cut	d	mm	0.5*	1.0	1.5

*Initial cutting parameter

Table 4: Grey relational generation of each performance characteristics
Tabela 4: Grey relacijska generacija vsake karakteristike performance

Run no	MRR	F	Ra
	Larger-the-better	Smaller-the-better	Smaller-the-better
Ideal sequence	1.000	1.000	1.000
1	0.000	1.000	1.000
2	0.095	0.768	0.746
3	0.252	0.000	0.000
4	0.140	0.822	0.807
5	0.484	0.286	0.487
6	0.226	0.452	0.463
7	0.484	0.100	0.991
8	0.312	0.606	0.939
9	1.000	0.398	0.177

Table 5: Evaluation of $\Delta_{0i}(k)$ for each of the responses
Tabela 5: Ocena $\Delta_{0i}(k)$ za vsak odgovor

Run no	*MRR*	*F*	*Ra*
Ideal sequence	1.000	1.000	1.000
1	1.000	0.000	0.000
2	0.905	0.232	0.254
3	0.748	1.000	1.000
4	0.860	0.178	0.193
5	0.516	0.714	0.513
6	0.774	0.548	0.537
7	0.516	0.900	0.009
8	0.688	0.394	0.061
9	0.000	0.602	0.823

Table 6 shows the calculated Grey relational coefficients (with the weights of $\psi_{MRR} = 0.33$, $\psi_F = 0.33$ and $\psi_{Ra} = 0.33$) of each performance characteristic using Eq. (3).

Table 6: Grey relational coefficient of each performance characteristics ($\psi_{MRR} = 0.33$, $\psi_F = 0.33$ and $\psi_{Ra} = 0.33$)
Tabela 6: Grey odvisnostni koeficient za vsako značilnost performance ($\psi_{MRR} = 0.33$, $\psi_F = 0.33$ and $\psi_{Ra} = 0.33$)

Run no	*MRR*	*F*	*Ra*
Ideal sequence	1.000	1.000	1.000
1	0.248	1.000	1.000
2	0.267	0.587	0.565
3	0.306	0.248	0.248
4	0.277	0.649	0.631
5	0.390	0.316	0.391
6	0.299	0.376	0.380
7	0.390	0.268	0.974
8	0.324	0.456	0.844
9	1.000	0.354	0.286

The Grey relational coefficients, given in **Table 7**, for each response have been accumulated by using Eq. (4) to evaluate the Grey relational grade, which is the overall representative of all the features of the cutting-process quality. Thus, the multi-criteria optimization problem has been transformed into a single equivalent objective function optimization problem using a combination of

the Taguchi approach and Grey relational analyses. The higher is the value of the Grey relational grade, the corresponding factor combination is said to be close to the optimal [9].

Table 7: Grey relational grade
Tabela 7: Grey stopnja odvisnosti

Run no	Grey relational grade	Rank
1	0.7119	1
2	0.4683	6
3	0.2648	9
4	0.5139	5
5	0.3623	7
6	0.3483	8
7	0.5388	3
8	0.5360	4
9	0.5414	2

The signal-to-noise (*S/N*) ratio is a measure of the magnitude of a data set relative to the standard deviation. If the S/N is large, the magnitude of the signal is large relative the noise, as measured with the standard deviation [11]. Table 8 shows the *S/N* ratio based on the *larger-the-better* criterion for the overall Grey relational grade calculated using Eq. (6).

$$S/N = -10 \log \left[\frac{1}{n} \sum_{i=1}^{n} \frac{1}{y_i^2} \right] \qquad (6)$$

where *n* is the number of measurements, and y_i is the measured characteristic value.

Table 8: *S/N* ratio for overall Grey relational grade
Tabela 8: *S/N* razmerje za splošno Grey stopnjo

Run no	S/N
1	−2.59
2	−6.59
3	−11.54
4	−5.78
5	−8.82
6	−9.16
7	−5.37
8	−5.42
9	−5.33

Table 9: Response Table for the mean Grey relational grade
Tabela 9: Tabela odgovorov za povprečno Grey stopnjo odvisnosti

Factors	Grey relational grade			
	Level 1	*Level 2*	*Level 3*	*max-min*
V	0.49	0.41	0.54	0.13
f	0.60	0.46	0.38	0.22
d	0.54	0.51	0.39	0.15

Total mean Grey relational grade = 0.48

A graphical representation of the *S/N* ratio for the overall Grey relational grade is shown in **Figure 2**. The dashed line is the value of the total mean of the *S/N* ratio.
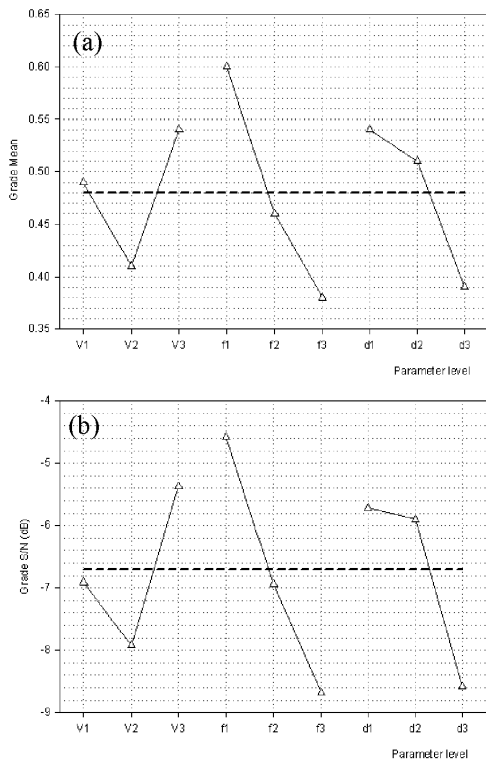
Figure 2: (a) Mean plot, (b) *S/N* plot for the Grey relational grade
Slika 2: (a) Povprečna odvisnost, (b) *S/N* odvisnost za Grey stopnjo odvisnosti

As indicated in **Figure 2**, the optimal condition for the turning of the AISI 1050 medium-carbon steel becomes $V_3 f_1 d_1$. **Table 9** shows the mean Grey relational grade ratio for each level of the process parameters.

4.2 Analysis of Variance (ANOVA)

The purpose of the analysis of variance (ANOVA) is to investigate which turning parameters significantly affect the performance characteristics [8–10]. This is accomplished by separating the total variability of the grey relational grades, which is measured by the sum of the squared deviations from the total mean of the grey relational grade, into contributions from each of the turning parameters and the error [9]. Thus;

$$SS_T = SS_F + SS_e \qquad (7)$$

where

$$SS_T = \sum_{j=1}^{p} (\gamma_j - \gamma_m)^2 \qquad (8)$$

SS_T – Total sum of the squared deviations about the mean
γ_j – Mean response for the jth experiment
γ_m – Grand mean of the response
p – Number of experiments in the orthogonal array
SS_F – Sum of the squared deviations due to each factor
SS_e – Sum of the squared deviations due to error

In addition, the *F* test was used to determine which turning parameters have a significant effect on the per-

formance characteristic. Usually, the change of the turning parameter has a significant effect on the performance characteristics when the *F* value is large [8–10]. The ANOVA for the overall Grey relational grade is shown in **Table 10**.

Table 10: ANOVA results of turning process parameters
Tabela 10: ANOVA rezultati parametrov procesa struženja

Parameter	Degree of Freedom	Sum of Square	Mean Square	F	Contribution (%)
V	2	0.026	0.013	1.21	17.81
f	2	0.071	0.035	3.27	48.63
d	2	0.039	0.019	1.79	26.71
Error	2	0.010	0.011		6.85
Total	8	0.158			100

According to this analysis, the most effective parameters with respect to the material-removal rate, the cutting force and the surface roughness are the feed rate, the depth of cut and the cutting speed. The percentage contribution indicates the relative power of a factor to reduce the variation. For a factor with a high percentage contribution, there is a great influence on the performance. The percent contributions of the cutting parameters on the material-removal rate, the cutting force and the surface roughness are shown in Table 10 and **Figure 3**. The feed rate was found to be the major factor affecting the material-removal rate, the cutting force and the surface roughness (48.63 %), whereas the depth of cut (26.71 %) and the cutting speed (17.81 %) were found to be the second- and third-ranking factors respectively.

4.3 Confirmation Test

After evaluating the optimal parameter settings, the next step is to predict and verify the enhancement of the quality characteristics using the optimal parametric combination [9]. The estimated Grey relational grade $\hat{\gamma}$ using the optimal level of the design parameters can be calculated as:

$$\hat{\gamma} = \gamma_m + \sum_{i=1}^{o} (\overline{\gamma}_j - \gamma_m) \qquad (9)$$

where γ_m is the total mean Grey relational grade, $\overline{\gamma}_i$ is the mean Grey relational grade at the optimal level, and
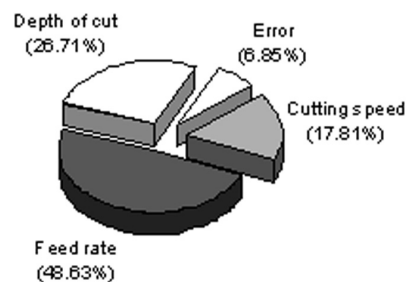

Figure 3: Contribution percentage of the cutting parameters
Slika 3: Prispevni procent parametrov rezanja

Table 11: Results of confirmation test
Tabela 11: Rezultati potrditvenega preizkusa

	Initial factor settings	Optimal process condition	
		Prediction	Experiment
Factor levels	$V_1 f_1 d_1$	$V_3 f_1 d_1$	$V_3 f_1 d_1$
MRR/ (mm³/min)	0.11		0.30
F/N	123		115
Ra/μm	0.87		0.65
S/N ratio of overall Grey relational grade	–2.59	–2.21	–-2.18
Overall Grey relational grade	0.71	0.72	0.77

Improvement in Grey relational grade = 0.06

o is the number of the main design parameters that affect the quality characteristics [9]. **Table 11** indicates the comparison of the predicted tensile strength and elongation with that of the actual by using the optimal turning conditions. Good agreement between the actual and the predicted results has been observed (the improvement in the overall Grey relational grade was found to be as 0.20).

In the Taguchi method, the only performance feature is the overall Grey relational grade and the aim should be to search for a parameter setting that can achieve the highest overall Grey relational grade [9]. The Grey relational grade is a representative of all the individual performance characteristics. In the present study, the objective functions were selected in relation to the parameters of the material-removal rate, the cutting force and the surface roughness. The importance weights of the material-removal rate, the cutting force and the surface roughness were equally adjusted to be 0.33.

The results show that using the optimal parameter setting ($V_3 f_1 d_1$) causes a lower cutting force and surface roughness with a higher material removal rate and hence a better surface finish.

5 CONCLUSIONS

In this study, the Grey-based Taguchi method was applied for the multiple performance characteristics of turning operations. A grey relational analysis of the material-removal rate, the cutting force and the surface roughness obtained from the Taguchi method reduced from the multiple performance characteristics to a single performance characteristic which is called the grey relational grade. Therefore, the optimization of the complicated multiple performance characteristics of the processes can be greatly simplified using the Grey-based

Taguchi method. It is also shown that the performance characteristics of the turning operations, such as the material removal rate, the cutting force and the surface roughness are greatly enhanced by using this method.

6 REFERENCES

[1] W. H. Yang, Y. S. Tarng, Design Optimization of cutting parameters for turning operations based on the Taguchi method, Journal of Materials Processing Technology, 84 (**1988**), 122–129

[2] P. L. B. Oxley, Modelling machining processes with a view to their optimization and the adaptive control of metal cutting machine tools, Robot. Comput.-Integrated Manuf., 4 (**1988**), 103–119

[3] G. Chryssolouris, M. Guillot, A comparison of statistical and AI approaches to the selection of process parameters in intelligent machining, ASME J. Eng. Ind., 112 (**1990**), 122–131

[4] Y. Yao, X. D. Fang, Modelling of multivariate time series for tool wear estimation in finish turning, Int. J. Mach. Tools Manuf., 32 (**1992**) 4, 495–508

[5] C. Zhou, R A. Wysk, An integrated system for selecting optimum cutting speeds and tool replacement times, Int. J. Mach. Tools Manuf. 32 (**1992**) 5, 695–707

[6] M. S. Chua, M. Rahman, Y. S. Wong, H. T. Loh, Determination of optimal cutting conditions using design of experiments and optimization techniques, Int. J. Mach. Tools Manuf., 33 (**1993**) 2, 297–305

[7] A. Bendell, J. Disney, W. A. Pridmore, Taguchi methods: Applications in world industry, IFS Publications, UK, 1989

[8] D. C. Montgomery, Design and analysis of experiments, Wiley, Singapore, 1991

[9] S. Datta, A. Bandyopadhyay, P. K. Pal, Grey-based taguchi method for optimization of bead geometry in submerged arc bead-on-plate welding. Int J Adv Manuf Technol., 39 (**2008**) 11, 1136–1143

[10] U. Esme, M. Bayramoglu, Y. Kazancoglu, S. Özgun, Optimization of weld bead geometry in TIG welding process using Grey Relation Analysis and Taguchi Method, Mater. Tehnol., 43 (**2009**), 143–149

[11] D. S. Holmes, A. E. Mergen, Signal to noise ratio – What is the right size, www.qualitymag.com/.../Manuscript%20Holmes%20&%20 Mergen.pdf, USA, 1996, 1–6

THERMODYNAMIC CONDITIONS FOR THE NUCLEATION OF BORON COMPOUNDS DURING THE COOLING OF STEEL

TERMODINAMIČNI POGOJI ZA NUKLEACIJO BOROVIH SPOJIN PRI OHLAJANJU JEKLA

Zdeněk Adolf, Jiří Bažan, Ladislav Socha

VŠB-Technical University of Ostrava, Department of Metallurgy, 17. listopadu 15/2172, 708 33 Ostrava-Poruba, Czech Republic
zdenek.adolf@vsb.cz

The higher the value of the product of boron and oxygen concentrations, or of boron and nitrogen concentrations, than the value corresponding to the balance for the given temperature, is the thermo-dynamic criterion for the nucleation of a new phase (B_2O_3 or BN). It follows from the calculations that the theoretical temperature of the beginning of B_2O_3 nucleation is higher than the temperature of the beginning of BN nitride nucleation. During the solidification and cooling down of steel the boron oxide will be formed preferentially before the boron nitride.

Keywords: boron steel, nucleation, non-metallic inclusions

Večji produkt vsebnosti bora in kisika ter bora in dušika kot ravnotežna vrednost pri izbrani temperaturi je termodinamični pogoj za nukleacijo nove faze (B_2O_3 oz. BN). Izračuni so pokazali, da je teoretično temperatura začetka nukleacije oksida B_2O_3 višja kot pri nitridu BN. Zato bo pri ohlajanju jekla borov oksid nastal pred nitridom.

Ključne besede: bor, jeklo, nukleacija, nekovinski vključki

1 INTRODUCTION

This paper presents a thermodynamic analysis of the probability of the formation of boron oxide and nitride in boron- and nitrogen-microalloyed stainless steels. The steels are designated for forgings for the production of valves of nuclear power plants' primary circuits and their chemical composition is given in **Table 1**.

**Table 1:** Chemical composition of the steel (in mass fractions w/%)
Tabela 1: Kemična sestava jekel (v masnih deležih w/%)

Element. (w/%)							
C	0.04	S	0.001	V	0.05	Nb	0.017
Mn	1.57	Cr	17.5	W	0.02	B	0.004
Si	0.6	Ni	10.5	Al	0.050	N	0.0126
P	0.020	Mo	0.07	Ti	0.40		

The objective of this work is to determine at which temperatures the B_2O_3 or BN is formed during the cooling and solidification of the steel. The formation of a new phase (inclusion) is related to the content of boron, nitrogen and oxygen in the steel.

2 THERMODYNAMIC BALANCE

The temperature dependencies of the Gibbs energy for the formation of B_2O_3 and BN were derived from table data[1, 2] with the use of the equations:

$$[B] + \tfrac{3}{2}[O] = \tfrac{1}{2} B_2O_{3(l)} \qquad (1)$$

$$[B] + [N] = BN_{(s)} \qquad (2)$$
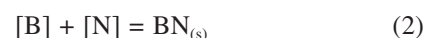
$$\Delta G_1^0 = -411\ 990 + 143{,}585\ T \qquad (3)$$

$$\Delta G_2^0 = -227\ 737 + 97{,}95\ T \qquad (4)$$

Due to the fact that the melting temperature of B_2O_3 is 450 °C, this oxide is at the temperatures of steel solidification in the liquid state[2].

It is possible to derive from equations (3) and (4) the following relations for the temperature dependencies of the equilibrium constants:

$$\lg K_1 = \frac{21517}{T} - 7{,}50 \qquad (5)$$

$$\lg K_2 = \frac{11894}{T} - 5{,}116 \qquad (6)$$

The following is valid for the equilibrium constants of the reactions (1) and (2):

$$K_1 = \frac{a_{B_2O_3}^{1/2}}{\left(a_{[B]} \cdot a_{[O]}^{3/2}\right)_{equilibrium}} \qquad (7)$$

$$K_2 = \frac{a_{BN}}{\left(a_{[B]} \cdot a_{[N]}\right)_{equilibrium}} \qquad (8)$$

Assuming that pure boron oxide and boron nitride are formed, it is possible to consider their activities to be equal to one. It is similarly possible to assume unequivocally that the solutions of boron, oxygen and nitrogen in steel are diluted and that the activities of these elements

are equal to a mass percentage. It is then possible to adjust the equations (7) and (8) to these forms:

$$\left([B]\cdot[O]^{3/2}\right)_{equilibrium} = \frac{1}{K_1} \qquad (9)$$

$$\left([B]\cdot[N]\right)_{equilibrium} = \frac{1}{K_2} \qquad (10)$$

Due to the fact that the equilibrium constants K_1 and K_2 are a function of temperature only in accordance with equations (5) and (6), the equilibrium products of the concentrations of boron and oxygen, as well as boron and nitrogen, depend only on the temperature (see equations (11) and (12)) and can be calculated from the temperature dependencies.

$$\lg\left([B]\cdot[O]^{3/2}\right)_{equilibrium} = -\frac{21517}{T} + 7{,}50 \qquad (11)$$

$$\lg\left([B]\cdot[N]\right)_{equilibrium} = -\frac{11894}{T} + 5{,}116 \qquad (12)$$

It is subsequently possible to affirm logically that the formation of boron trioxide or boron oxide at the temperature T is conditioned by a higher value of the real product of boron and oxygen, or a boron and nitrogen concentration that would correspond to the equilibrium.

$$\left([B]\cdot[O]^{3/2}\right)_{real} \geq \left([B]\cdot[O]^{3/2}\right)_{equilibrium} \qquad (13)$$

$$\left([B]\cdot[N]\right)_{real} \geq \left([B]\cdot[N]\right)_{equilibrium} \qquad (14)$$

It follows from equations (11) and (12) that with decreasing temperature the value of equilibrium products (13) and (14) also decreases, and therefore the probability of the formation of the inclusions B_2O_3 and BN increases, since the real products (13) and (14) remain constant.

3 DISCUSSION OF THE RESULTS

The derived relationships were applied to the steel microalloyed with boron and nitrogen of required chemical composition – see **Table 1**.

The theoretical dependencies of the temperatures of the beginning of formation of the B_2O_3 or BN on the content of oxygen and nitrogen are given in **Figures 1 and 2**.

These dependencies were calculated from equations (5) and (6), adjusted for mass fractions 0.001 %, 0.006 %, 0.03 % and 0.05 % of boron.

It follows from **Figure 2** that, for example, the theoretical temperature of the beginning of nucleation of BN nitride is for the nitrogen content of 100 µg/g (ppm) in the interval 903 °C, 1001 °C, 1104 °C and 1040 °C, or for 200 µg/g of nitrogen in the interval 939 °C, 10043 °C, 1154 °C and 1193 °C. The theoretical temperature for the start of nucleation of the oxide B_2O_3 is for the achieved oxygen contents (10 µg/g) higher, i.e., 1161 °C,
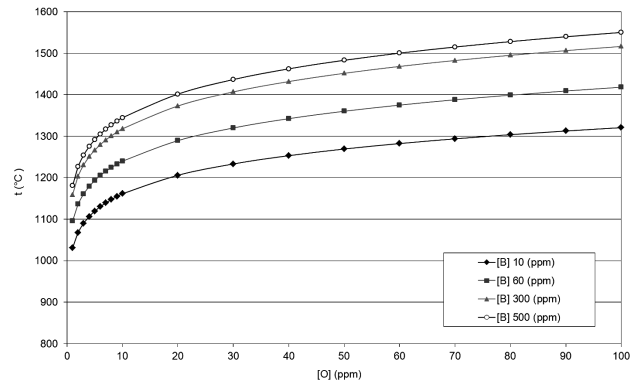

Figure 1: Dependence of the beginning temperature of formation of B_2O_3 and the content of oxygen in steel
Slika 1: Začetna temperatura tvorbe B_2O_3 v odvisnosti od vsebnosti kisika v jeklu
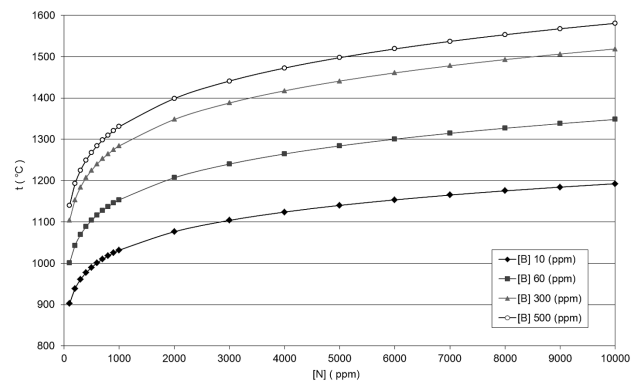

Figure 2: Dependence of the starting temperature on the formation of BN and the content of nitrogen in steel
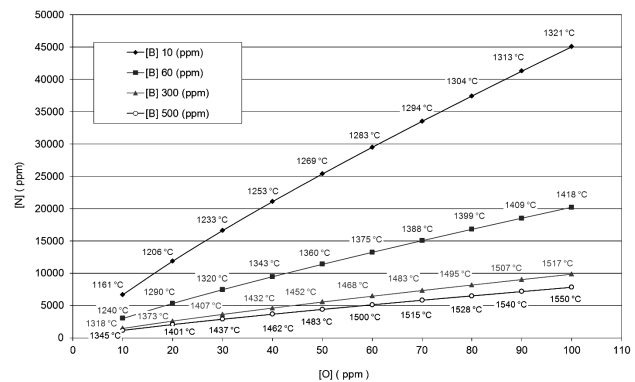**Slika 2:** Začetna temperatura tvorbe B_2O_3 v odvisnosti od vsebnost dušika v jeklu

Figure 3: Equilibrium temperatures and equilibrium contents of nitrogen corresponding to the oxygen content in steel of 10–100 µg/g
Slika 3: Ravnotežne temperature in ravnotežne vsebnosti dušika pri vsebnosti 10–100 µg/g kisika v jeklu

1240 °C, 1318 °C and 1345 °C, and for 20 µg/g of oxygen it is 1206 °C, 1290 °C, 1373 °C and 1402 °C. It follows, therefore, that boron oxide will be formed preferentially before boron nitride during the cooling of the steel.

For the steels with the above-mentioned boron contents the equilibrium temperatures and equilibrium

nitrogen contents corresponding to 10–100 μg/g of oxygen in steel are shown in **Figure 3**. It is evident from the figure that B_2O_3 oxides can be formed only at higher contents of oxygen than would correspond to an equilibrium (right to the curve). Similarly, boron nitrides can be formed only at higher nitrogen contents than would correspond to an equilibrium (above the curve), since inequalities (13) and (14) are fulfilled.

4 CONCLUSIONS

The thermodynamic balance of probability for the formation of oxide B_2O_3 and nitride BN in boron-microalloyed steels was calculated. The balance proved that the oxide is more stable than the boron nitride and, therefore, during the cooling of steels it is formed preferentially.

5 REFERENCES

[1] J. Fruehan, et al. The Making Shaping and Treating of Steel. Pittsburgh 1998, 767 pp., ISBN 0-930767-02-0

[2] J. Leitner. Database of thermodynamic data for admixtures in iron based melts. VŠCHT Praha, 2002, 23 pp.

A MICRO-DAMAGE INVESTIGATION ON A LOW-ALLOY STEEL TESTED USING A 7.62-mm AP PROJECTILE

RAZISKAVA MIKROPOŠKODB MALOLEGIRANEGA JEKLA PO PREIZKUSU S KROGLO AP 7,62 mm

Teyfik Demir[1], Mustafa Übeyli[2]

[1]TOBB University of Economics and Technology, Engineering Faculty, Mechanical Engineering, 06560 Ankara - TÜRKİYE
[2]Osmaniye Korkut Ata University, Engineering Faculty, Mechanical Engineering, 80000 Osmaniye - TÜRKİYE
mubeyli@gmail.com

Low-alloy steels have been widely used as an armor material in defense systems due to their superior mechanical and weldability properties. In this study, microdamage formation in an AISI 4140 steel, which was hit by 7.62-mm armor-piercing (AP) projectile, was investigated. Analyses of the microstructure and microhardness after ballistic testing were performed to correlate the microstructure-property relationship. Two different types of adiabatic shear band (ASB) were observed in the tested samples. The experimental results indicated that the type and hardness of the bands were strongly related to the hardness and ballistic performance of the steel specimens.

Keywords: high-strength steel, adiabatic shear band, armor.

Malolegirana jekla se uporabljajo za obrambne sisteme predvsem zaradi njihovih boljših lastnosti in varivosti. V tem delu je raziskan nastanek poškodbe v jeklu AISI 4140 po udarcu prebojne krogle 7,62 mm v oklep. Mikrostruktura in mikrotrdota sta po balističnem preizkusu korelirana z odnosom mikrostruktura-lastnosti. V preizkusnih vzorcih sta opaženi dve vrsti adiabatskih strižnih pasov (ASB). Rezultati so pokazali, da sta vrsta in trdota pasov zelo povezani s trdoto in balističnimi lastnostmi vzorcev jekla.

Ključne besede: visokotrdna jekla, adiabatski strižni pasovi, oklep

1 INTRODUCTION

Microstructural changes, i.e., phase transformations, distortion of grains, elongation of grains, grain refinement, are observed in metallic materials that are exposed to high strain rates and very large strains. With these changes, bands that are different from the original matrix in nature or alignment may form. These bands are termed adiabatic shear bands and they occur in a number of processes, such as dynamic impact, metal forming, ballistic testing, machining and high-strain-rate deformation. The adiabatic shear band phenomenon was first discovered by Zener and Hollomon [1]. However, studies on the adiabatic shear band formation accelerated after the year 1970. The thermomechanical instability caused by the presence of local inhomogeneity, inducing local deformation and heating, results in the formation of shear bands [2]. Adiabatic shearing is a special case where the heat generated in the localized bands cannot be transferred easily to the surrounding material due to the strain rate and thermal properties of the material [2]. However, in a real situation some of the heat loss to the surrounding material always occurs. The reason for using the adiabatic term is to indicate that a large part of the heat is retained in the band [2]. This leads to a local temperature increase which may cause a microstructure change in the material [3]. Adiabatic shearing can lead to a catastrophic failure in materials under high strain rate

deformation [4,5]. There are two general classifications of the ASBs: deformed and transformed [2]. In the deformed ASBs, there is no change in the microstructure of the materials, but the grains or structure are highly distorted. On the other hand, in the transformed bands, a crystallographic phase change takes place.

Derep [6] investigated the microstructure transformation induced by the adiabatic shearing in an armor steel tested using a hollow charge. It was observed that a fine-grained, equiaxed structure of delta ferrite consisting of very narrow martensite laths formed in the center of ASBs. In another study, Wittman et al. [7] investigated the adiabatic shear-band formation in AISI 4340 steel. Also, an investigation of the adiabatic shear band formation in different steels (AISI 1018, AISI 4340 and HY-100) was performed after applying torsion loads at high strain rates [8]. It was mentioned that the shear bands were produced by the dynamic torsional deformation in all cases and they were of the deformed type for the steel AISI 1018, whereas those were transformed for the steel AISI 4340. In addition, Bassim [9] studied ASB formation in the AISI 4340 steel during high strain rate deformation using a torsional Split Hopkinson Bar System. It was also reported that ASBs initiated at local defects and inhomogeneities. In addition, the specimen geometry and dimensions were found to be contributing factors to the development of ASBs. Furthermore, Duan et al. [10] examined the forma-

tion of adiabatic shear bands in two different grades of steel (medium carbon steel and 30CrMnMo) subjected to the impact of tungsten projectiles. They reported that three kinds of ASBs formed in the 30CrMnMo, while the medium carbon steel did not easily produce ASBs. Moreover, Hu et al. [11] investigated the ASB formation in various steels (4130, AISI 1045, modified rolled homogeneous armor steel and AerMet 100) tested by 44 grain-fragment simulating projectiles. It was shown that transformed bands were found in the steels, 4130, modified rolled homogeneous armor steel and AerMet 100, while deformed bands were found in the AISI 1045. Recently, the effect of heat treatment on the ASBs in AISI 4340 steel tested with the Split Hopkinson Pressure Bar was studied [12]. It was concluded that heat treatment did not cause any significant effect on the microstructure and hardness of ASBs. In a more recent work, Lins et al. [13] made a microstructural characterization of the ASBs in an interstitial-free steel deformed at high strain rates ($>2.8 \cdot 10^4$ s^{-1}) in a Split Hopkinson Pressure Bar. They found that the deformation twins occurred throughout the microstructure. Recently, a microstructural study on the AISI 4340 and DIN 100Cr6 steels, tested with a 7.62-mm AP projectile, was carried out [14]. It was stated that the impact of the AP projectile resulted in the formation of ASBs in all the samples having different hardness levels [14]. In addition to the studies conducted on steels, shear band formation in copper [15–17], aluminum [18,19] and refractory metals [20–23] was also examined.

The ballistic behavior of the high-strength, low-alloy steel AISI 4140 with respect to its hardness and areal density was determined against a 7.62-mm armor-piercing (AP) projectile in our previous work [24]. In this study, a micro-damage analysis in this type of steel after the ballistic testing with the 7.62-mm AP projectile was made.

2 EXPERIMENTAL PROCEDURE

The AISI 4140 steel is a high-strength, low-alloy steel that can be strengthened significantly by applying a martensite formation heat treatment. This steel is used mainly in the automotive industry and for structural applications. The AISI 4140 steel used in this work had 0.40 % C, 1.0 % Cr, 0.2 % Mo, 0.7 5% Mn and 0.2 % Si (mass fractions, $w/\%$). Experimental studies were based mainly on two lines: a microstructural examination and a microhardness measurement of the ASBs formed in AISI 4140 steel that was subjected to the impact of a 7.62-mm AP projectile [24]. This type of projectile is widely used in NATO armies. Its specification can be found in ref. [24]. The thicknesses of the steel samples utilized in this work were 7.2 mm, 9 mm, 10.8 mm, 12.7 and 14.4 mm. Furthermore, three hardness levels (38 HRC, 50 HRC and 60 HRC) were considered for each thickness of the steel sample for the comparison with the previous study [14]. In coding of the steel specimens, the letters A, B and C were used to indicate the hardness levels of 38 HRC, 50 HRC and 60 HRC, respectively. In addition, the
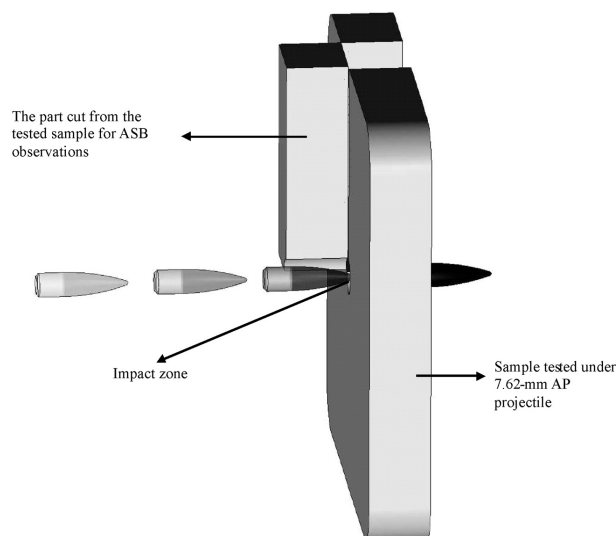

Figure 1: Location of samples for ASB investigation
Slika 1: Mesto odvzema vzorcev za preiskave ASB

numbers, 1, 2, 3, 4 and 5 following these letters were utilized to refer to the steel thickness of 7.2 mm, 9 mm, 10.8 mm, 12.7 and 14.4 mm, respectively.

The microstructural changes in the specimens were firstly determined using an optical microscope to see the type and distribution of the ASBs in the material. For this purpose, the AISI 4140 steel specimens were etched using 5 % nital solution to see both the phase(s) and the adiabatic shear bands clearly. Next, the microstructures of the samples were investigated at the impact surfaces through the thickness of the steel and parallel to the projectile motion (**Figure 1**). Secondly, an analysis using a scanning electron microscope (SEM) was carried out to resolve the microstructure of the white ASBs more clearly. Moreover, a representative chemical content of the precipitate was determined by energy-dispersive X-ray (EDX) analysis. Finally, the microhardness measurements were also made to determine the hardness of the different types of adiabatic shear bands formed upon impact.

3 EXPERIMENTAL RESULTS AND DISCUSSION

Typical microstructures of the sample before testing are represented in **Figure 2**. Due to the applied heat treatment, all the samples had a tempered martensite phase containing ferrite with very small iron-carbide islands. This type of phase provides the best combination of strength and toughness for a low-alloy steel. For this reason, this type of microstructure is frequently chosen to be used in high-strength applications.

The kinetic energy of the projectile was able to generate ASBs in the AISI 4140 steel. Its velocity was measured to be (782 ± 5.4) m/s [24]. The most important factor in ballistic studies is the velocity of the impact. Damage types change significantly with the impact velocity. The velocities between 700 m/s and 3000 m/s are termed intermediate impact velocities, which cause
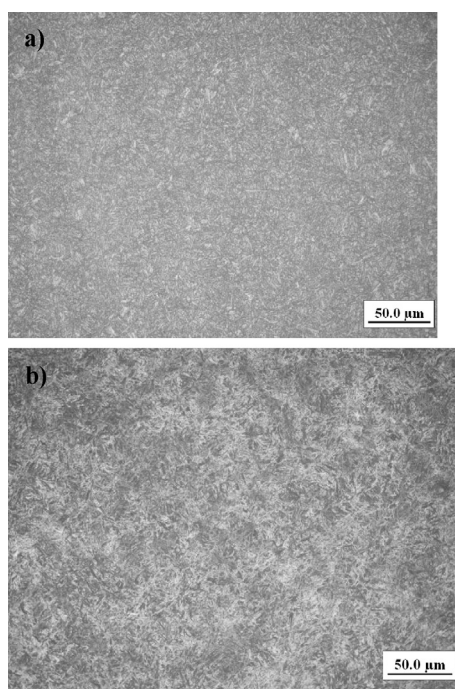
Figure 2: Microstructures of the sample AISI 4140 with a hardness of a) 40 HRC, b) 60 HRC before testing
Slika 2: Mikrostruktura vzorca AISI 4140 s trdotama a) 40 HRC in b) 60 HRC pred preizkusom

quasi-static and dynamic damage to the target material [25]. Therefore, the projectile generates compressive shock waves on impact. These waves induce phase transformations and chemical changes, which can harden metals to a great extent [25].

After the ballistic testing of the steel samples, some microstructural changes were recorded. These changes were mainly the formation of ASBs. A general view of a typical ASB in the investigated samples is seen in **Figure 3**. One can see that the ASBs were formed in all samples under the effect of AP projectile and appear as long white strips. However, the density of the ASBs varied significantly with respect to the hardness and thickness of the samples. The microstructure of the deformed ASBs in the specimen group A was very similar to that of the matrix material. In addition, the extent of the ASB formation was fairly low in comparison to the other groups B and C. Furthermore, only deformed bands were observed in the samples of group A and distortion in the bands was rather low. On the other hand, in the specimen groups B and C, both deformed and transformed bands were found. Moreover, a higher distortion in the deformed bands induced by shear in these specimen groups was seen significantly in comparison to the samples of group A. In our previous study [14], the transformed band formation was also found for the steel samples (AISI 4340 and DIN 100Cr6) with the hardness of 49 HRC and 59 HRC even though the most of the bands were of the deformed type in all the samples.

The thickness of the bands seen in the investigated samples is given in **Table 1**. It changed between 19 μm and 56 μm, depending on the types of band and the sample. This indicates that the local deformation and heating in the samples is taking place. **Figure 4** represents the deformed band formed in the sample A2. It is clear that the microstructure of the band was the same with the base tempered martensitic structure. However, the color of the martensite laths in the deformed band was remarkably different from that of the matrix microstructure. This was probably due to the shear action causing a different orientation of the martensite laths in the band with respect to the base microstructure. **Figure 5** illustrates the band formation in the sample B5. It is apparent that both deformed and transformed bands appeared in this sample. The transformed bands formed as white lines and their microstructures were invisible with an optical microscopy analysis as opposed to deformed bands. A similar situation was also found in the sample group C (**Figure 6**). The thinning and
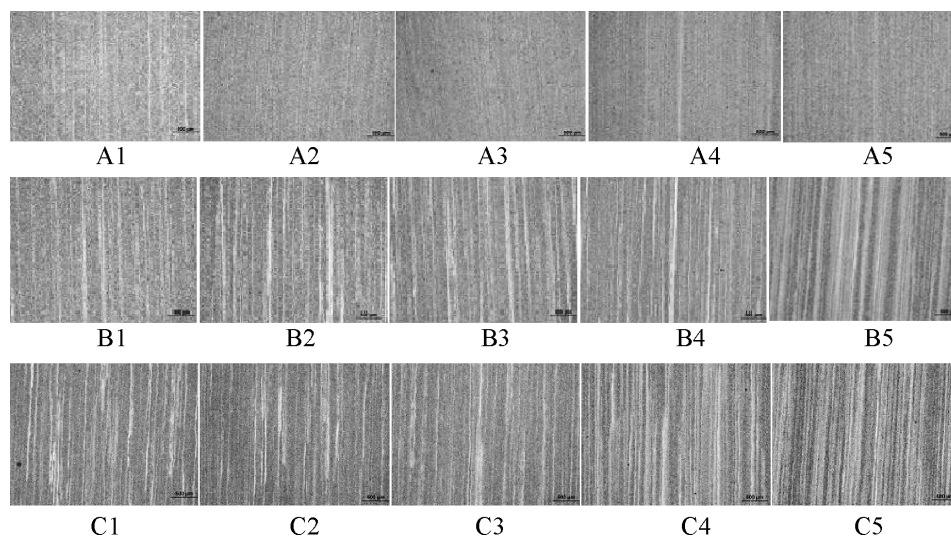

Figure 3: General view of ASBs in samples with various hardness and thickness
Slika 3: Splošen videz ASB v vzorcih z različno trdoto in debelino

Table 1: Shear band widths of the samples
Tabela 1: Širina pasov v vzorcih

Sample ID	Average Band Width (µm)	Band Type
A1	27	Deformed
A2	28	
A3	36	
A4	25	
A5	42	
B1	56	Deformed
B2	49	
B3	34	
B4	51	
B5	49	
B1	21	Transformed
B2	24	
B3	25	
B4	32	
B5	36	
C1	35	Deformed
C2	41	
C3	25	
C4	54	
C5	40	
C1	19	Transformed
C2	32	
C3	25	
C4	25	
C5	35	

Figure 5: View of deformed and transformed bands in the sample B5 after ballistic testing. Transformed band was observed as a white line.
Slika 5: Videz deformiranih in premenjenih pasov v vzorcu B5 po balističnem preizkusu. Premenjeni pas je viden kot bela črta

iron-carbide precipitates, consisting of a small amount of chromium, were observed (**Figure 7**). The size of precipitates changed between ≈100 nm and 5 µm. In addition, fine grains were also observed in the band. **Figure 8** shows the elemental analysis for the fine precipitate found in this band by EDX analysis. The formation of very fine grains and precipitates and very fine ferrite grains can be explained by the dynamic recrystallization. The impact velocity and kinetic energy of the projectile were sufficient to generate an immediate local heating through very narrow bands in the investigated steel AISI 4140. A ballistic study on the 30CrMnMo steel [10] also showed the formation of different types of shear bands. The fine-grain and

shortening of the martensite laths in a transformed band of C5 can be clearly seen in **Figure 6b**. Furthermore, white areas of this band were resolved by SEM analysis. **Figure 7** depicts the detailed microstructure features for this transformed band in the sample C5 steel after the ballistic impact. In white regions of the band, fine
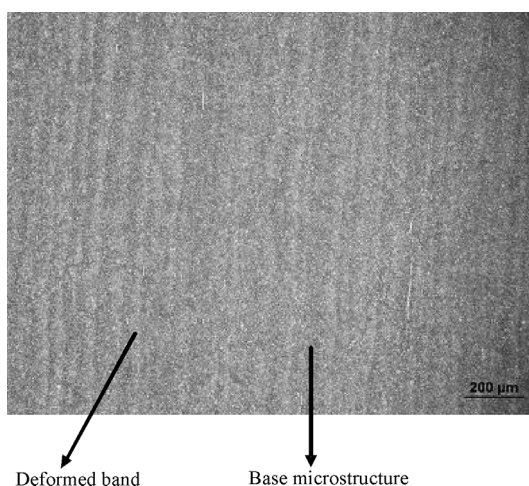

Figure 4: Microstructure of the sample A2 after ballistic testing. Deformed band formation with a lighter color compared to the base microstructure (tempered martensite) was observed.
Slika 4: Mikrostruktura vzorca A2 po balističnem preizkusu. Opaženo je formiranje deformacijskih pasov s svetlejšo barvo v primerjavi z osnovno mikrostrukturo (popuščeni martenzit)
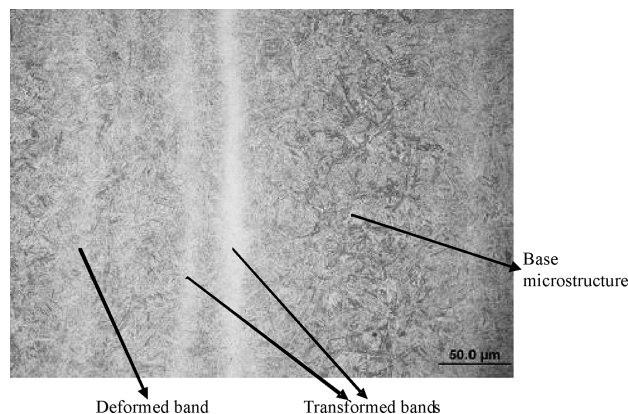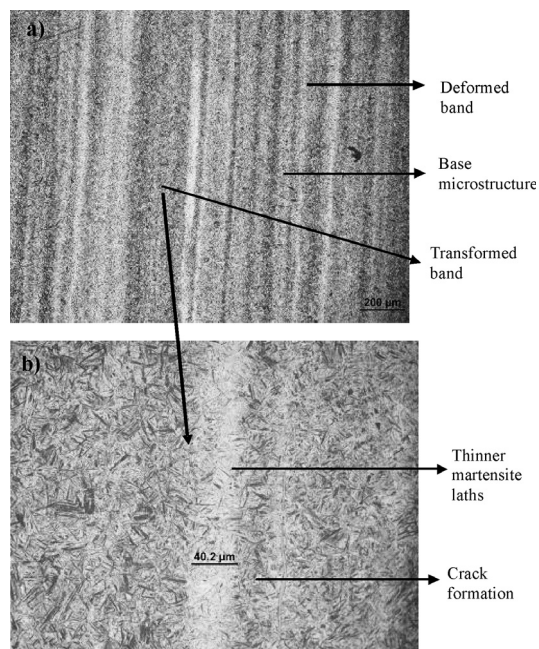

Figure 6: View of the band formation in the sample C5 after the impact of the 7.62-mm AP projectile. a) 100-times, b) 500-times.
Slika 6: Formiranje pasov v vzorcu C5 po trku AP-krogle 7,62 mm: povečave: a) 100-kratna, b) 500-kratna
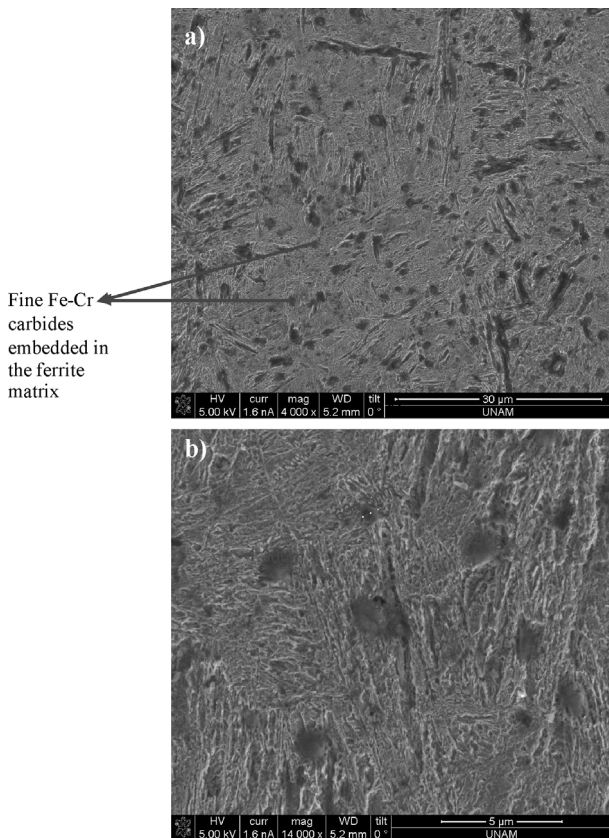
Figure 7: SEM examination of a transformed band formed in the sample C5. Formation of fine precipitate and grain occurred. a) 4000X, b) 14000X.
Slika 7: SEM-posnetki premenjenega pasa v vzorcu C5. Nastala so majhna zrna in izločki. Povečave: a) 4000-kratna, b) 14000-kratna

carbide-precipitate formations in the shear bands of the 30CrMnMo steel, observed after the impact of the tungsten-based projectile, were very similar to those found in this study.

The hardness of the bands varied with respect to the sample hardness and band type. **Table 2** gives the micro-hardness values of the bands for the investigated specimens. It is clear that the hardness of the ASBs was greater than that of the matrix for all the samples. The difference between the hardness levels of the matrix material and the ASB was smaller for the specimens of group A since the microstructural coherency and smaller
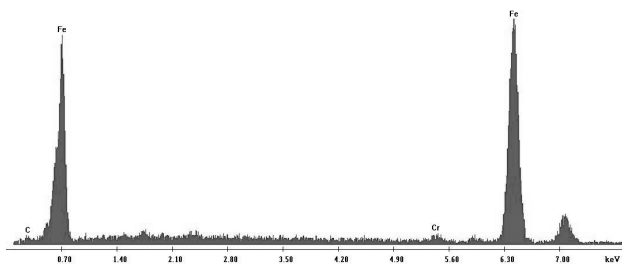

Figure 8: Elemental analysis of the fine precipitate found in the transformed band of C5 by EDX analysis.
Slika 8: Elementna EDX-analiza majhnega izločka v prememnjenen pasu vzorca (*c*/%)
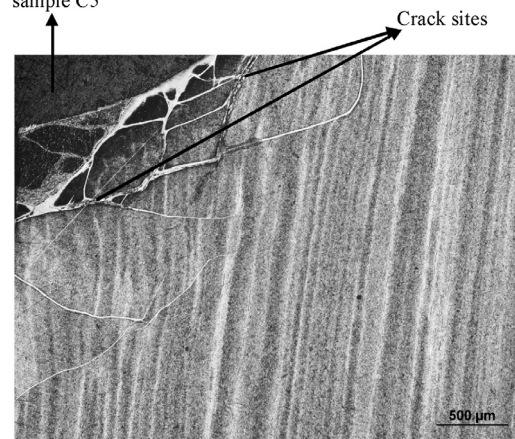

Figure 9: Micro-view of the sample C5 after the ballistic testing. The very intense ASB formation and the cracks are seen in the impact zone.
Slika 9: Mikrovidez vzorca C5 po balističnem preizkusu. V zoni udarca je nastalo veliko ASB-pasov in razpok.

Table 2: Shear bands hardness
Tabela 2: Trdota pasov

Sample Group	Types of Band	Hardness of Band (HV)	Hardness of Main Metal (HV)
A	Deformed	344	320
B	Deformed	519	417
	Transformed	569	
C	Deformed	695	667
	Transformed	722	

shear between the band and the matrix material took place. On the other hand, for the specimen groups of B and C the variation in the hardness was much higher due to the fact that the shear process occurred to a larger extent. The hardness of the deformed band (344 HV) was found to be slightly higher than that of the base material (320 HV) for the specimens of group A. However, it reached 519 HV and 695 HV for the sample groups B and C, respectively. On the other hand, the hardness of the transformed bands in the sample groups B and C was recorded as 569 HV and 722 HV, respectively. The increment in the hardness values was around 100 HV and 150 HV for the deformed and transformed bands in the sample group B, respectively. However, it was 30 HV and 50 HV for the deformed and transformed bands in the sample group C, respectively. The much higher hardness of transformed bands was directly caused by the fine structure of the grains and precipitates. A previous study [24] indicated that when the hardness of the AISI 4140 steel increased, the resistance to the advancement of the projectile decreased. Although the specimens belonging to the group A were perforated by a ductile hole formation mechanism under the impact of the 7.62-mm AP projectiles, most of the specimens in the groups of B and C were broken into several pieces in a brittle manner rather than perforated [24]. In other words, the projectile perforated the samples in group A easily due their lower hardness. Furthermore, the higher resistance to projectile movement in the sample groups B

and C led to higher local heating in the steel, which accelerated the formation of the ASBs. Both the microstructure and microhardness results for the AISI 4140 steel impacted by the AP projectile were found to be similar with those of AISI 4340 and DIN 100Cr6 [14] due to the fact that their alloy contents are similar. All the three steels have a strong carbide-former element of chromium, which promotes the formation of carbide precipitates in the transformed ASBs during the impact. In contrast to the other two steels, the AISI 4340 steel has another alloying element of nickel, which is not a carbide forming element and so it does not affect the precipitation sequence in the formation of the transformed bands.

Borvik et al. [26] worked on the adiabatic shear formation in the Weldox 460E Steel impacted by blunt projectiles. They found that the target thickness heavily influenced the shear localization process. Only the deformed bands ranging from 100 μm to 300 μm in width were observed in target plates with a thickness of less than 20 mm, while the transformed bands having much less width (10–100 μm) were found for the thicker target plates [26]. Furthermore, they measured much higher hardness values for the transformed bands (420 HV) compared to the original hardness of the steel (180-190 HV) [26]. In a more recent study [27], it was recorded that the impact of the 7.62-mm AP projectile to the dual-phase steel targets caused the formation of deformed bands with higher hardness values. An increase of 70 to 100 HV in the hardness of the samples was measured after testing due to the formation of these bands [27]. In the current study, it was also observed that an increase in the thickness of the samples caused more ASB formation. This is directly related to the increase in the resistance to projectile motion with increasing thickness. The higher portion of the kinetic energy of the projectile is transferred to the steel sample resulting in more ASB formation.

ASBs could also lead to crack formation. In other words, they can act as crack-initiation sites in the deformed materials under high strain rates. Typical crack sites occurred on the impact zone are represented for the sample C5 in **Figure 9**. Very intense ASBs led to the formation of cracks at the hit zone between the projectile and the sample. The crack formation in the sample was not detected outside the impact zone.

4 CONCLUSIONS

The main conclusions drawn from the experimental results can be described as follows:
- A deformed band formation was observed in all the steel specimens, which were tested with 7.62-mm AP projectiles. However, transformed bands occurred in the specimens having a hardness of 50 HRC or 60 HRC.
- The hardness of the bands was found to be remarkably higher than the matrix material.

- The impact action of the projectile led to the formation of fine grains and precipitates in the transformed bands.
- An increase in the resistance to the projectile motion increased the transformed band formation.
- The effect of the projectile hit on the microstructure of the AISI 4140 steel was found to be consistent with that of the AISI 4340 steel [14].

Acknowledgement

5 REFERENCES

[1] C. Zener C, J. H. Hollomon, Journal of Applied Physics, 15 (**1944**), 22
[2] R. Dormeval, The adiabatic shear phenomenon, pp. 47–69, in Materials at High Strain Rates, (Ed. T. Z. Blazynski), Elsevier Applied Science, 1987
[3] K. E. Aeberli, P. L. Pratt, J. Mater. Sci., 20 (**1985**), 316
[4] H. C. Rogers, Ann Rev Mater. Sci., 9 (**1979**), 283
[5] S. J. Manganello, K. H. Abbott, J. Mater., 7 (**1972**), 231
[6] J. L. Derep, Acta Metall. 35 (**1987**), 1245
[7] C. L. Wittman, M. A. Meyers, H.R. Park, Metall. Trans. A, 21 (**1990**), 707
[8] K. Cho, C. Y. Chi, J. Duffy, Metall Trans A, 21A (**1990**), 1161
[9] M. N. Bassim, J. Mater. Process. Technol., 119 (**2001**), 234
[10] Z. Q. Duan, S. X. Li, D. W. Huang, Fatigue Fract. Engng Mater. Struct., 26 (**2003**), 1119
[11] C-J. Hu, P-Y. Lee, J-S. Chen, J. of the Chinese Inst. of Engineers, 25 (**2002**) 1, 99
[12] A. G. Odeshi, M. N. Bassim, S. Al-Ameeri, Mater. Sci. Eng. A, 419 (**2006**), 69
[13] J. F. C. Lins, H. R. Z. Sandim, H-J. Kestenbach, D. Raabe, K. S. Vecchio, Mater. Sci. Eng. A, 457 (**2007**), 205
[14] M. Übeyli, T. Demir, R. O. Yıldırım, M. F. Aycan, Kovove Materialy-Metallic Materials, 47 (**2009**), 409–413
[15] J. A. Hines, K. S. Vecchio, ACTA Mater, 45 (**1997**), 635
[16] U. Andrade, K. Meyers, K. S. Vecchio, A. H. Chokshi, ACTA Mater., 42 (**1994**), 3183
[17] M. A. Meyers, U. R. Andrade, A. H. Chokshi, Metall. Mater. Trans., A21 (**1995**), 2881
[18] Y. B. Xu, W. L. Zhong, Y. J. Chen Q. Liu, Y. L. Bai, M. A. Meyers, Mater. Sci. Eng., A 299 (**2001**), 287
[19] M. A. Meyers, V. F. Nesterenko, J. C. Lasalvia, Y. B. Xu, Q. J. Xue, Phys. IV, 9 (**2000**), 51
[20] H. A. Grebe, H-R. Pak, M. A. Meyers, Metall Trans A, 16 (**1985**), 761
[21] F. D. S. Marquis, Y. J. Chen, J. Phys., IV C3 (**1997**), 441
[22] Y. J. Chen, M. A. Meyers, V. F. Nesterenko, Mater. Sci. Eng. A, 268 (**1999**), 70
[23] S. Nemat-Nasser, W. Guo, Mech. Mater., 32 (**2000**), 243
[24] T. Demir, M. Übeyli, R. O. Yildirim, Mater. Des., 29 (**2008**), 2009
[25] D. J. Viechnicki, M. J. Slavin, M. I. Kliman, Ceramic Bulletin, 70 (**1991**), 1035
[26] T. Borvik, J. R. Leinum, J. K. Solberg, O. S. Hopperstad, M. Langseth, Int. J. Impact Eng., 25 (**2001**), 553
[27] M. Übeyli, T. Demir, H. Deniz, R. O. Yildirim, Ö. Keleş, Mater. Sci. Eng., A 527 (**2010**), 2036

ACTIVATION OF POLYMER POLYETHYLENE TEREPHTHALATE (PET) BY EXPOSURE TO CO_2 AND O_2 PLASMA

AKTIVACIJA POLIMERA POLIETILENTEREFTALATA (PET) S CO_2- ALI O_2-PLAZMO

Alenka Vesel

Jožef Stefan Institute, Jamova 39, 1000 Ljubljana, Slovenia
Center of Excellence for Polymer Materials and Technologies, Tehnološki park 24, 1000 Ljubljana, Slovenia
alenka.vesel@guest.arnes.si

A comparison of O_2 and CO_2 plasma treatment for the functionalization of PET (polyethylene terephthalate) is presented. The plasma was created in a glass discharge chamber at a pressure of 75 Pa by an electrodeless RF discharge. The RF generator operated at a frequency of 27.12 MHz and a power of about 200 W. The samples were cut into small pieces and exposed to plasma for different periods. Immediately after the treatment the samples were characterized by high-resolution XPS. A comparison of both survey and high-resolution C1s peaks revealed that the amount of the specific functional groups formed on the surface during the plasma treatment was the same for the CO_2 and O_2 plasma. Within the limits of the experimental error the concentration of hydroxyl groups was about 34 % and carboxyl groups was about 29 % for a sample treated in both plasmas for 30 s. The results were explained by the rapid dissociation of both molecules to neutral oxygen atoms that are fairly stable in glass discharge tubes and readily react with the surface of polymer materials. Any effect of CO radicals is neglected since oxygen atoms are chemically more reactive, so possible differences in the surface functionalization might have been observed only for extremely short treatment times and/or orders of magnitude lower pressure.

Keywords: oxygen plasma, carbon dioxide plasma, PET polymer, surface functionalization, surface modification, XPS

Primerjali smo vpliv plazme, generirane v kisiku ali ogljikovem dioksidu, na funkcionalizacijo polimera PET (polietilen-tereftalat). Plazmo smo ustvarili v stekleni razelektritveni cevi z RF-generatorjem s frekvenco 27,12 MHz in močjo 200 W. Tlak plina v cevi je bil 75 Pa. Vzorce polimera smo različno dolgo izpostavili plazemski obdelavi, nato pa smo jih analizirali z visokoločljivostnim XPS-spektrometrom. Iz primerjave preglednih in visoko ločljivih XPS-spektrov smo ugotovili, da je delež novo nastalih funkcionalnih skupin enak za obe plazmi: O_2 in CO_2. V obeh primerih je bila koncentracija hidroksilnih skupin okoli 34-odstotna, koncentracija karboksilnih skupin pa okoli 29-odstotna. Podobnost obeh plazem smo razložili z močno disociacijo obeh molekul O_2 in CO_2 na nevtralne atome kisika, ki so v razelektritveni cevi dokaj stabilni in zaradi svoje reaktivnosti reagirajo s površino polimernega materiala. Vpliv radikala CO, ki nastaja pri disociaciji molekule CO_2 smo zanemarili, ker so kisikovi atomi veliko bolj reaktivni kot CO.

Ključne besede: kisikova plazma, plazma ogljikovega dioksida, polimer PET, funkcionalizacija površine, površinska modifikacija, XPS

1 INTRODUCTION

Low-pressure weakly ionized plasma is a popular tool for the modification of the surface properties of solid materials. It is often regarded as an ecologically benign alternative to wet chemical processing. The major effect of the plasma surface interaction is the potential interaction within the excited plasma particles and the atoms on the surface of the solid material. The result of the interaction is either a reduction or oxidation of the material surface.[1–12] Accordingly, plasmas created in different gases are used to obtain certain effects. For reduction proposes, a hydrogen plasma is often applied. The major technology based on the interaction of a hydrogen plasma with solid materials is discharge cleaning, i.e., the removal of oxidizing impurities from the surface of the materials.[1–5] A more modern technology based on the application of hydrogen plasma is the synthesis and/or modification of nanomaterials.[6–9]

Oxidation, on the other hand, is performed by a plasma created in various gases.[10–12] Oxygen, nitrogen, water vapour and carbon dioxide are gasses suitable for the generation of plasma with oxidizing particles. The technologies based on the application of oxidizing plasma include discharge cleaning (in this case degreasing),[13,14] plasma etching[15–17], plasma sterilization[18–19] and the plasma synthesis of metal oxide or nitride nanoparticles.[20–23] Another technology of particular importance is the surface activation of organic materials.[24–31] Generally speaking, any organic material can be functionalized by required functional groups using a plasma created in an appropriate gas. In practise, however, the type and concentration of specific functional groups created on a surface of specific organic material, is limited. In particular, the functionalization of polymer materials using oxygen plasma often leads to the appearance of at least three different functional groups (like hydroxyl, carbonyl and carboxyl). Although many attempts have been made to control the concentration of each functional group on the surface of organic materials, the results are far from being satisfactory. In

order to avoid the formation of all possible oxygen-rich functional groups on the surface of the polymer, the application of a plasma created in different gases was suggested. For instance, several attempts have been made to functionalize polymer PET (polyethylene terephthalate) with carboxylic groups using a plasma created in carbon dioxide instead of oxygen.[32,33] The aim of this paper is a comparison of the plasma created by the same discharge in the same plasma vessel but in two different gases: oxygen and carbon dioxide. The appearance of different functional groups was monitored by high-resolution XPS (X-ray photoelectron spectroscopy).

2 EXPERIMENTAL

2.1 Plasma treatment of polymer

Experiments were performed with a polyethylene terephthalate (PET) foil from DuPont. The samples were treated in the experimental system which was pumped with a two-stage oil rotary pump with a pumping speed of $4.4 \cdot 10^{-3}$ m^3 s^{-1}. The discharge chamber was a Pyrex cylinder with a length of 0.6 m and an inner diameter of 0.036 m. The plasma was created with an inductively coupled RF generator, operating at a frequency of 27.12 MHz and an output power of about 200 W. Commercially available oxygen or carbon dioxide was leaked into the discharge chamber. The pressure was measured by an absolute vacuum gauge. During our experiments, the pressure was fixed at 75 Pa. The samples of PET foil were treated in O_2 or CO_2 plasma for 10 s and 30 s.

2.2 X-ray photoelectron spectroscopy (XPS) characterization

The surface of the plasma-treated PET samples was analyzed with an XPS (X-ray Photoelectron Spectrometer) instrument TFA XPS Physical Electronics. The base pressure in the XPS analysis chamber was about $6 \cdot 10^{-8}$ Pa. The samples were excited with X-rays over a 400-μm spot area with a monochromatic Al $K_{\alpha1,2}$ radiation at 1486.6 eV. The photoelectrons were detected with a hemispherical analyzer positioned at an angle of 45° with respect to the normal to the sample surface. Survey-scan spectra were made at a pass energy of 187.85 eV and a 0.4-eV energy step, while for C1s individual high-resolution spectra were taken at a pass energy of 23.5 eV and a 0.1-eV energy step. Since the samples are insulators, we used an additional electron gun to allow for surface neutralization during the measurements. The spectra were fitted using MultiPak v7.3.1 software from Physical Electronics, which was supplied with the spectrometer. The curves were fitted with symmetrical Gauss-Lorentz functions. A Shirley-type background subtraction was used. Both the relative peak positions and the relative peak widths (FWHM) were fixed in the curve-fitting process.

3 RESULTS AND DISCUSSION

Samples were exposed to oxygen or carbon dioxide plasma for 10 s and 30 s. The time of 10 s is a typical treatment time that ensures the saturation of the surface with oxygen-rich functional groups. **Figure 1** represents the XPS survey spectra of an untreated sample and samples treated with O_2 and CO_2 plasma. We can observe qualitatively that the concentration of carbon is decreased in favor of oxygen for both plasma-treated samples. The quantitative results are summarized in **Table 1**. The experiments were repeated several times in order to minimize any statistical errors so the values presented in **Table 1** are averaged over several measurements. The statistical error is within 1 %, indicating fairly reproducible results. It is interesting that the concentration of carbon and oxygen is practically the same for samples treated with oxygen and carbon dioxide plasma. Furthermore, the differences between the 10 s and 30 s treatment times are minimal. This is just another confirmation of the well-known fact that saturation of the surface with functional groups occurs before 10 s of treatment time.[34,35]

Table 1: Comparison of the surface composition of the PET polymer treated in oxygen or carbon dioxide plasma.
Tabela 1: Primerjava površinske sestave polimera PET, obdelanega v kisikovi plazmi ali plazmi ogljikovega dioksida

Sample	C	O
untreated sample	73.1	26.9
CO_2 plasma – 10 s	55.9	44.1
O_2 plasma – 10 s	56.5	43.5
CO_2 plasma – 30 s	55.9	44.2
O_2 plasma – 30 s	56.9	43.2

The survey spectra presented in **Figure 1** give us information about the concentration of elements in the
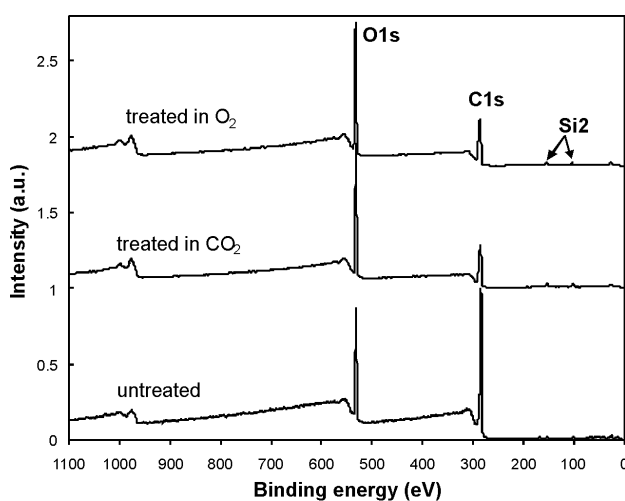

Figure 1: Comparison of XPS survey spectra of untreated PET sample and of PET sample treated in O_2 or CO_2 plasma for 10 s
Slika 1: Primerjava preglednega XPS-spektra neobdelanega vzorca polimera PET ter vzorca polimera PET, obdelanega 10 s v O_2- ali CO_2-plazmi
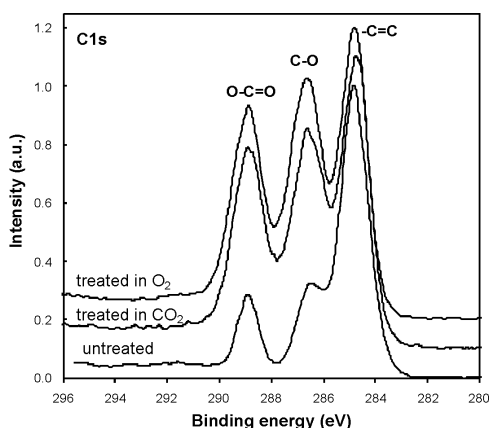
Figure 2: Comparison of high-resolution XPS spectra of carbon C1s of untreated PET sample and of PET sample treated in O_2 or CO_2 plasma for 10 s

Slika 2: Primerjava visoko ločljivega XPS-spektra ogljika C1s neobdelanega vzorca polimera PET ter vzorca polimera PET, obdelanega 10 s v O_2- ali CO_2-plazmi

Table 2: Comparison of the concentration of different functional groups formed on PET polymer during treatment in oxygen or carbon dioxide plasma.

Tabela 2: Primerjava koncentracije različnih funkcionalnih skupin, nastalih na površini polimera PET med obdelavo v kisikovi plazmi in plazmi ogljikovega dioksida

Sample	-C=C	C-O	O=C-O
untreated sample	75.8	13.0	11.2
CO_2 plasma – 10 s	42.4	32.3	25.3
O_2 plasma – 10 s	42.2	31.7	26.1
CO_2 plasma – 30 s	38.7	33.1	28.3
O_2 plasma – 30 s	36.5	34.3	29.2

surface film but do not tell us anything about the concentration and the type of each particular functional group. In order to get an insight into the concentration of the functional groups, we performed high-resolution XPS measurements of the carbon C1s peak. Again, we performed the analysis on several samples, but a typical result is presented in **Figure 2**. The major peak at 285 eV corresponds to the –C=C bond, the peak at 286.3 eV to the C-O(H) bond, while the well-pronounced peak at 288.8 eV corresponds to –COO- (carboxyl and ester group). As expected, from the knowledge gained from **Figure 1** and **Table 1**, the concentration of hydroxyl C-OH and carboxyl functional groups -COOH is increased dramatically. Interesting, however, no difference is observed between the sample treated in O_2 and CO_2 plasma. **Table 2** represents a quantification of the results presented in **Figure 2**. Again, the values presented in **Table 2** are averaged over several samples. It is interesting that the concentration of different functional groups on all the samples is practically the same, or definitely within the limit of the experimental error. From these results we can conclude that both O_2 and CO_2 plasma treatments lead to the formation of practically the same functional groups.

The upper result is explained by taking into account the characteristics of the oxygen and carbon dioxide plasmas. Since the ionization fraction in both plasmas is practically the same, and is of the order 10^{-6}, the charged particles play a minor role in the surface modification of our sample. The dissociation fraction, on the other hand, is at least five orders of magnitude larger than the ionization fraction. Such a huge difference between the ionization and dissociation fraction is explained by the probabilities of neutralization and recombination. The probability for the surface neutralization of charged particles does not depend on the type of the material facing plasma and is very close to 1. The surface recombination probability, on the other hand, is very sensitive to the surface properties and may be anything between 10^{-6} and 1.[36-37] In the case of glass discharge chambers, the probability for surface recombination is fairly low, since oxygen atoms do not chemisorb on the glass surface. In both cases, the result of the dissociation is atomic oxygen. Since the dissociation energies for oxygen molecules and CO_2 molecules are similar, it is expected that the dissociation probability would be practically the same in both plasma. Moreover, the surface recombination probabilities are also similar for both gases. Taking into account these considerations we can explain the observed functionalization of the polymer. In both O_2 and CO_2 plasmas the major reactants are neutral oxygen atoms. There is no reason that the atoms originating from oxygen molecules or carbon dioxide molecules would act differently. Any differences might have appeared at much lower treatment times, i.e., well before the saturation of the surface with functional groups is observed. Such experiments, however, are not possible in our labs since we do not have a pulsed plasma generator.

4 CONCLUSION

Well-defined foils of polymer PET were exposed to plasma created in oxygen and carbon dioxide gases in order to study any possible differences in the surface functional groups created during plasma processing. High-resolution XPS was applied to study the type and concentration of different functional groups. Within the limits of the experimental error, we can clearly conclude that there are no differences in the oxygen functional groups between the treatment with oxygen and the carbon dioxide plasmas. Our results were explained by the formation of a large density of neutral oxygen atoms in both plasmas, since these atoms are the major reactance in low-pressure, weakly ionized, highly reactive plasma.

ACKNOWLEDGEMENT

5 REFERENCES

[1] A. Vesel, A. Drenik, R. Zaplotnik, M. Balat-Pichelin, Surf. Interface Anal., 42 (**2010**) 6/7, 1168–1171

[2] M. Mozetic, A. Zalar, M. Drobnic, Thin solid films, 343–344 (**1999**), 101–104

[3] M. Mozetic, Vacuum, 61 (**2001**) 2/4, 367–371

[4] M. Mozetic, B. Pracek, Inf. Midem, 28 (**1998**) 3, 171–174

[5] F. Brecelj, M. Mozetic, Vacuum, 40 (**1990**) 1/2, 177–178

[6] A. Hassanien, M. Tokumoto, P. Umek, D. Vrbanic, M. Mozetic, D. Mihailovic, P. Venturini, S. Pejovnik, Nanotechnology, 16 (**2005**) 2, 278–281

[7] M. K. Sunkara, S. Sharma, R. Miranda, G. Lian, E. C. Dickey, Appl. Phys. Lett., 79 (**2001**) 10, 1546–1548

[8] M. Wolter, I. Levchenko, H. Kersten, K. Ostrikov, Appl. Phys. Lett., 96 (**2010**) 13, 133105

[9] I. Levchenko, S. Y. Huang, K. Ostrikov, S. Xu, Nanotechnology, 21 (**2010**) 2, 025605

[10] A. Vesel, M. Mozetic, A. Zalar, Appl. Surf. Sci., 200 (**2002**) 1/4, 94–103

[11] A. Vesel, M. Mozetic, A. Drenik, N. Hauptman, M. Balat-Pichelin, Appl. Surf. Sci., 255 (**2008**) 5, 1759–1765

[12] A. Vesel, A. Drenik, M. Mozetic, A. Zalar, M. Balat - Pichelin, M. Bele, Vacuum, 82 (**2007**) 2, 228–231

[13] A. Vesel, M. Mozetic, A. Drenik, S. Milosevic, N. Krstulovic, M. Balat-Pichelin, I. Poberaj, D. Babic, Plasma Chem. Plasma Process., 26 (**2006**) 6, 577–584

[14] M. Mozetic, A. Zalar, Vacuum, 71 (**2003**) 1/2, 233–236

[15] A. Vesel, M. Mozetic, P. Panjan, N. Hauptman, M. Klanjsek - Gunde, M. Balat - Pichelin, Surf. Coat. Technol., 204 (**2010**) 9/10, 1503–1508

[16] A. Drenik, A. Vesel, M. Mozetic, J. Nucl. Mater., 386–388 (**2009**), 893–895

[17] M. Kunaver, M. Mozetic, M. Klanjsek - Gunde, Thin solid films, 459 (**2004**) 1/2, 115–117

[18] K. Eleršič, I. Junkar, A. Špes, N. Hauptman, M. Klanjšek - Gunde, A. Vesel, Mater. Tehnol., 44 (**2010**) 3, 153–156

[19] D. Vujošević, Z. Vratnica, A. Vesel, U. Cvelbar, M. Mozetič, A. Drenik, T. Mozetič, M. Klanjšek - Gunde, N. Hauptman, Mater. Tehnol., 40 (**2006**) 6, 227–232

[20] Z. Chen, U. Cvelbar, M. Mozetic, J. He, M. K. Sunkara, Chem. Mater., 20 (**2008**) 9, 3224–3228

[21] K. Ostrikov, Plasma Nanoscience, Wiley, New York, 2008

[22] A. Drenik, U. Cvelbar, K. Ostrikov, M. Mozetic, J. Phys. D: Appl. Phys., 41 (**2008**) 11, 115201-1-115201-7

[23] U. Cvelbar, K. Ostrikov, M. Mozetic, Nanotechnology, 19 (**2008**) 40, 405605-1–405605-7

[24] U. Cvelbar, M. Mozetic, I. Junkar, A. Vesel, J. Kovac, A. Drenik, T. Vrlinic, N. Hauptman, M. Klanjsek-Gunde, B. Markoli, N. Krstulovic, S. Milosevic, F. Gaboriau, T. Belmonte, Appl. Surf. Sci., 253 (**2007**) 21, 8669–8673

[25] A. Vesel, M. Mozetic, A. Hladnik, J. Dolenc, J. Zule, S. Milosevic, N. Krstulovic, M. Klanjsek-Gunde, N. Hauptman, J. Phys. D: Appl. Phys., 40 (**2007**) 12, 3689–3696

[26] A. Vesel, M. Mozetic, A. Zalar, Surf. Interface Anal., 40 (**2008**) 3–4, 661–663

[27] A. Vesel, M. Mozetic, A. Zalar, Vacuum, 82 (**2008**) 2, 248–251

[28] M. Sowe, I. Novak, A. Vesel, I. Junkar, M. Lehocky, P. Saha, I. Chodak, Int. J. Polym. Anal. Ch., 14 (**2009**) 7, 641–651

[29] A. Vesel, M. Mozetic, S. Strnad, K. Stana-Kleinschek, N. Hauptman, Z. Persin, Vacuum, 84 (**2010**) 1, 79–82

[30] A. Asadinezhad, I. Novak, M. Lehocky, F. Bilek, A. Vesel, I. Junkar, P. Saha, A. Popelka, Molecules, 15 (**2010**) 2, 1007–1027

[31] A. Vesel, K. Elersic, I. Junkar, B. Malic, Mater. Tehnol., 43 (**2009**) 6, 323–326

[32] N. Medard, J.-C. Soutif, F. Poncin-Epaillard, Surf. Coat. Technol., 160 (**2002**) 2/3, 197–205

[33] Meng-Jiy Wang, You-Im Chang, F. Poncin-Epaillard, Surf. Interface Anal., 37 (**2005**) 3, 348–355

[34] A. Vesel, I. Junkar, U. Cvelbar, J. Kovac, M. Mozetic, Surf. Interface Anal., 40 (**2008**) 11, 1444–1453

[35] I. Junkar, U. Cvelbar, A. Vesel, N. Hauptman, M. Mozetic, Plasma Processes Polym., 6 (**2009**) 10, 667–675

[36] A. Drenik, U. Cvelbar, A. Vesel, M. Mozetic, Inf. Midem, 35 (**2005**) 2, 85–91

[37] A. Drenik, U. Cvelbar, A. Vesel, M. Mozetic, Strojarstvo, 48 (**2006**) 1/2, 17–22

THE IMPACT ON RIGID PVC PIPES: A STUDY OF THE CORRELATION BETWEEN THE LENGTH OF THE CRAZED ZONE AND THE AREA OF THE IMPACTED REGION

UDAR TOGIH PVC-CEVI: ŠTUDIJA KORELACIJE MED DOLŽINO RAZPOKANE ZONE IN POVRŠINO ZONE UDARA

Christian Bopda Fokam[1], Mohamed Chergui[1], Kalifa Mansouri[2], Mohamed El Ghorba[1], Mohamed Mazouzi[1]

[1]Laboratoire de Contrôle et de Caractérisation des Matériaux, B.P 8118, Oasis-Route El Jadida – ENSEM / Casablanca, Maroc
[2]Ecole Normale Supérieure de l'Enseignement Technique, Bd hassan II, Mohamedia Maroc
fokam79@yahoo.fr

This paper presents a numerical methodology aimed at identifying quantitatively the crazing under quasi-static impact loading of rigid PVC pipes. It also presents the correlation between the length of the crazed region and the area of the impact. Testing low-speed impacts has provided a damaging loading before the rupture of the sample's pipe section. The striker impact on the pipes allows us to appreciate the damage caused. The craze in the impacted area was identified in our previous work [1], the different criteria of the craze initiation are presented. The criterion of Steinstern and Myers, better adapted to rigid PVC [2], is used in a numerical simulation on ANSYS for the problems of static contact. For tests carried out at low velocity, an equivalent static load representing the dynamic impact loading can account for the stress states in the structure of the pipe [3]. The analysis of the stress fields in the structure of the pipe compared to the stress of the craze initiation depends on the first stress invariant and allows us to deduce the length of the crazed region in the thickness of the pipe. Finally, we present the correlation between the length of the crazed region and the area of the zone of impact (the area of the imprint of the striker on the pipe).

Keywords: damage, crazing, impact, PVC, amorphous polymer

Predstavljena sta numerična metodologija za kvantitativno identifikacijo razpokanja pri kvazi statični udarni obremenitvi togih PVC-cevi in korelacija med dolžino *z* razpokane zone in površino udara. Preizkusni udari z majhno hitrostjo so ustvarili poškodbeno obremenitev pred zlomom prereza cevi. Udarec cevi s kladivom omogoča, da se oceni nastala poškodba. Razpokanje zone udara je identificirano v našem prejšnjem delu [1], zato so predstavljena merila začetka razpokanja. Merilo Steinsteina in Myersa, ki je bolj prilagojen za toge PVC-cevi [2], je uporabljen pri numerični simulaciji ANSYS za problem statičnega stika. Za preizkuse pri majhni hitrosti lahko ekvivalentna statična obremenitev pomeni dinamično obremenitev in omogoči, da se opredeli napetostno stanje v strukturi cevi [3]. Analiza napetostnih polj v strukturi cevi, primerjana z napetostjo začetka razpokanja, je odvisna od invariante prve napetosti in mogoča, da se določi globina dolžine zone razpoke v steni cevi. Končno je predstavljena tudi korelacija med dolžino razpokane zone in površino zone udara (površina odtisa kladiva).

Ključne besede: poškodbe, razpokanje, udar, PVC, amorfni polimer

1 INTRODUCTION

Plastic materials are a large proportion of pipe water-supply systems primarily due to the ease of installation and the relatively low cost of the materials. Plastic pipes used for water canalization continues to be the subject of many studies focusing mainly on the behavioral nature of the material. During construction works, pipes are often subjected to accidental impact such as falling rocks, scratches etc. The ability to resist pressure and the reliability becomes important to engineers. The approach generally used to solve this problem requires the identification and determination of the length of the morphological degradation mechanism of the material during impact.

Amongst the morphological mechanisms identified as responsible for the degradation of amorphous polymers, we find mostly crazes and shear bands [4].

The identification of a craze in the area of the impact has already been demonstrated in a previous study [1]. It is important to define the critical length of the crazed region, beyond which the material can be considered as either obsolete or unusable.

This article focuses mainly on the presentation of a numerical methodology for the determination of the length of a crazed area. A correlation between the area of the impact on the pipe (imprint) and the length of the crazed region is also studied. To illustrate this study, we first define a craze and the different initiation criteria. Subsequently, the material and the dimensions of the test specimens are presented, as well as the experimental impact conditions. Finally, steps in the numerical methodology and the analyses for the determination of the length of the crazed region are exposed.

2 CRAZING

2.1 Presentation

Crazing is a defect resulting in the appearance of cracks on the surface of a material. Crazes are superficially similar to cracking.
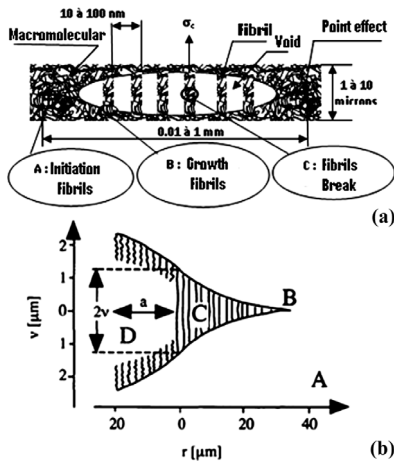
Figure 1: (a) Diagram of a craze with cracks characterized by the presence of fibrils [6] (b) Craze region with the result of fissure formation [7]. Zone A represents the region were the glassy polymer is elastically deformed. B, the area were initiation crazing occurs. C propagation or growth of the crazed region. D Rupture of the fibrils leading to the transformation of the craze into a crack of length a.

Slika 1: (a) Diagram poškovanja, ki ga karakterizirajo fibrili [6]. (b) Zona risov z rezultati nastanka razpok [7]. Zona A je področje, kjer je bil steklast polimer elastično deformiran. B je površina nastanka risov. D je prelom fibrilov, ki rise spremeni v razpoko z dolžino a.

However, there are differences between them. Crazes are characterized by crack partitions linked together by small parallel fibrils of the material [5] (see **Figure 1a**).

Crazes and cracks proceed in three stages. Initiation, which is the enlargement and rupture of fibrils. Crazing involves a process of stretching the bulk of the material towards the area were the fibrils are located at the beginning of the crack [8].

2.2 Criteria of craze initiation

In elastic and visco-elastic regimes or after the development of a significant plastic deformation, the corresponding formula of the initiation criteria is distinct for each regime. In a previous publication [1], we detected the first craze in elasto/visco-elastic regime for rigid PVC. The initiation criteria presented below, correspond to the craze appearances in elasto/visco-elasto regimes and elaborate on different phenomenological bases.

Following the observation of an incubation time for the craze formation where the constant stress is less than half of the yield stress (σ_y), Argon et al. [9] proposed a sophisticated formula (1), as shown below

$$\left| \sigma_1 - \sigma_2 \right| = \frac{A}{C + 3I_1 / 2\sigma_y Q} \tag{1}$$

where A and C represent material parameters. σ_1 and σ_2, respectively, are the maximum and minimum principal stress. I_1 is the first stress invariant, $Q = 0.0133$ is a factor controlling the dependency of the criterion to the shear stress on I_1 and σ_y is the yield stress.

Sternstein and Myers [10] proposed a criterion based on the mechanism of micro-void formation in a dilatational

stress field, and on the stabilization of micro voids through a deviatoric stress (2). Recently, following the same approach, Gearing [11] proposed a criterion based only on the maximum principal stress (3):

$$\left| \sigma_1 - \sigma_2 \right| \geq A^0 + \frac{B^0}{I_1} \tag{2}$$

$$\sigma_1 \geq A + \frac{B}{I_1} \tag{3}$$

With the same idea, Oxborough and Bowden suggested the definition of a criterion based on critical deformation. The criterion has been reformulated in the stress for an elastic material, with ν standing for the Poisson's ratio and E for the Young's modulus ($X' = EX$ and $Y' = EY$ are two material parameters depending on the temperature) (4):

$$\sigma_1 - \nu\sigma_2 - \nu\sigma_3 \geq X' + \frac{Y'}{I_1} \tag{4}$$

To account for the sensitivity to hydrostatic pressure observed for some polymers, Ishikawa [12] proposed the following criterion (5):

$$I_1 \geq A + \frac{B}{I_1} \tag{5}$$

3 EXPERIMENTAL PROGRAM

3.1 Material

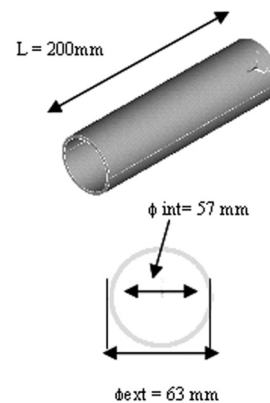The pipes used are mostly made up of polyvinyl chloride (rigid PVC). They come from the same

Figure 2: Dimensions (in millimeter) of samples of the test tube for the impact test

Slika 2: Dimenzije vzorcev (v milimetrih) preizkusne cevi za udarne preizkuse

Table 1: Mechanical properties of rigid PVC
Tabela 1: Mehanske lastnosti togega PVC

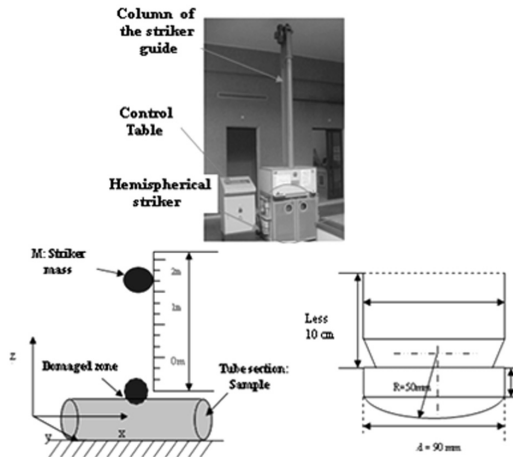| Properties	Values
Young's modulus	3200 MPa
Tensile stress fracture	75 MPa
Elongation at fracture tensile	100 %
Tensile strength in compression	50–75 MPa

Figure 3: (a) Impact machine from the German TestSystems UTS, (b) synoptic diagram of the impact machine, (c) dimensions of the hemispherical striker
Slika 3: (a) Udarna naprava nemškega proizvajalca TestSystems UTS, (b) sinoptičen diagram udarne naprave, (c) dimenzije hemisferičnega kladiva

molding. The pipe dimensions are 63 mm in diameter and a wall with a 4.5 mm thickness (see **Figure 2**).

3.2 Presentation of the impact machine

This device allows us to drop a weight (striker) from a selected height onto a pipe (see **Figure 3a and 3b**). The section of the pipe is placed on a support "*V*". A cylindrical rigid bar to help prevent the rebound of the striker during and after the impact is introduced. A weight of the striker equal to 16 kg and of radius $R = 50$ mm is used. (See **Figure 3c**). The height used ranges between 0 m and 2 m. The mass, height and velocity are used to calculate the kinetic energy of the impact.

After impact, the object dropped of mass 16 kg, leaves an elliptical mark called the impacted area or the area of impact at the point of impact (see **Figure 4**).

4 METHODOLOGY FOR DETERMINING THE LENGTH OF THE CRAZED REGION

In a previous publication [1] we have identified the crazing as the morphological mechanism of damage in the impacted area (see **Figure 4**). In this section, we propose a numerical methodology for determining the length of the crazed region in the pipe wall thickness below the impacted area (see **Figure 4**).
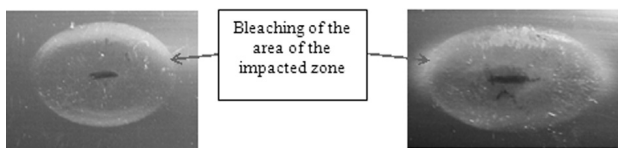

Figure 4: Photographs of the impacted area on sections of the pipe at varying heights after the drop of the striker (mass)
Slika 4: Posnetka površine udara na prerezih cevi po različni višini padca udarnega kladiva

The craze initiating to the critical stress (in agreement with the criterion of craze initiation considered) and the methodology consist of delimiting areas in the pipe were the stress levels are greater than the critical stress ($\sigma \geq \sigma_{cr}^{am}$, σ_{cr}^{am}: critical stress initiation).

The different criteria for the craze initiation presented above (Section 1.2) are valid, depending on the type of material. An analysis of these criteria showed that the criterion of Sternstein and Myers (2) is the best adapted for rigid PVC.

The determination the length of the crazed region requires the calculation of stress fields in the wall thickness of the pipe material at the time of impact. These experiments are difficult. We have constructed a numerical model based on Ansys for the simulation of the problem of impact dynamics [13]. As our test impacts are at low velocities ($V < 6$ m/s), it is shown in the literature that a static equivalence of a dynamic problem is sufficient to account for the stress in the structure [3]. Therefore, the impact of the striker on the pipe is treated as a static contact problem between two solid bodies. The normal load applied on the upper surface of the striker (see **Figure 5**) is obtained through the equations of Hertz, linking the dimensions of the impacted area (see **Figure 4**) to the static normal force. A visco-elastic constitutive law is applied to the numerical model in order to reduce the computation times of the problem, which is already highly non-linear, without altering the objectives of the study. Indeed, the craze initiating for the case of rigid PVC in the elastic regime and the critical stress initiation are expected to lower the yield stress.

The high stress levels in the material (stress greater than the resistance of the material studied) do not affect the final results of the experiment.
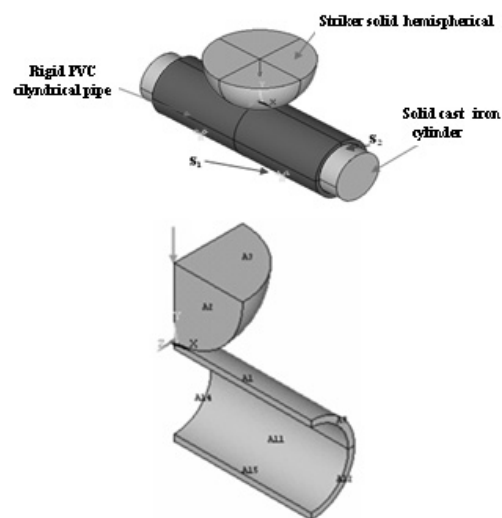

Figure 5: Geometric representation of the numerical model: (a) full actual geometry, (b) ¼ of the geometry implemented due to the symmetry of the problem.
Slika 5: Geometrična slika numeričnega modela: (a) polna realna geometrija, (b) ¼ geometrije, uporabljene zaradi simetrije problema

The tests impacts, being numerous, means that the details of the methodology for determining the length of the crazed region in the pipe wall thickness will be presented for an impact using a striker of mass 16 kg dropped from a height of 1.25 m (designated impact: 1.25 m/16 kg).

$\sigma_{S\&M}$, the stress parameter of the pipe to be found, corresponds to the criterion of Sternstein and Myers (2):

$$\sigma_{S\&M} = \left| \sigma_1 - \sigma_2 \right| \geq \sigma_{cr}^{am} = A^0 + \frac{B^0}{I_1} \qquad (6)$$

where $\sigma_1 > \sigma_2 > \sigma_3$, $A^0 = 19.936$ MPa and $B^0 = 1\ 203.384$ MPa 2 for rigid PVC.

Figure 7, represents a cartograph stress state in the wall thickness of the pipe. Around each isovalue of a contour line with the stress represented by we observe that from the given equation above, the critical stress of Sternstein and Myers (σ_{cr}^{am}, see formula (6)) varies weakly with I_1 (see **Figure 6**). Moreover, it seems reasonable that the local critical stress for the craze initiation decreases as I_1 increases. Thus, the creation of micro-voids before crazing would be easier and would lead to a lower stress initiation. This reflects in a decrease in the critical stress while "I_1" increases.

In **Figure 6** we see that the variation of is not very significant and in all cases it does not fluctuate above and below 10 % of its average value. Thus, the critical stress σ_{cr}^{am} at all points on an isovalue contour of the stress '$\sigma_{S\&M}$' is considered constant.

Each isovalue contour of the stress in **Figure 7b** is a possible limit between the crazed regions and others not crazed in the thickness of the pipe. This limit is identified when. We also notice that all the isovalue contours cover the entire section of the thickness of the pipe (see **Figure 7b**). Thus, whatever the limit of the isovalue contour, crazing occupies the entire thickness of the pipe, where the stress fields represent (with being constant on an isovalue contour).
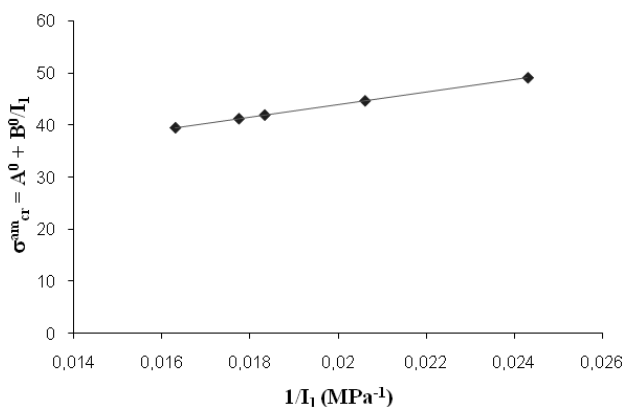

Figure 7: Cartograph of stress states $\sigma_{S\&M} = \left| \sigma_1 - \sigma_2 \right|$ corresponding to the criterion of Sternstein and Myers. (**a**) ¼ of the geometry of the pipe, (**b**) surface S1 of the thickness of the pipe
Slika 7: Kartografija napetostnega stanja $\sigma_{S\&M} = \left| \sigma_1 - \sigma_2 \right|$

Considering as a constant on an isovalue contour, the representation of the stress states compared to critical stress initiation along an imaginary line (see **Figure 7b**) is sufficient to determine the length of the crazed region, which corresponds to .

Figure 8, represents the stress states compared to along an imaginary line located at any position, crossing the right section of the structure of the pipe (S_1) just below the contact point (see **Figure 7**).

In **Figure 8**, the intersection between the plot and indicates the limit of the crazed region. Beyond this intersection, the stress is less than the stress initiation. The stress state is abnormally large and the structure can be attributed to the elastic constitutive law applied to the numerical model. Nevertheless, the intersection point is

Figure 6: A graph of the critical stress of the craze initiation of the Sternstein and Myers criterion $\sigma_{cr}^{am} = A^0 + B^0/I_1$ around an isovalue contour in the thickness of the pipe.
Slika 6: Graf kritične napetosti začetka poškodbe po Sternstein-Myersovem merilu $\sigma_{cr}^{am} = A^0 + B^0/I_1$ za enake vrednosti po obodu cevi
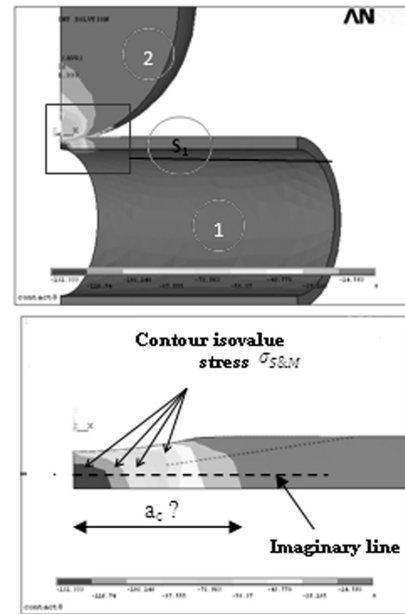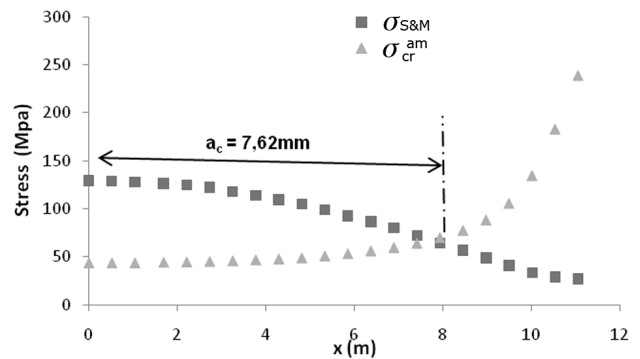

Figure 8: A Graph of the critical stress for craze initiation against the stress state of the material subjected to loading, along an imaginary line selected in the pipe.
Slika 8: Grafikon kritične napetosti za nastanek poškodbe σ_{cr}^{am} proti napetosti $\sigma_{S\&M}$ za obremenjeni material po imaginarni črti v cevi.
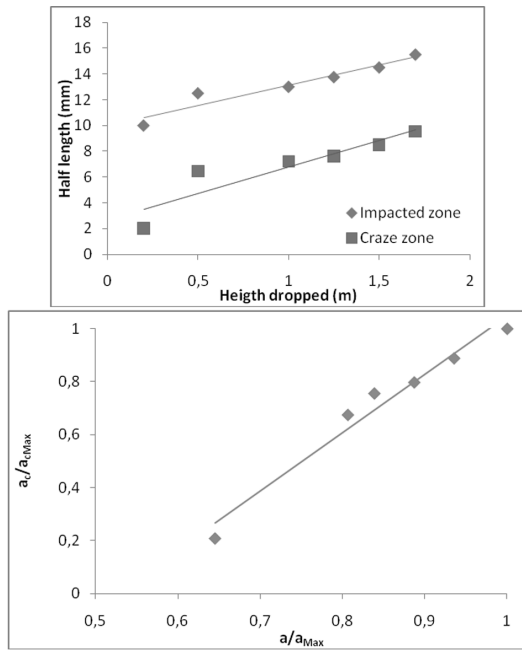
Figure 9: (a) Evolution comparison of crazed region "a_c" and impacted area "a" depending on the level of impact. (b) Evolution of the corresponding non-dimensional "a_c/a_{cMax}" by to "a/a_{max}"

Slika 9: (a) Evolucija primerjanega poškodovanega področja "a_c" in področja udara v odvisnosti od velikosti udara; (b) ustrezne brezdimenzijske vrednosti "a_c/a_{cmax}" in "a/a_{max}"

where the stress 51 MPa $\leq \sigma_y$ = 52 MPa (σ_y: yield strength in tensile of the rigid PVC).

In **Figure 8**, the half-length "a_c" of the crazed region, of the stress state corresponding to the test impact using, respectively, a height and mass of 1.25 m and 16kg is: **7.62 mm** ($a_c = L_c / 2$: half the length of the crazed zone).

Table 2 summarizes the determined size of the half lengths of the crazed regions corresponding to the different impact tests performed ($h \in [0.2 \text{ m } 1.7 \text{ m}]$).

Table 2: Half-length of the crazed region "a_c" corresponding to the impacts of mass 16kg dropped from different heights
Tabela 2: Polovica dolžine poškodovane zone "a_c", ki ustreza udaru mase 16 kg spuščene z različne višine

Designation (m/kg)	h	a/mm	a_c/mm
0.2 m/16 kg	0.2	10	2
0.5 m/16 kg	0.5	12.5	6.45
1 m/16 kg	1	13	7.22
1.25 m/16 kg	1.25	13.75	7.62
1.5 m/16 kg	1.5	14.5	8.49
1.7 m/16 kg	1.7	a_{Max} = 15.5	a_{cMax} = 9.55

From **Table 2**, we notice that the dimensions of the various areas of impact "a" are higher than the corresponding crazed "a_c". It is true that bleaching the impacted area (see **Figure 4a**) allows the localization of the morphological degrading mechanisms (damage caused by the impact).However, it does not help to

determine its length. But the developments of these two parameters show correlations (see **Figure 9**).

In the range of the impact tests performed ($h \in [0.2$ m, 1.7 m]), the evolutions of "a_c" and "a" show an almost linear growth with the level of impact (see **Figure 9a**). In **Figure 9b**, the correlative evolution shows a linear dependence of these two quantities. The area of the imprint (impacted area) may be a good indicator of the length of the crazed region in a pipe subjected to an impact.

5 CONCLUSION

A numerical methodology for determining the length of the crazed region in a rigid PVC pipe subjected to a quasi-static impact has been presented.

With crazing identified on the impacted area [1], determining its length with the methodology proposed involves a comparison of the stress states in the structure for the critical stress of the craze initiation. After choosing the criterion of initiation of Sternstein and Myers (6) for rigid PVC [2] we notice that its dependence on the first stress invariant I_1 induces some distinct critical values. However, on an isovalue contour of stress, the criterion does not deviate more than ±10 % from the average value (see **Figure 6**). From this small variation we considered the value of the critical initiation as a constant on an isovalue contour. Thus, the comparative representation of the stress in the wall thickness of the pipe $\sigma_{S\&M}$ and the critical stress initiation craze σ_{cr}^{am} (see **Figure 8**) along a line crossing all the boundaries of all the isovalue contours (see **Figure 7b**) allow us to deduce the length of the crazed region corresponding to $\sigma_{S\&M} \geq \sigma_{cr}^{am}$. Depending on the level of the impact load, we see a linear growth of the length of the crazed region (see **Figure 9a**), which is linearly correlated to the size of the corresponding impacted area (see **Figure 9b**).

6 REFERENCES

[1] Fokam Bopda C., Chergui M., Ghorba M., K. Mansouri Impact des tubes en PVC rigide : tenu mécanique et mécanisme de détérioration, Communication, Congrès Français de Mécanique (Marseille), ref: N°1313- S18 /CFM'2009 (2009)

[2] Fokam Bopda C., Chergui M., Ghorba M., K. Mansouri Discrimination des critères d'amorçage de craquelures: PVC rigide (non plastifié), Communication, RNJCP 2009, Faculté, Mbem Sik (Casablanca) (2009)

[3] Y. Aminanda, B. Castanié, Modélisation de l'indentation des structures sandwichs à peaux métalliques, Mécanique & Industries 6 (2005), 487–498 DOI: 10.1051/meca:2005061

[4] Van der Giessen E, Lai J Proc. 10th Int. Conf. On Deformation, Yield and Fracture of Polymers (1997)

[5] Tijssens MGA, Van der Giessen E, Sluys LJ (2000) Mech Mat 32:19

[6] Kausch, H.-H., Polymer fracture, 2nd ed., Springer-verlag, Berlin (1987)

[7] C. G'Sell, J. M. Haudin introduction à la mécanique des polymères, Editors INPL, Nancy, (**1995**), vol. 1.

[8] S. K. M. Ting, J. G. Williams, A. Ivankovic, Engineering Fracture Mechanics, Fracture and Damage Mechanics, 71 (**2004**) 4–6, 657–668

[9] Argon AS, Hannoosh JG, Phil Mag 36 (**1977**), 1195

[10] Sternstein SS, Myers FA, J Macromol Sci –Phys B 8 (**1973**), 539

[11] Gearing B.P., Anand L. On modelling the deformation and fracture reponse of glassy polymers due to shear yielding and crazing. Int J Sol. Struct. 41 (**2004**), 3125–3150

[12] Ishikawa M., Sato Y., Higuchi H. Polymer, 37 (**1996**) 7, 1177–1181

[13] Fokam Bopda Christian, Chergui M., Ghorba M., K. Mansouri (2009) Impact tube en PVC rigide, Démarche de validation d'un modèle numérique revue ClicEdition, livre: Les avancées en Mécanique, Tendance de la Modélisation ET Nouvelles techniques expérimentales (Algérie, Bikskra) Ref: 0165-C04/ CAM2009

A COMPARATIVE ANALYSIS OF THEORETICAL MODELS AND EXPERIMENTAL RESEARCH FOR SPRAY DRYING

PRIMERJALNA ANALIZA TEORETIČNIH MODELOV IN EKSPERIMENTALNA RAZISKAVA RAZPRŠILNEGA SUŠENJA

Dragisa Tolmac, Slavica Prvulovic, Dragana Dimitrijevic, Jasna Tolmac

University of Novi Sad, Technical faculty "Mihajlo Pupin", Djure Djakovica bb, 23000 Zrenjanin, Serbia
dragisat@gmail.com

Spraying is very often applied in the chemical and food-processing industries. It includes the spraying of a suspension – spraying with a content of about 30 % to 65 % of a dry substance. The drying time is in most cases only several seconds. In this work the convective drying principle in warm air is presented.

A mathematical model of momentum, heat-and-mass transfer in the atomization-swirler zone was proposed. An uneven distribution of particles and entrainment effects were taken into account in the model. To verify the model an extensive experimental investigation was performed on water evaporation at different initial air temperatures, feed rates, flow rates of the drying agent for different parameters of the atomization and initial particle size distribution. Changes in the air temperature inside the stream of sprayed material, material temperature, evaporation rate, and changes in the Sauter diameter and the distribution of particle diameter vs. their distance from the atomizer were determined experimentally. Good agreement between the experimental results and the theoretical data was achieved.

In the paper an attempt was made to apply the model to the calculation of spray drying in a pilot-plant dryer. The air supplied to the dryer tangentially to the axis was characterized by a high swirl. In order to consider the swirl air flow pattern in the dryer, changes in heat-and-mass balance were made for the particle-drying agent system. The model was verified experimentally on the basis of results of investigations on the drying of a 55 % mass solution of starch and water.

It was found that our model described the process of drying in the analyzed system. An extensive literature survey on spray drying, including unsteady-state phenomena, is presented in the paper. The main sources of errors occurring in the modeling of the spray drying process were discussed. A critical estimation of the existing mathematical models of the process was made and some of them were described in detail.

Key words: spray dryer, model, evaporation, temperature distribution

Razprševanje je pogosto uporabljeno v prehrambni industriji in obsega razprševanje emulzije s 30–65 % suhe snovi. Čas sušenja je največkrat nekaj sekund. V tem delu obravnavamo princip konvektivnega sušenja v toplem zraku. Predlagamo model, ki obsega moment, transfer mase in toplote v coni atomizacije in vrtinčenja, neenakomerno porazdelitev delcev in efekte srkanja. Za verifikacijo modela je bila izvršena obsežna eksperimentalna raziskava izparevanja vode z zrakom z različnimi temperaturami zraka, hitrostjo napajanja, hitrostjo sušenja sušilnega sredstva, parametri atomizacije in z začetno porazdelitvijo delcev. Spremembe temperature zraka v toku razpršenega materiala, temperatura materiala, hitrost izparevanja, spremembe premera Sauter in porazdelitev premera delcev v odvisnosti od razdalje od atomizatorja so bile določene eksperimentalno. Doseženo je bilo dobro ujemanje eksperimentalnih in teoretičnih rezultatov. Obravnavan je bil tudi poskus uporabe modela za izračun razpršilnega sušenja v pilotnem sušilniku. Za zrak, ki je bil tangencialno vpihovan v sušilnik, je značilno močno vrtinčenje. Da bi se upošteval vpliv tega vrtinčenja, sta bili spremenjeni bilanci toplote in mase sistema delec – sušilno sredstvo. Model je bil eksperimentalno preverjen na podlagi rezultatov sušenja 55-odstotne vodne raztopine škroba. Ugotovljeno je, da model dobro opisuje proces sušenja v analiziranem sistemu. V članku je tudi pregled literature o razpršilnem sušenju in obravnavane so najvažnejše napake pri modeliranju. Kritično so ocenjeni dosedanji matematični modeli procesa. Nekateri pa so detaljno opisani.

Ključne besede: razpršilni sušilnik, model, izparevanje, porazdelitev temperature

1 INTRODUCTION

Different suspensions of certain products react with uneven drying, which depends on the properties of the material that is dried. It is very difficult to recommend a unique technique for spray driers. In comparison with other systems, spray drying requires a relatively small storage space. The service and maintenance are very simple and can be performed with little labor. These advantages and an economical heat transfer provide the optimal cost of the final dried product. The drying time is in most cases only a few seconds and sensitive products, such as vitamins, chemical and food products and others, who better submit to a high temperature in a short period of time, but lower temperatures for a longer period of time could be dried.

For substances and materials with over 30 % of moisture, spray drying is a good solution to the problem of drying.

Thanks to the principle of convective drying, the dried material and contact drying agent, the system receives intensive exchange of heat and mass and is very difficult to give an adequate mathematical model of the process, given the complex processes of heat-and-mass transfer involved.

There have been many attempts to formulate a mathematical description of spray drying since the

1950s. In spray drying there are many phenomena that are difficult to represent in the form of a mathematical model. For many years the polydispersity of spray, entrainment effects, or problems of internal heat-and-mass transfer in the disperse phase have been inadequately considered in models. In practise, models of the process that have been created since the beginning of the 1970s were concerned only with the flow of the drying agent.

A significant advancement was achieved in the 1970s, when the principles of momentum, heat-and-mass balances between the continuous and disperse phases [1] (for monodisperse spray and plug flow of the air), and especially when was presented a model in which the entrainment effects and non-uniformity of atomization were accountable were formulated [2]. The solution of the model of spray drying taking into account axial and tangential velocity distributions of air was presented, also. All the aforementioned relations (the entrainment rate and the hydrodynamics of the drying agent) were determined empirically. In further publications the researchers presented many successful applications of their model both in the modelling and the scaling-up of the process. The simple model was recognized by many researchers and studies based on this model have been published [3].

However, the biggest change occurred when the so-called particle source in the cell (PSI-cell) model for gas-droplet flows was proposed [4]. A method for solving the Navier-Stokes equations and the continuity equation was developed where the droplets were treated as sources of mass, momentum and energy to the gaseous phase. In the model, the gas flow field and droplet trajectory are recalculated sequentially until the flow field fails to change with repeated interactions. In the model proposed originally [1] many simplified assumptions were made that referred mainly to the calculation of trajectories and the temperature of the particles. Further extensive studies resulted in developing more sophisticated versions of the PSI-cell model, also including commercial packages such as FLOEW3D and PHOENIX.

The PSI-cell-type models were used successfully to predict such subtle phenomena as the analysis of low-frequency oscillations in the flow field inside the spray drying chamber [5], a determination of the conditions in which recirculation zones appear in the chamber [6] or the effects of inlet air geometry and cone angle on the wall deposition rate [7].

It should be stressed, however, that a practical application of the PSI-cell-type model requires profound knowledge of spray drying and some experience in the programming and calculation of systems with distributed parameters. One problem, which is still unsolved, is the choice of a turbulence model that should be applied in the calculations [8] in such a way that the theoretical results obtained are as near as possible to the experimental values.

Therefore, there is still a considerable demand for simple models that can be used to optimize the process, to minimize its costs, and to evaluate product quality [9]. However, there are many publications of a classical construction representing new concepts of mathematical models of spray drying and offering an extensive description of the whole process [10].

The quality of a spray-drying simulation depends not only on the on the quality of the applied mathematical model but also, and sometimes mainly, on the accuracy of the determination of the initial parameters of the process, and, in particular, the parameters of atomization (mainly the initial particle size distribution and the spray cone angles). An error made in this stage is carried forward and may cause the results obtained to disqualify the modelling process fully, irrespective of the type of model applied.

In the literature, several interesting attempts have been undertaken to overcome this problem. It was proposed to determine experimentally the air temperature distributions in the dryer chamber and then to apply the results directly as the input in the integral equations for the simulation of heat-and-mass transfer of the process [11]. Unfortunately, the experimental determination of the temperature profiles in the dryer is as difficult as the determination of atomization parameters. It also proposed to perform calculations for a randomly generated initial particle size distribution. The model requires an assumption of the air temperature distributions in the dryer [12,13]. The authors state that the model can be developed in such a way that the temperature can be calculated iteratively. However, so far neither has its developed a version of the model been proposed nor has its experimental verification been given.

In this paper, an attempt was made to formulate our own mathematical model for spray drying, which, based on the classical methods for balancing the transport processes between the continuous and disperse phases, would make it possible to analyze the phenomena on the level accessible only to PSI-cell-type models. The proposed model is a development of the concept presenting a theoretical method for the calculation of the entrainment rate [14]. One of the aims of the study was to apply the model and to verify it experimentally in two different drying systems (flat air velocity profile, pressure nozzle, evaporation of water and high swirl air-flow pattern in a chamber, two-fluid nozzle and drying of solution containing dissolved solids.).

2 MODEL OF THE PROCESS

The spray envelope was divided into two regions: the spray boundary region and the spray core region. The spray boundary region is determined by the location of the particles of the atomized material. A change in the location of the particles towards the radial direction also means an increase in the spray diameter and the amount

of air inside the spray which comes into contact with particles. The amount of air which controls the spray can be determined by defining the position of the particles as a function of the distance to the atomizer – swirler. The main assumption made when developing the model is the following: if spraying is monodispersive, or if only one fraction of particles is considered, then in the cross-section of the spray the temperature and air humidity are distributed evenly. The temperature and humidity gradients appear when the atomization is polydispersive. This distribution can be determined by solving the subsequent heat-and-mass transfer equations for particular fractions.

If the air velocity profile is flat, the total amount of air which should be taken into account in the heat-and-mass balance will be the sum of the air flowing through the main core of the spray and the air dw_g that entered the spray, determined by the change in the position of the particles (**Figure 1**).

The position of the particle as a function of the distance to the atomizer can be calculated from the generally known transfer equations that have the following form for three dimensions:

$$\frac{dU_{px}}{dh} = \left[\left(1 - \frac{\rho_g}{\rho_p}\right)g - \frac{3}{4}C_d \frac{U_p(U_{px} - U_{gx})\rho g}{\rho_p d_p}\right]\frac{1}{U_{px}} \quad (1)$$

$$\frac{dU_{pr}}{dh} = \left[\frac{U_{pt^2}}{r} - \frac{3}{4}C_D \frac{U_p(U_{pr} - U_{gr})\rho g}{\rho_p d_p}\right]\frac{1}{U_{px}} \quad (2)$$

$$\frac{dU_{pt}}{dh} = \left[-\frac{U_{pt}}{r} - \frac{3}{4}\frac{3}{4}C_d \frac{U_p(U_{pt} - U_{gt})\rho g}{\rho_p d_p}\right]\frac{1}{U_{px}} \quad (3)$$

where U_p is the relative particle velocity calculated from

$$U_p = [(U_{px} - U_{gx})^2 + (U_{pr} - U_{gr})^2 + (U_{pt} - U_{gt})^2]^{1/2} \quad (4)$$

In the case of flat velocity profiles in the systems, Eqs. (1)–(4) will be simplified, as $U_{gr} = U_{gt} = 0$. The tangential and radial locations of participles will be determined from

$$\frac{dr}{dh} = \frac{U_{pr}}{U_{px}} \quad (5)$$

$$\frac{dx_t}{dh} = \frac{U_{pr}}{U_{px}} \quad (6)$$

If at first the mass balances for a solid-gas system, assuming that atomization is monodispersive or that only one fraction of the dispersed material is to consider and assume that in the stream cross-section, there is neither a temperature nor an air humidity gradient and that continuous and dispersed phases are concurrent.

The mass balance has the form in **Figure 1** and it is given by equation [7].

$$w_g Y + w_1 X + dw_g Y_o =$$
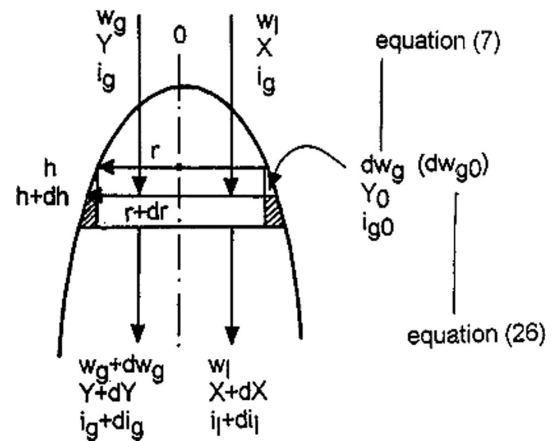$$= (W_g + dw_g)(Y + dY) + w_1(X + dx) \quad (7)$$

Figure 1: Heat-and-mass transfer balances for spray-air system
Slika 1: Bilance prenosa toplote in mase za sistem razprševanje – zrak

With the transformation we obtain where Y_0 is the bulk humidity (outside the stream).

$$\frac{dY}{dh} = \frac{dw_g}{dh}\frac{Y_0 - Y}{W_g} - \frac{w_2}{w_g}\frac{dX}{dh} \quad (8)$$

Similarly, a heat balance for both phases can be derived (**Figure 1**):

$$w_g i_g + w_1 i_1 + dw_g i_{g0} =$$
$$= (w_g + dw_g)(i_g + di_g) + w_1(i_1 + d_i) \quad (9)$$

After the transformation we obtain:

$$dw_g i_{go} = w_g\,di_g + dw_g i_g + w_1 di_1 \quad (10)$$

Humid air and material enthalpies are described by the equations

$$i_g = c_{gs} T_g + (cvTg + \Delta H)Y \quad (11)$$

and

$$i_1 = (Xc_w + c_s)T_1 \quad (12)$$

through the calculation of the derivatives of air and material enthalpies from

$$di_g = c_H dT_g + (cvTg + \Delta H)dY \quad (13)$$

and

$$di_1 = (Xc_w + c_s)\,dT_1 + c_w T_1\,dX \quad (14)$$

and subsequent substitution into Eq. (10), we obtain the equation that can be used to determine the gas temperature in the stream cross-section taking into account entrainment effects

$$\frac{dT_g}{dh} = \frac{1}{w_g C_h}\left[(i_{go} - i_g)\frac{dw_g}{dh} - w_g(c_v t_g + \Delta H)\frac{dY}{dh} - \right.$$
$$\left. - w_1(Xc_w + c_s)\frac{dT_1}{dh} - w_1 c_w T_1 \frac{dx}{dh}\right] \quad (15)$$

The entrainment rate dw_g/dh can be determined on the basis of the increment of the stream cross-section (**Figure 1**):

$$\mathrm{d}w_{\mathrm{g}} = \frac{U_{\mathrm{gx}}\rho_{\mathrm{g}}}{1+Y}\left[\pi(r+dr)^2 - \pi r^2\right] \qquad (16)$$

therefore, the entrainment rate can be determined from

$$\frac{\mathrm{d}w_{\mathrm{g}}}{\mathrm{d}h} = 2\pi\frac{U_{\mathrm{pr}}\rho_{\mathrm{g}}}{1+Y}\frac{\mathrm{d}r}{\mathrm{d}g} \qquad (17)$$

Where the increment of the stream diameter dr/dh is calculated from Eq. (5).

A complete description of the process requires a determination of the humidity and material temperature in the process.

To evaporate water from a solution containing solid material of moisture X, the mass balance has the form

$$\frac{\mathrm{d}x}{\mathrm{d}h} = \frac{W_{\mathrm{D}}(1+x)}{\rho_{\mathrm{g}}V_{\mathrm{p}}}\frac{1}{U_{\mathrm{px}}} \qquad (18)$$

where w_{D} is the evaporation rate given by

$$W_{\mathrm{D}} = fNkS_{\mathrm{p}}r_{\mathrm{g}}(Y^* - Y) \qquad (19)$$

and f is the relative drying rate defined by

$$\int\frac{x-x_0}{x_{\mathrm{cr}}-X_{\mathrm{e}}} \qquad (20)$$

where the subscript e refers to the equilibrium between the gas and the solids and the subscript to the critical point, above which drying is unhindered and the drying rate depends solely on the rate of heat transfer to the material.

In the case of drying of a solution containing solid material, the drying is unhindered until a crust forms on the droplets. The moisture content during crust formation is the critical moisture content. For a moisture content higher than the critical content or to evaporate the solution that does not contain solid material, the value of f should be substituted as unity.

The heat balance for a particle material enables a determination of the particle temperature as a function of the distance to the atomizer. The heat delivered to the particle will be used to evaporate the particle:

$$\mathrm{d}(m_{\mathrm{p}}c_{\mathrm{p}}T_{\mathrm{p}}) = [k_{\mathrm{h}}S_{\mathrm{p}}(T_{\mathrm{g}} - T_{\mathrm{p}}) - W_{\mathrm{D}}/N(\Delta H + c_{\mathrm{v}}Tg)]\mathrm{d}t \qquad (21)$$

Assuming that changes in the drying process concern mainly the moisture content and temperature, the left-hand side of Eq. (21) can be transformed to:

$$\mathrm{d}(m_{\mathrm{p}}c_{\mathrm{p}}T_{\mathrm{p}}) = \mathrm{d}[r_{\mathrm{p}}v_{\mathrm{p}}(c_{\mathrm{s}} + c_{\mathrm{w}}X)\,T_{\mathrm{p}}] = \\ = r_{\mathrm{p}}V_{\mathrm{p}}[(C_{\mathrm{s}} + C_{\mathrm{w}}X)\,\mathrm{d}T_{\mathrm{p}} + c_{\mathrm{w}}T_{\mathrm{p}}\mathrm{d}x] \qquad (22)$$

Substituting the right-hand side of Eq. (22) into (21), we obtain after rearrangements

$$\frac{\mathrm{d}T_{\mathrm{p}}}{\mathrm{d}h} = \frac{6a(T_{\mathrm{g}} - T_{\mathrm{p}}) - \left[W_D N(\Delta H + C_v T_g)\right]s_p}{d_{\mathrm{p}}\rho_{\mathrm{p}}(c_{\mathrm{s}} - c_{\mathrm{w}}X)} + \\ + \frac{U_{\mathrm{px}}c_{\mathrm{w}}T_{\mathrm{p}}}{C_{\mathrm{s}} + c_{\mathrm{wX}}}\frac{1}{U_{\mathrm{px}}} \qquad (23)$$

In this process, a continual change in the particle diameters takes place, which has a significant effect on

heat-and-mass transfer coefficients and on the drag coefficient. The actual particle diameter can be determined from [1]:

$$d = d_{\mathrm{p0}}\left(\frac{P_{\mathrm{sw0}} - P_{\mathrm{w}}}{P_{\mathrm{sw}} - P_{\mathrm{w}}}\right) \qquad (24)$$

For a moisture content lower than the critical.

The particle diameter no longer decreases and thus Eq. (24) ceases to be valid.

In all calculations, heat-transfer coefficients were determined from the Ranz-Marshall equation and mass-transfer coefficients from the Chilton-Colburn analogy, where the psychometric coefficient and humidity potential coefficient were taken as unity.

The model described above can be solved in the following way:

1. For monodispersive atomization, the solution of Eqs. (1)–(24) is used to calculate all the process parameters taking into account the entrainment effects.

2. For polydispersive atomization assuming constant air temperatures and humidities in the cross-section of the spray, the evaporation rate (Eq. (19)) should be calculated as a sum of the evaporations from particular fractions i:

$$W_{\mathrm{d}} = \sum_{i-1}^{n} -1\int N_{\mathrm{i}}\,k_{\mathrm{i}}\,S_{\mathrm{pi}}\,\rho_{\mathrm{g}}(Y^* - Y) \qquad (25)$$

For the entire stream of atomized material, the entrainment rate (Eq. (17)) can be calculated on the basis of the motion of the largest diameter particles. Heat-and-mass balance equations for particles solved separately for particular fractions are used to calculate temperatures, moisture contents and the position of the particular fraction in the dryer.

For polydispersive atomization when the air humidity and temperature distributions in the spray cross-section, the system of model equations should be solved
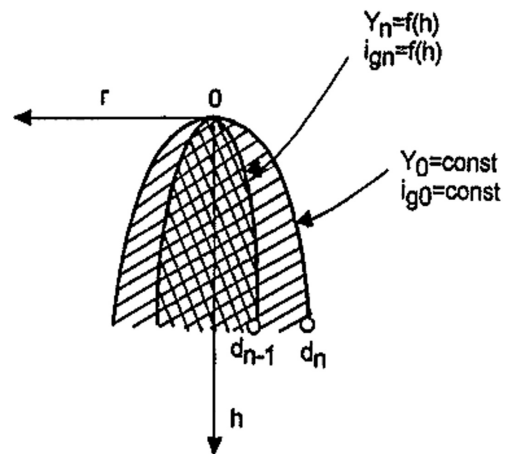
Figure 2: Calculating of humidity and temperature distribution in spray
Slika 2: Izračun porazdelitve vlage in temperature v curku

individually for each fraction starting with the particles of the largest diameter d_{pn}. A uniform temperature and air humidity field T_{gr} and Y_{ng} will be obtained in the stream cross-section. The files should be stored in the computer's memory because the motion of the next fraction of particles of diameter d_{pn-1} will take place in the field of gas humidity Y_n and temperature T_{gn} determined by the fraction of diameter d_{pn} (**Figure 2**).

Proceeding in this way, we will obtain the temperature and air humidity distributions in the stream cross-sections: the more fractions that are considered the more accurate is the final calculated result.

3 EXPERIMENTAL DETAILS

To test the proposed mathematical model, experimental investigations were carried out in a dry 55 % solution of starch and water in spray drying. **Figure 3** shows a schematic of the experimental equipment of the spray dryer in which the experiments took place. In **Table 1** are given the basic characteristics of the spray dryer.

Table 1: The basic characteristics of the spray-drying chambers

Name	Units	Dimensions
Diameter chamber spray dryer	(mm)	5000
Elevation spray drying chamber	(mm)	5500
Cyclone diameter	(mm)	1400
Power fan	(kW)	18.5
Air flow	(m³/h)	9750–14400
Atomizer (swirler)	(kW)	0.75
Electric motor r/min	(min⁻¹)	3800

Inlet air drying is done by fans (3). Air over the absorptive heater (4), with the help of fans (3). Thermal power heater (4), can be regulated in the range 40–65 kW. The material is drying leads through the entrance
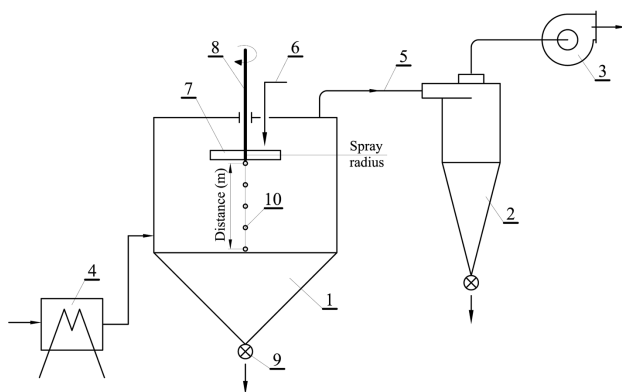

Figure 3: Schematic of the experimental plant spray dryer: 1 – chamber spray dryer, 2 – cyclone, 3 – fan, 4 – heater, 5 – air outlet, 6 – supply of material, 7 – swirler (atomizer), 8 – drive axle, 9 – rotary feeder, 10 – measuring points
Slika 3: Shema eksperimentalnega sušilnika: 1 – komora sušilnika, 2 – ciklon, 3 – vetrilo, 4 – grelnik, 5 – dovod zraka, 6 – dovod materiala, 7 – razprševalnik (atomizer), 8 – gonilna os, 9 – vrteči se napajalnik, 10 – merilne točke

(6). Material for drying (55 % mass solution of starch and water), empties into the atomizer (7) with the axle (8) using electric propulsion. Spray nozzle rotates with an rpm of n = 3800 min⁻¹ and disperses the liquid solution in small droplets. Aerosols are derived in the form of a rotational disc with the diameter of 320 mm and with a paddle. The extensive spray speed is 63.5 ms⁻¹.

In contact with hot gas – air drying dispersed droplets one obtains and the intensive exchange of heat and mass is achieved. Air flow to the fan (3), can be regulated, and the drying air velocity V = (0.17 to 0.24) ms⁻¹ can be obtained.

The dried material using the rotary feeder is transported as a finished product (9). Air with dust particles are drains with the piping (5) in the cyclone (2) and the completion separation is achieved and discharged in the atmosphere using fans (3).

4 MEASURING METHODS

The main part of the paper is concerned with the measurement of the air and material temperature in the spray, the evaporation intensity, and the particle size distribution for various air-flow velocities, feed rates, inlet air temperatures and spray cone angles. The temperature profiles of the air and atomized material as a function of the distance to the nozzle were determined by means of type T thermocouples and an EMT-02 temperature meter. To determine the temperature of the gas flowing inside the spray, the thermocouples were placed in special Teflon casings with an l8 mm external diameter. The Teflon casing diameter was selected on the basis of numerous tests as it achieved a stable temperature read-out. A similar measuring technique was used by [17]. To measure the evaporation intensity, a specially designed measuring plate was used. This plate was inserted into the funnel through the hatches in the measuring section where atomized material was collected on the whole cross-sectional area of the tunnel, which made it possible to calculate the evaporation intensity.

The change in the particle size distribution of the atomized material as a function of the distance to the spray nozzle was determined using the method of image analysis. A sample of atomized material was placed in a Petri dish where the surface was covered with a layer of non-volatile silicone oil. The image obtained from a microscope and camera was recorded on a video cassette, and then processed by a microcomputer image analyzer (IMAL 2561128). To minimize the statistical error for every analyzed sample, 600 particle size distributions of the atomized material were calculated [15,16]. The ambient air temperature and humidity were also measured with a THERM 2285-2 meter produced by Alhborn with the probe FH 9626 -11.

5 EXPERIMENTAL RESULTS AND DISCUSSION

One of the main sources of error in the spray drying simulation is an imprecise specification of the initial process parameters, for example, the spray cone angle and particle size distribution. The parameters were carefully determined for each swirl insert and for each feed rate. Experimental investigations of the water evaporation were carried out for three feed rates (98, 135, 157) kg h^{-1}, and three values of air temperature (80, 100, 130) °C. An example of the initial particle size distribution obtained at feed rate of 98 kg h^{-1} is shown in **Figure 4**.

Both in this case and for other values of the initial atomization parameters a characteristic log-normal particle size distribution was obtained. The experimental investigations show that the character of the distribution does not change as a function of the distance to the atomizer-swirler in all experimental runs.

All theoretical calculations were made with the assumption that the sign of negligible changes in the air and material temperature in the cross-section of atomized material spray which was confirmed experimentally.

The increase of the temperatures in the cross-section spray dryer is only slight, **Figure 5**. The absence of an air temperature gradient in the spray cross-section can be explained with the design of the experimental set-up and by process parameters. The air-velocity profile in the tunnel of the dryer is flat and the turbulence is low. In the study is up [18] a temperature distribution along the spray dryer radius was observed and similar results were obtained.

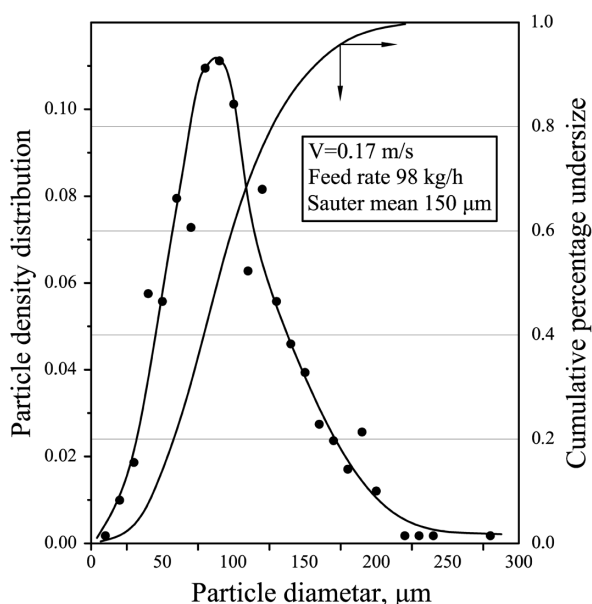As simulation calculations show that in agreement with experimental observations(in all experimental trials
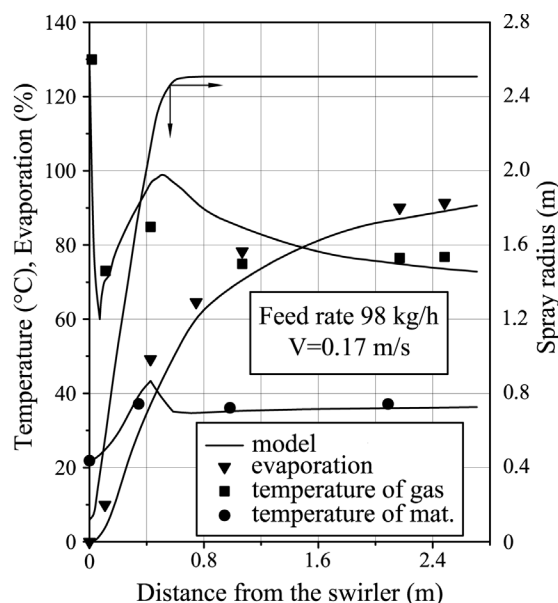

Figure 5: Comparison of theoretical and experimental results
Slika 5: Primerjava teoretičnih in eksperimentalnih rezultatov

no wetting of the tunnel wall was reported) the particle of diameter corresponding to a 95 % cumulative percentage undersize did not contact the walls of the tunnel dryer, **Figure 5** shows a comparison between the theoretical and experimentally calculated changes in the air temperature, material and evaporation rate as a function of the distance from the atomizer for the same feed rate and air-flow velocity. A theoretically calculated spray radius is also plotted on the same graph. A rapid drop in the air temperature and then its characteristic rise are related to entrainment effects. An increase in the amount of air in the spray due to its expansion causes the
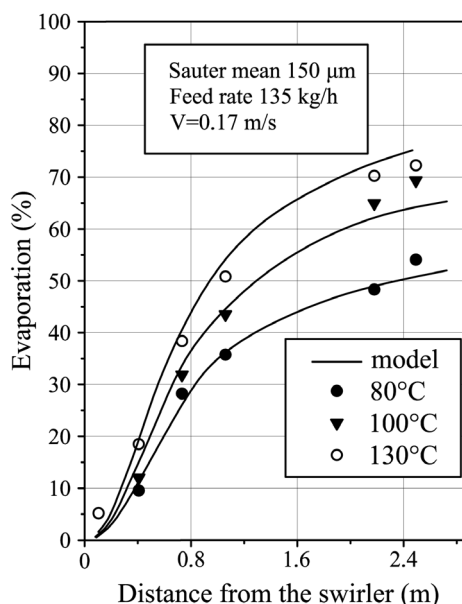

Figure 4: Initial particle size distribution
Slika 4: Začetna porazdelitev velikosti delcev

Figure 6: Evaporation at different air temperatures
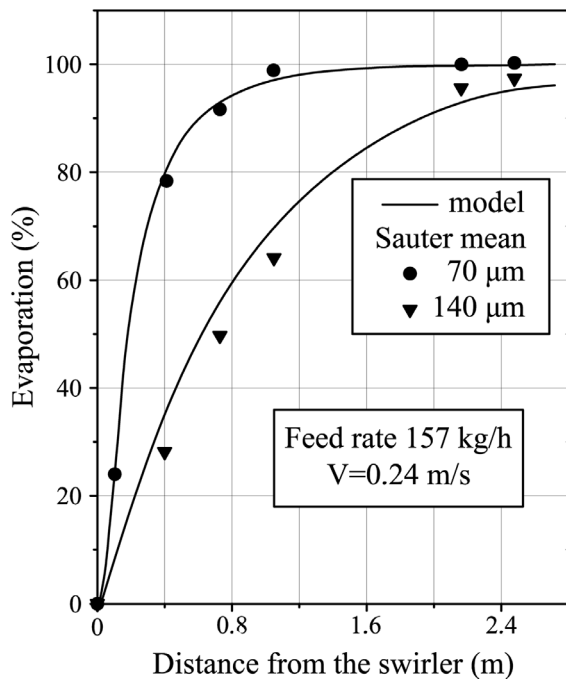**Slika 6:** Izhlapevanje pri različnih temperaturah zraka

Figure 7: Effect of sauter mean on evaporation rate
Slika 7: Vpliv povprečja Sauter na hitrost izhlapevanja

temperature to rise despite intensive evaporation, until the moment when the balance occurs between the heat used for evaporation and the heat supplied into the spray by the entraining air is achieved. After this time a drop in the air temperature as a function of the distance to the atomizer is observed. Similar profiles of particular functions were obtained in many studies [17].

The experimental results shown in **Figure 6** illustrate the changes in the evaporation rate along the tunnel of the dryer for different temperatures of the drying agent. Air temperature has a decisive effect on the evaporation rate. No significant influence of the drying agent velocity on the shape of the curves discussed was observed. Particles achieve a zero relative velocity after a short period of time, which limits the convective heat transfer between the continuous and disperse phases.

Lack of air circulation zones in the tunnel causes the spray to compact and move parallel to the tunnel of the dryer walls. The very good agreement between the theoretical and experimental results is worthy of note.

The final figure discussed (**Figure 7**) shows the effect of the initial particle size distribution on the evaporation rate at the same air temperature and feed rates. The analyses of the results show that the character of the initial particle size distribution has a remarkable influence on the whole evaporation process. Particles with a smaller Sauter mean diameter are evaporated much faster than particles having larger mean diameters. In the case when the initial particle size distributions are similar, the feed rate is the parameter that determines the evaporation rate. Good agreement between theoretical and experimental results was also obtained in this case.

6 CONCLUSIONS

A mathematical model of momentum, heat-and-mass transfer during spray drying was proposed and verified. The model of a classical construction reflects the majority of phenomena occurring between the conclusions and dispersed phases during atomization. The main difference between the proposed model and the models described in the literature is the balancing of the transport processes between the continuous and disperse phases. It is possible to describe the trajectories of the particle fractions and take into account the entrainment effects. The model was verified both for the system of simple as well as complex drying agents and for the solution containing solid particles. The model presented in this paper can be used to predict many subtle phenomena that occur during spray drying, in particular during complex air flow. In all theoretical simulations of the drying process of evaporation, reasonable agreement with the experimental data was achieved.

7 REFERENCES

[1] Bellinghausen, R., Esper G. J., Gehrmann, D., Scale-up of spray driers on the basis of laboratory scale experiments, Meet. of the EFChE Drying Working Party, Utrecht, **1993**

[2] Crowe, C. T., Sharma, M. P, Stock, D. E., The particle-source- in-cell (PSI-cell) model for gas-droplet flows, J. Fluid Eng., 99 (**1977**), 325–334

[3] Gauvin, W. H., Katta, S., Basic concepts of spray drying design, AIChE J., 22 (**1976**) 4, 713–724

[4] Kuts, P. S., Samsonyuk, V. K., Akulich, P. V., Liquid phase distribution in a spray formed by pneumatic nozzle in the spray dryer chamber, in A. S. Mujumdar (ed.), Drying'92, Part A, Elsevier, Amsterdam, (**1992**), 543–550

[5] Langrish, T. A. G. and Zbiciński, I., The effects of air inlet geometry and spray cone angle on the wall deposition rate in spray dryers, Trans. Inst. Chem. Eng. A, 72 (**1994**), 420–430

[6] Larrgrish, T. A. G., Oakley, D. E., Keey, R. B., Bahu, R. E., Hutchinson, C, A., Time-dependent flow patterns in spray dryers, Trans. Inst. Chem. Eng., 71 (**1993**), 355–360

[7] Lefebvre, A. H, Atomization and sprays, Taylor & Francis, Bristol, USA, 1989

[8] Livesley, D. M., Oakley, D. E., Gillespie, R. F., Elhaus, B., Ranpuria, C. K., Taylor, T., Wood, W., Yeoman, M. L., Developments and validation of a computational model for spray-gas mixing in spray dryers, in A. S. Mujumdar (ed.), Drying'92, Part A, Elsevier, Amsterdam, (**1992**), 407–416

[9] Miura, T., Othani, S., Maeda, S., Heat and mass transfer to and from sprays, in A. S. Mujumdar (ed.), Drying'80, Vol. 1, Hemisphere, McGraw Hill, New York, NY, 1 (**1980**), 351–356

[10] Oakley, D. E., Bahu, R. E., Spray/gas mixing behaviour with spray dryers, in A. S. Mujumdar and I. Filkova (eds.), Drying 9.1, Elsevier, Amsterdam, (**1990**), 303–313

[11] Papadakis, S. E., King, C. J., Air temperature and humidity profiles in spray drying. 1. Features predicted by the particle source in cell model, 2. Experimental measurements, Ind. Eng. Chem. Res., 27(**1988**) 11, 2111–2123

[12] Parti, M., Palancz, B., Mathematical model for spray drying, Chem. Eng Sci., 29 (**1974**), 355–362

[13] Prvulovic, S., Tolmac, D., Blagojevic, Z., Experimental research on energetic charakteristics of starch dryer, FME Transactions, 37(**2009**) 1, 47–52

[14] Satija, S., A scale-up study of nozzle tower spray dryers, Drying Technol., (**1987**) 1, 63–85

[15] Som, S. K., Mitra, A. K., Sengupta, S. P., Evaporation, drop Som, S. K., Mitra A. K., Sengupta, S. P., Evaporation, drop Iiquid spray containing dissolved solids in a convective medium, Drying Technol., 8 (**1990**) 3, 571–591

[16] Tolmac, D., Introduction to the Theory of Drying with Examples from Practice, Technical Faculty, Zrenjanin, Serbia, 2007

[17] Zbiciriski, I., Grabowski, S., Strumillo, C., Kiraly, L., Krzanowski, W., Mathematical modelling of spray drying, Comput. Chem Eng., 12 (**1988**) 2/3, 209–214

[18] Zhelev, J. B., Experimental investigation of flow pattern in a spray dryer, Drying Technology 7 (**1989**) 3, 74–85

CREEP RESISTANCE OF MICROSTRUCTURE OF WELDS OF CREEP RESISTANT STEELS

ODPORNOST PROTI LEZENJU PRI MIKROSTRUKTURI ZVAROV JEKEL, ODPORNIH PROTI LEZENJU

Franc Vodopivec, Monika Jenko, Roman Celin, Borut Žužek, Danijela A. Skobir

Institute of Metals and Technology, Lepi pot 11, SI-1000 Ljubljana, Slovenia
franc.vodopivec@imt.si

Welds are essential parts of tube systems in high temperature power works producing electrical energy and have a heterogeneus microstructure due to the welding gradient of temperature and cooling rate. A short summary is given of findings related to the creep resistance of welds of creep resistant steels. In the majority of references it was found that creep resistance was lower for the intercritical part of heat affected zone (HAZ). The effect of potential changes of intercritical microstructure on creep rate at exploitation is discussed.

Key words: creep resistant steel,welds, creep rate, HAZ, intercritical zone

Zvari so bistvena komponenta cevnih sistemov v termoelektrarnah, njihova mikrostruktura pa je heterogena zaradi gradienta temperature in ohlajanja pri varjenju. Pripravljen je bil kratek pregled ugotovitev v zvezi z odpornostjo različnih delov cone toplotnega vpliva varjenja (TVC) proti lezenju v dosegljivih virih. Večina virov navaja, da je odpornost najnižja v področju, kjer je bilo med varjenjem jeklo segreto v interkritično področje CTV. Analizirane so mogoče spremembe interkritične mikrostrukture in od njih odvisne spremembe hitrosti lezenja.

Ključne besede: jeklo odporno proti lezenju, zvari, hitrost lezenja, TVC, interkritična cona

1 INTRODUCTION

Welds are an essential parts of steels tube systems in thermal power works. The heating cycle of welding, the temperature gradient and cooling rate give to the weld part of tubes, the heat affected zone (HAZ) a heterogeneous microstructure of products of transformation of austenite at cooling. This microstructure depends on the temperature at welding and the cooling rate. It consists of a slightly affected microstructure of basic steel, the products of transformation of cooling from intercritical range, the range of temperature of stability ferrite + austenite and the transformation at cooling of austenite from a temperature up to melting point on the boundary to the deposed metal. Also the HAZ microstructure may be affected by the cooling rate and influenced additionally by reheating at deposition of following welding passes. The heating time is short, however, the local temperature is sufficient for inducing changes of grains size and may even change the quantity and distribution of carbide particles hindering the movement of dislocations and affecting the creep rate. For this reason, the creep resistance of welds of creep resistant steels has received considerable attention. In this work, an abbreviated review of the most significant findings in accessible references is given. Conclusions are proposed with accent on more reliable findings and some so far insufficiently clear facts are mentioned, also. The effect of possible changes of microstructure in intercritical zone on creep rate is examined, also.

2 REVIEW

For a 21Cr steel it was established that the weld metal had a greater creep rate than the base metal due to agglomerate of carbide particles facilitating the cavitation.[1] The creep activation energy of 337.5 kJ/mol was deduced, a value in acceptable agreement with the creep activation energy for α-iron.[2] For the steels 9Cr1Mo and 2.25Cr1Mo, the dissimilar weld joint showed lower creep strength than base steels and the creep deformation was for both steels concentrated in the intercritical (ICZ, $\alpha+\gamma$ range) zone of HAZ.[3] Creep cavities were generated mostly at grain boundaries in ICZ, their number increased with creep deformation that was self-accelerating.[4] Also, it was established that at creep tests at 650 °C and 675 °C, the change of hardness was small for ICZ and great for weld metal, coarse grained HAZ and base metal. Creep failure of welds occurred with IV type cracking in ICZ with the highest generation of voids. HAZ modelling showed for ICZ the higher equivalent stress and strain.[5]

The higher ICZ susceptibility to cracking in welds of a 1.25Cr0.5Mo steel in service may be due to the heterogeneous distribution of precipitates. Close to 90 % of voids are found at grains of size lower than 10 μm. However, 200 to 300 voids per mm² did not shorten significantly the steel rupture time.[6] Calculation showed that ICZ has a higher equivalent strain and high hydrostatic pressure and than the base material submits ICZ to a strong constraint.[7] The distribution of voids and

equivalent stress were similar for all HAZ zones, thus independent on microstructure. Also, it is suggested that hydrostatic pressure may accelerate the coalescence of voids to cracks.[7] The greater crack susceptibility of ICZ may be due to a heterogeneous distribution of precipitates and the greater change of particles morphology during creep.[8]

The grain boundaries sliding hinders the generation of cavities at accelerated creep rate tests.[9] For this reason, the density of cavities could not be an absolute parameter of creep damage effect in ICZ. From strain rate measurements the rupture life can be predicted with reasonable accuracy.[9] The most effective factors reducing the creep rupture strength of welds of steel P 91 are the finer austenite grains that accelerate the growth rate of subgrains from martensite laths and the softer martensite matrix that both increase the rate of softening and creep cavitation.[10]

The intrinsically higher ICZ creep rate is due to the effect of stress triaxiality.[11] Stress relief cracking could occur in coarse grained HAZ because of sulphur and phosphorus segregations.[12] In the investigation of the effect of triaxiality on creep with notched specimens, it was found that the equivalent stress played a major role in the multiaxial rupture life of a 1.25Cr0.5Mo steel.[13] For a similar steel, it was deduced that multiaxial stress could play a key role in the type IV failure of welds and that this failure may be caused by grain boundaries sliding of fine grains produced by the partial transformation at welding.[14] With small punch tests it was found that the creep rupture time of HAZ was by low stress levels shorter than for the base and deposited metal.[15] Also, it was assumed that a film like carbide phase at grain boundaries and coarsening of $M_{23}C_6$ particles may affect the creep rupture strength of HAZ.[15]

For the 9Cr1MoVNbN and 12Cr2MoWVTiB steels the creep damage was greater for undermatched than for equal and overmatched welds and for overmatched welds the failure tendency was higher than for equal matched welds.[16] After normalising at 1050 °C and tempering at 780 °C, the creep rupture strength for HAZ was equal as for the parent steel[17]. For proper understanding and modelling of creep behaviour of welds, it is necessary to know the individual creep strength of different weld regions and the effect of stress multiaxiality that is changed permanently because of creep and relaxation.[18]

The creep rupture strength of cross weld joints is usually about 20 % to 30 % lower than that of the base steel.[19] Also, it was found that in steel P 91 the particles spacing of secondary phases was higher in HAZ than in base steel. Creep strength is for welds identical to that of the base steels up to 575 °C and the creep resistance may be influenced by post-weld heat treatment.[20] Creep fracture occurs in ICZ and the density of creep voids is greater in the interior of the specimen section, where also the multiaxial stress is larger.[21]

The creep strength of the 9 Ce to 12 Cr steels was improved and the formation of small grains in ICZ

suppressed with addition of 0.1 % B because of the grain strengthening effect of this element[22]. In[23] the effect of boron addition is confirmed and is established that no coarsening of carbide particles occurred by 10 000 h creep test at 650 °C. Also, the cross weld stress of boron steel is up to 10 000 h of creep time higher for the weld than for the base steel. The stress concentration in the softened zone of ICZ explains it creep propensity only if the smaller grain size is considered, also.[24]

Up to 575 °C the weld creep strength is in the scatter band of ±20 % of the base steel, while, at higher temperature the weld creep strength is below this range.[25] In HAZ the recovery is faster because of the faster deterioration of laths structure and the decrease of dislocation density that facilitate a faster creep deformation.[26] With small punch tests the localization of creep fracture in ICZ was confirmed especially by small load and a simple relation was established between the punch load and the equivalent stress.[27] Creep damage from preliminary uniaxial tests shortens the time to rupture by small punch test.[28]

The following conclusions and remarks are derived from this review:

– in welds of creep resistant steels the creep resistance of the HAZ intercritical zone (ICZ) is the lowest and the creep rate increased appropriately;

– creep failure occurs with coalescence of grain boundary voids to type IV cracks;

– in operation, creep relaxation occurs that affects the equivalent stress and the creep resistance;

– boron presence in steel increases the creep resistance of the ICZ zone of HAZ;

– reliable weld creep modelling should be based on the effect of operation time and temperature on creep rate for individual constituents of HAZ and on stress multiaxiality;

– data on the accurate creep rate of typical HAZ microstructure constituents are insufficient;

– plastic deformation increases the number of defects in metal lattice and accelerates diffusion and related processes, also diffusion and creep. It is not clear how these processes can be accelerated by stressing without plastic deformation.

3 EFFECT OF CHANGES OF INTERCRITICAL HAZ MICROSTRUCTURE ON CREEP RESISTENCE

In creep resistant steels the creep rate depends on spacing of particles, mostly of carbides of chromium, vanadium, niobium and other metals added in the steel. Two theoretical equations were developed for the dependence of creep rate and particles spacing λ:[29,30]

$$\dot{\varepsilon} = (b^2/k_B TG)\lambda\sigma^2 D \qquad (1)$$

and in the detachment concept of dislocations overcoming of non coherent precipitates[31,32]

$$\dot{\varepsilon} = (6\lambda\rho/k_B TG)\cdot\exp(-E/k_B T) \qquad (2)$$

With $\dot{\varepsilon}$ – creep rate, b – Burgers vector, k_B – Boltzmann constant, T – temperature in K, G – shear modulus, σ – acting stress, D – diffusion coefficient, ρ – density of mobile dislocations and E – creep activation energy.

By constant volume share of carbides f, the particles spacing and carbide particles size d are related with:[30]

$$\lambda = 4d/\pi f^{1/3} \qquad (3)$$

By constant volume share of carbide, the creep rate increases with particles spacing which, by constant volume share of carbide, depends of particles size, thus of particles coarsening rate, also. This rate depends on volume diffusion rate of the main metal bound in carbide phase, fi.: chromium in $M_{23}C_6$ and vanadium and niobium in MC carbides.

For the coarsening of $M_{23}C_6$ carbide particles the experimental coarsening rate was determined[33,34]

$$\Delta d^3_{ce,1073K} = k_{ce,1073K}\, t = 1.48\cdot10^{-26}\, t \qquad (4)$$

The Lifshitz-Slyouzov-Wagner[35] (LSW) equation for coarsening of particles is:

$$\Delta d^3 = 8S\gamma\Omega Dt/9k_B T \qquad (5)$$

With Δd^3 – increase of particles size in time t, S – equilibrium content of carbide constituting metal in solution in the matrix, γ – carbide particle-matrix interface energy, Ω – volume of diffusing atoms, k_B – Boltzmann constant, D – diffusion coefficient and T – temperature in K.

Introducing the parameters for the steel X20 the coarsening kinetics for $M_{23}C_6$ particles in steel X20 tempered at 1073 K the relation was deduced:[34]

$$\Delta d^3_{ce,1073K} = 1.31\cdot10^{-26}\, t \qquad (6)$$

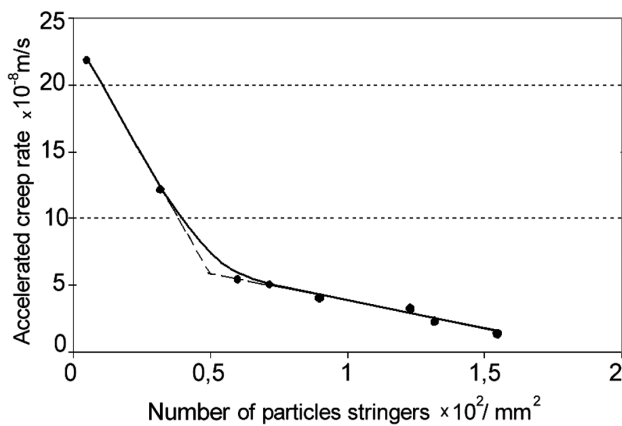This relation is in acceptable agreement with the experimental equation (4).

Figure 1: Dependence of accelerated creep rate on the number of stringers of carbide particles in martensite in 0.18C11.5Cr1.08 Mo0.29V steel.[36]
Slika 1: Odvisnost med hitrostjo pospešenega lezenja in številom nizov martenzitnih izločkov v jeklu 0.18C11.5Cr1.08 Mo0.29V[36]

As shown in **Figure 1**, by equal particle size the creep rate depends strongly on the share of particles in stringers[37].

The number of stringers per unity of surface decreases with tempering time several times more rapidly that particles coarsening. The explanation is the faster growth of particles at grain and subgrain boundaries[38,39,40] very probably because the boundary diffusion is faster then volume diffusion. The kinetics of decrease of the number of stringers of particles the relation was deduced:

$$n_t = n_t - k_n t^x = 1.78\cdot10^8 - 0.706\cdot10^2\, t \qquad (7)$$

with n_t – density of stringers at the time t, n_i – density of stringers at $t = 0$, k_n – rate of decrease of stringers density (m^{-2} s^{-1}) and t – tempering time (s).

After approximately 350 h of tempering at 800 °C the stringers density was diminished below the critical value of about $0.60\cdot10^8$ m^{-2}, the creep rate increased by approximately 8.5 times,[37] while a much lower increase would be attained from the increase of particles spacing if the rate was calculated using equation (1) and the particle spacing calculated using equation (3) based on the experimentally assessed average particles size. These findings suggest that the creep resistance of the intercritical part of HAZ depends to a significant extent of the number if stringers of carbide particles and their stability.

Investigations of the coarsening of carbide particles in a 12Cr steel have shown[41] that in specimens crept for up to 16 000 h at 650 °C by the stress of 80 MPa the coarsening rate of MX particles was 3.73 times greater that in grip part of tested specimens.[34]

Parts of HAZ are heated to a different temperature and a different microstructure is obtained. In some parts of HAZ the temperature is theoretically sufficient for significant change to steel creep resistance, however, because of the short heating time only partial solution of carbide particles is achieved with the greatest solution for VC, lower for NbC and the lowest for $M_{23}C_6$. Accordingly, it is logical to conclude that, especially the particles distribution in parts of HAZ, heated to the theoretical temperature of complete solution of VC and NbC particles and the HAZ part heated at higher temperature, but to low for a sufficient solution of $M_{23}C_6$ particles, the creep rate is higher mostly because of the diminished effect of particles in stringers.

Equations (1) and (2) show that creep rate increases with the density of mobile dislocations which is related to the creep stress (σ), Burgers vector (b) and shear modulus (G)[42] and the constant $\alpha = 0.4$.

$$\rho = (\sigma/\alpha MGb)^2 \qquad (8)$$

For accelerated creep rate tests by $\sigma = 170$ MPa, $G_{853K} = 57.6\cdot10^3$ MPa[32], $M = 3$, $b = 2.5\cdot10^{-10}$ nm, the dislocation density of $\rho = 0.978\cdot10^{14}$ m^{-2} is obtained.[37]

Let us examine how processes of transformation of austenite to martensite and ferrite transformation in HAZ

may affect the mobile dislocation density. These dislocation are generated by plastic deformation. Accordingly, no significant effect could be expected from the generation of elastic stresses by austenite to martensite transformation and their relaxation. By transformation of the mixture of austenite and ferrite, thus by cooling from intercritical temperature, these elastic stresses could relax with slight plastic deformation of ferrite and its mobile dislocation density slightly increased. Thus, the density of mobile dislocations could be slightly increased in parts of HAZ with incomplete ferrite to austenite transformation at heating. Carbide stringers consist for a greater part of $M_{23}C_6$ particles. These particles grow faster because of boundary diffusion[39,40] and the rate of decrease of the density of stringers is much greater than for the average coarsening rate in stringers and the rate of stringers decmposition. For this reason, it is expected that by heating at welding the creep resistance is diminished much less by increase of particles spacing than by the decrease of stringers density and it is logical to conclude that the increased creep rate for the intercritical part of HAZ is due mostly to the decrease of the effect of stringers of carbide particles on creep. After heating at higher temperature, a great part of carbide particles is dissolved in austenite and stringers form again at grain and subgrain boundaries of martensite and their effect on creep rate is restored. This interpretation of processes in HAZ, rsp. at temperature of ferrite + austenite range, would be for the creep resistant steel X20 the logical explanation for two experimental findings: 1) compared to as delivered steel X20, the accelerated creep rate at 580 °C and stress of 170 MPa the creep rate was increased for about one order of magnitude after cooling from $\alpha+\gamma$ range, while it was slightly decreased after cooling from the temperature of total carbide particles solution in austenite and 2) the difference of creep rate was decreased after longer tempering.[43]

4 CONCLUSION

On the base of the review of findings in references, of the analysis of the effects of change of carbide particles size and distribution, it is concluded that the decrease of creep rate for the intercritical part of HAZ of creep resistant steels is due to a wide extent to the decrease of the effect of particles in stringers on the creep process. This conclusion is supported by so far unpublished experimental results on the effect of annealing temperature on accelerated creep rate for the steel X20.

5 REFERENCES

[1] P. Liaw, G. V. Izao, M. G. Burke: Mat. Sci. Eng., 131 (**1991**), 187–201

[2] R. W. K. Honeycombe: The Plastic Deformation of metals, Ed. Arnold, London, 1985

[3] K. Laha, S. Latha, K. B. S. Rao, S. L. Mannan, D. H. Sastry: Mat. Sci. Techn., 17 (**2001**), 1265–1272

[4] N. Komai, F. Masuyama: ISIJ Intern., 42 (**2002**), 1364–1370

[5] K. Shinozaki, De. Jun Li, H. Koroki, H. Harada, K. Ohishi: ISIJ Intern., 42 (**2002**), 1578–1584

[6] S. Fujibayashi, T. Endo: ISIJ Intern., 42 (**2002**), 1309–1317

[7] D. Li, K. Shinozaki, H. Kuroki: Mat Sci.Techn., 19 (**2003**), 1253–1260

[8] S. Fujibayashi, T. Endo: ISIJ Intern., 43 (**2003**), 790–797

[9] S. Fujibayashi: ISIJ Intern., 44 (**2004**), 1441–1450

[10] M. E. Abd El-Azim, A. M. Nasreldin, G. Zies, A. Klenk: Mat Sci.Techn., 21 (**2005**), 779–790

[11] V. Gaffard, A. F. Gourgues-Lorenzon, J. Besson: ISIJ Intern., 45 (**2005**), 1915–1925

[12] A. G. Chapuis, C. L. Davis: Mat. Sci. Techn., 22 (**2006**), 937–943

[13] S. Fujibayashi: ISIJ Intern., 47 (**2007**), 333–339

[14] S. Fujibayashi: Eng. Fract. Mechanics, 74 (**2007**), 932–946

[15] S. I. Kamazaki, T. Sugimoto, Y. Hasegawa, Y. Kohno: ISIJ Intern., 47 (**2007**), 1228–1233

[16] J. Chang, J. He, G. Zhang, Y Zhang: Transactions of the China Welding Institute, 29 (**2008**), 101–104

[17] T. Sato, K. Mitsuhata, K. Tamura, R. Ihara: Long term creep rupture of 9Cr narrow gap welded joints improved by normalising and tempering after welding; 2007 Proc. ASME Pressure Vessels and Piping Conf.- 8th Intern. Conf. on Creep and Fatigue at Elevated temperature- CREEP 8 (**2008**), 669–674

[18] E. Ross, K. Maile, A. Klenk, M. Bauer: Intern. J. of Mat. Research, 99 (2008), 4, 402–409

[19] J. Plumensky, V. Foldina, M. Sondei, D. Schwartz, Y. Koukal: Microstructure and creep rupture strength of welded jonts in the steel 9P 91; 2007 Proc. ASME Pressure Vessels and Piping Conf.- 8th Intern. Conf. on Creep and Fatigue at Elevated temperature- CREEP 8 (**2008**), 503–511

[20] D. Jandova, J. Kasl, V. Kanta: Influence of substructure on creep failure of P91steel weld joints; I. A. Shibli, S. R. Holdsworth: Creep and Fracture in High Temperature Components; DEStech Publ. Inc, Lancaster. Penn., USA, (**2009**), 177–188

[21] M. YaguchiT. Ogata, T. Sakai: Creep strength of High Chromium Steels Welded Parts under Multiaxial Stress Conditions; I. A. Shibli, S. R. Holdsworth: Creep and Fracture in High Temperature Components; DEStech Publ. Inc, Lancaster. Penn., USA, (**2009**), 215–226

[22] M. Tabuchi, H. Hongo, K. Sawada, Y. Takahashi: Effect of Boron on Creep Strength of High Cr Steel Welds; I. A. Shibli, S. R. Holdsworth: Creep and Fracture in High Temperature Components; DEStech Publ. Inc, Lancaster. Penn., USA, (**2009**), 227–237

[23] P. Mayr, F. Mendez Martin, M. Albu, H. Cerjak: Correletion of Creep Strength and Microstructural Evolution of a Boron Alloyed 9Cr3WCoVNb Steel in as Received and Welded Conditions; I.A. Shibli, S.R. Holdsworth: Creep and Fracture in High Temperature Components; DEStech Publ. Inc, Lancaster. Penn., USA, (**2009**), 1029–1037

[24] Y. Hasegawa, M. Sugiyama, K. Kawakami: Type IV Damage Mechanism Due to the Microstructure Weakening in the HAZ of a Multi-Layer Welded Joint of the W Contaning 9 % Ferritic Creep Resistant Steel; I. A. Shibli, S.R. Holdsworth: Creep and Fracture in High Temperature Components; DEStech Publ. Inc, Lancaster. Penn., USA, (**2009**), 995–1006

[25] J. Kasl, D. Landova, V, Kanta: Developmentof Microstructure of Weld Joint of P 91 Steel After Creep Testing; I. A. Shibli, S. R. Holdsworth: Creep and Fracture in High Temperature Components; DEStech Publ. Inc, Lancaster. Penn., USA, (**2009**), 1007–1016

[26] S. Yamada, M. Yaguchi, Z. Ogata: Observation of Microstructural Change in Creep Damaged 9 % and 12 % Cr Steel Welded Joints; I. A. Shibli, S. R. Holdsworth: Creep and Fracture in High Temperature Components; DEStech Publ. Inc, Lancaster. Penn., USA, (**2009**), 1058–1066

[27] S. Kamazaki, T. Kato, T. Nakata, A. Gatsenko, Y. Kohno: Small Punch Creep Properies of Welded Joint of High Cr Ferritic Steel; I. A. Shibli, S. R. Holdsworth: Creep and Fracture in High Temperature Components; DEStech Publ. Inc, Lancaster. Penn., USA, (**2009**), 1102–1112

[27] K. Kubushiro, H. Yoshikawa: Creep Life Evaluation of Low-alloy Steel Weldments by Small Punch Method; I. A. Shibli, S. R. Holdsworth: Creep and Fracture in High Temperature Components; DEStech Publ. Inc, Lancaster. Penn., USA, (**2009**), 1113–1117

[28] M.F. Asby: Proc. Sec. Int. Conf. On Strength of Metals and Alloys, (**1970**), Am. Soc. Metals, ASM, Metals Park, Ohio, Ca, 507. Loc. Cit. ref. 30

[29] E. Hornbogen: Einfluss von Teilchen einer zweiter Phase aus das Zeitverhalten; W. Dahl, W. Pitch: Festigkeits- und Bruchverhalten bei höheren Temperaturen, Verl. Stahleisen, Düsseldorf, (**1980**), 31–52

[30] E. Artz, J. Rösler: Acta metal., 36 (**1988**), 1053–1060

[31] J. Rösler, E. Artz: Acta metal., 38 (**1990**), 671–683

[32] D. A. Skobir, F. Vodopivec, L. Kosec, M. Jenko, J. Vojvodič - Tuma: Steel Res. Intern. 75 (**2004**), 196–202

[33] F. Vodopivec, D. A. Skobir, B. Žužek, M. Jenko: Coarsening rate of carbide particles in a 0.18C11.5Cr0.27V steel; Article in preparation

[34] J. W. Martin, R. D. Doherty, B. Cantor: Stability of microstructure in metallic systems; Cambridge Univ. Press, (**1997**), 257

[35] F. Vodopivec, B. Ule, J. Žvokelj: O deformacijski sposobnosti jekel po uporabi v visokotlačnem parnem kotlu (On the deformation resistance of steel after use in high pressure stem boiler); Kovine Zlit. Tehnol., 31 (**1997**), 361–366

[36] F. Vodopivec, J. Vojvodič - Tuma, B. Šuštaršič, R. Celin, M. Jenko: Mater. Sci. Techn., DOI 10.1179/026708310X 12688283410325

[37] G. Eggeler: Acta metal., 37 (**1989**), 3225–3234

[38] A. Kostka, K. G. Tak, R. J. Helmig, Y. Estrim, G. Eggeler: Acta Mater., 55 (**2007**), 539–550

[39] A. Aghajani, Ch. Somsen, G. Eggeler: Acta Mater., 57 (**2009**), 5093–5106

[40] M. Taneike, M. Kondo, T. Morimoto: ISIJ Intern., 41 (**2001**), 111–S 115

[41] K. Maruyama: Fundamental aspects of creep deformation and deformation mechanism map; Ed. F. Abe, T-U. Kern, R. Viswanathan: Creep resistant steels, Woodhead Publ. LTD., Cambridge, England, (**2008**), 265–278

[42] J. Vojvodič - Tuma, R. Celin, D. Kmetič, B. Arzenšek, F. Vodopivec: Evolution of microstructure and properties of welds in thermal power installations operating at the highest temperature; Report NCRI 377/2007, Institute of Metals and Technology, Ljubljana, Slovenia

EFFECT OF THE MARTENSITE VOLUME FRACTION ON THE MACHINING OF A DUAL-PHASE STEEL USING A MILLING OPERATION

VPLIV VOLUMENSKEGA DELEŽA MARTENZITA NA OBDELAVO DVOFAZNEGA DUALNEGA JEKLA Z REZKANJEM

Okan Topçu[1], Mustafa Übeyli[2], Adem Acir[3]

[1]TOBB University of Economics and Technology, Mechanical Engineering, 06560 Ankara - Turkey
[2]Osmaniye Korkut Ata University, Mechanical Engineering, 80000 Osmaniye – Turkey
[3]Gazi University, Mechanical Education, Teknikokullar, 06560 Ankara - Turkey
mubeyli@etu.edu.tr

Dual-phase steels are attractive because of their good combination of strength and ductility. However, an increase in the martensite content will decrease the steel's machinability significantly. Therefore, optimum cutting parameters in the machining of such materials should be determined. In this paper, the machinability of a low-alloy steel having various martensite volume fractions was investigated. The four groups of samples, three of which were intercritically annealed at three different temperatures and one of which was normalized, were used. Then, the machining experiments were carried out using a face-milling operation with two different tools. After that, the flank wear on the tools with respect to the chip-volume or flank-wear limit was determined for each case. Next, the surface roughness of the samples was measured. Finally, the wear behavior of the tools was examined with a scanning electron microscope (SEM). The experimental results indicated that the flank wear of the tools increased dramatically with the increasing martensite content of the dual-phase steels.

Keywords: dual phase steel; machinability; tool wear; milling.

Dvofazno dualno jeklo se odlikuje po dobri kombinaciji trdnosti in duktilnosti. Pri povečanju vsebnosti martenzita se obdelovalnost pomembno zmanjša, zato je treba za jeklo določiti optimalne pogoje rezanja. V tem delu je bila raziskana obdelovalnost malolegiranega jekla z različnim volumenskim deležem martenzita. Uporabljene so bile štiri skupine vzorcev, tri izmed njih so bile interkritično žarjene pri treh različnih temperaturah, ena pa je bila samo normalizirana. Obdelovalni preizkusi so bili izvršeni s čelnim rezkanjem z dvema različnima orodjema. Nato je bila za vsak primer določena čelna obraba orodij glede na prostornino ostružkov ali mejna vrednost čelne obrabe in tudi hrapavost površine obdelancev. Obrabno vedenje orodij je bilo raziskano z vrstičnim elektronskim mikroskopom (SEM). Poskusi so pokazali, da čelna obraba orodij dramatično raste z vsebnostjo martenzita v dualnem jeklu.

Ključne besede: dvofazno dualno jeklo, obdelovalnost, obraba orodij, rezkanje

1 INTRODUCTION

Making a dual-phase microstructure in a low-carbon and/or alloyed steel provides not only a high strength but also a good formability and yielding without serrations [1–7]. In this type of microstructure, soft ferrite and hard martensite phases are present and maintain the ductility and the strength of the steel. The improvement in the mechanical properties via forming a dual-phase microstructure in the steel supplies the benefit of reducing the weight of systems. The studies on dual-phase steels have been focused generally on the microstructural and mechanical characterizations after intercritical heat-treatment applications [1–17]. On the other hand, the machinability of these materials is also very important, particularly with respect to the martensite fraction. Optimum cutting parameters in machining should be determined for dual-phase steels with respect to the martensite fraction and the tool types. This knowledge would be very helpful for accelerating the machining process and extending the tool life. In the literature, the studies on the machinability of dual-phase steels are very scarce [18–20].

Therefore, the machinability of these materials still needs to be investigated in detail. El-Gizawy [18] carried out a study on the machining characteristics of a high-strength, low-alloy steel with 80 % martensite and 20 % ferrite using a face-milling operation in which high-speed steel tools were used. It was concluded that the steel with ferrite and martensite showed superior chip disposability compared to that with ferrite and pearlite [18]. In addition, Sueyoshi and Tanaka [19] examined the machinability of a tri-phase steel having the microstructure of ferrite, martensite and graphite and compared the results with a dual-phase steel containing ferrite and martensite phases. They found that the drillability of the tri-phase steel was better than the dual-phase one. In another study [20], tool wear and chip disposability in the machining of a tri-phase steel were investigated and the results compared with those of the dual-phase steel. It was stated that the tri-phase steel provided better chip-disposal behavior due to the fine graphite nodules. Furthermore, the flank wear for the tri-phase steel was found to be lower than that for the dual-phase steel at low cutting speeds with high-speed steel tool.

In this paper, the machinability of a low-carbon, low-alloyed steel in a milling operation was presented. The main aim was to determine the effect of the martensite volume fraction and the cutting speed on the flank wear of coated and uncoated tools.

2 MATERIALS AND METHODS

The steel was supplied as a hot-rolled billet from a private steel company in Turkey. Its composition was 0.28 % C, 1.45 % Mn, 0.21 % Cr, 0.20 % Si, 0.13 % V, 0.01 % Nb and (bal) Fe in terms of mass fractions (%). The specimens were prepared as square shapes of size (100 × 100 × 10) mm. Next, the intercritical heat treatments at (737, 754 and 779) °C were applied to these steel specimens to obtain three different martensite volume fractions. These temperatures were utilized in our previous study [16] and corresponded to low, medium and high martensite volume fractions (approximately 30 %, 50 % and 80 %) in the steel. In addition, the normalizing treatment at 900 °C was also performed for one group of specimens to obtain a fine ferrite and pearlite microstructure to compare with the intercritically treated specimens. The details of the heat-treatment procedures of this steel can be found in Ref. [16]. In total, four different specimen groups, according to their microstructures, were formed. After finishing the thermal treatment procedures, the martensite volume fractions in the intercritically heat-treated samples were checked using an image-processing computer program. Furthermore, the macro-hardness of all the samples was measured by applying the Rockwell C test [21]. Finally, the face-milling experiments were carried out on a CNC vertical machining center (Johnford VMC-550 Fanuc Series O-M) in dry conditions (**Figure 1**). Two different types of tools, of which the properties are given in **Table 1**, were used in the face milling of the steel specimens. The tool geometr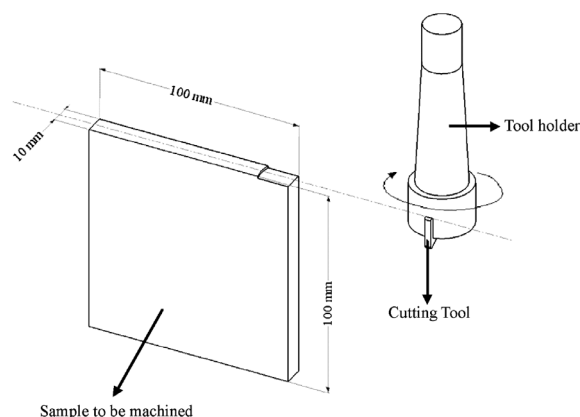y and the cutting conditions are also described in **Table 2**. The three different cutting speeds (100, 160 and 220) m/min were used in the operations while the feed was kept constant (0.2 mm per tooth). The milling operations were performed until a chip volume of 8000 mm^3 or a flank wear limit (V_B) of 0.3 mm was reached. Furthermore, the surface roughness of the machined samples was measured using a surface-roughness measurement device, i.e., a Perthometer M1 (Mahr). The microscopic observations on the tool inserts were made with the help of a scanning electron microscope (SEM) and an optical microscope to see their wear behavior clearly.

Table 1: Cutting-tool type and characteristics used in the experiment
Tabela 1: Tip rezalnega orodja, ki je bilo uporabljeno pri poskusih

Tool name	Cutting tool designation	Substrate and coating	Coating technique	Depth of cut (DOC) h/mm
Tool A	TPMN160308	K20 (no coating)	Uncoated	1.0
Tool B	TPMN160308	F620 + TiN coating	CVD	1.0

Table 2: Tool geometry and cutting conditions
Tabela 2: Geometrija orodja in pogoji rezanja

Cutting conditions	Parameters
Clamping type of tool holder	Collet
Tool holder diameter [mm]	32
Rake angle	0°
Relief angle	11°
Insert angle	60°
Cutting length, l/mm	100
Number of tooth	Single
Approach angle	90°
Nose radius, r/mm	0.8
Cutting speed, v/(m/min)	100, 160, 220
Feed per tooth [mm per tooth]	0.2
Axial depth of cut, h_a/mm	1
Radius depth of cut, h_r/mm	10

3 RESULTS AND DISCUSSION

Figure 2 shows typical microstructures of the samples with different thermal treatment histories. The martensite volume fractions of samples, treated intercritically at (737, 754 and 779) °C, were approximately (30, 50 and 80) %, respectively. The hardness was recorded to be (30, 35 and 40) HRC for the same samples, successively. The lowest hardness value belonged to the normalized specimen, which was 20 HRC. **Figure 3** depicts the change in the flank wear of both types of tools at the cutting speed of 100/min in the milling of four group specimens. It can be seen from this figure that an increase in the hardness of the dual-phase samples accelerated the wear of both types of tools. Although the performances of both tools were similar for the milling of the high martensitic samples (40 HRC), the uncoated tool had the lower flank-wear values for the milling of the low and medium martensitic samples. On
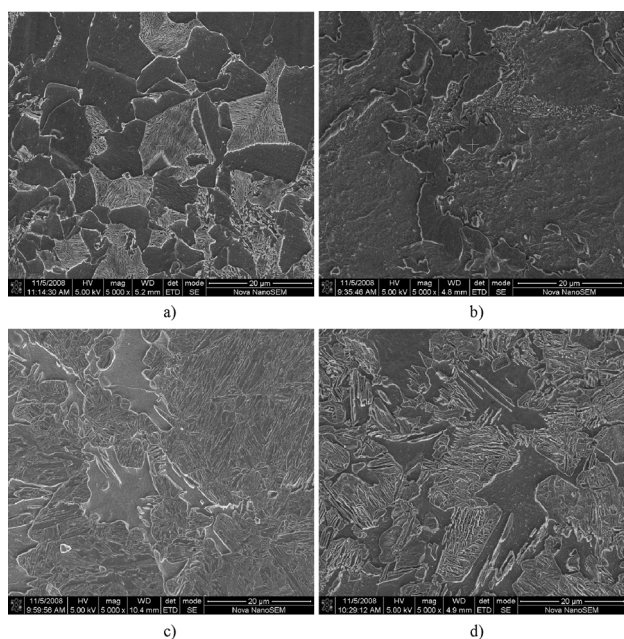

Figure 1: Schematic view of the face-milling operation. In one pass the tool moves from one end to the other end of sample at a certain cutting speed.
Slika 1: Shematičen pogled na proces čelnega rezkanja. V enem koraku se orodje pri določeni hitrosti rezanja premakne iz enega na drugi konec vzorca.

Figure 2: Typical microstructures of the steel samples a) normalized, b) intercritically annealed at 737 °C, c) intercritically annealed at 754 °C, d) intercritically annealed at 779 °C

Slika 2: Tipične mikrostrukture vzorcev jekla: a) normalizirano, b) interkritično žarjeno pri 737 °C, c) interkritično žarjeno pri 754 °C, d) interkritično žarjeno pri 779 °C

the other hand, the normalized and the low martensitic dual-phase samples led to a similar flank wear on Tool A (uncoated). In addition, the Tool B (coated) failed at the beginning of the milling of the normalized specimen (20 HRC) due to the excessive formation of a built-up edge (BUE).

The variation in the flank wear for the tools with respect to the chip volume at the cutting speed of 160
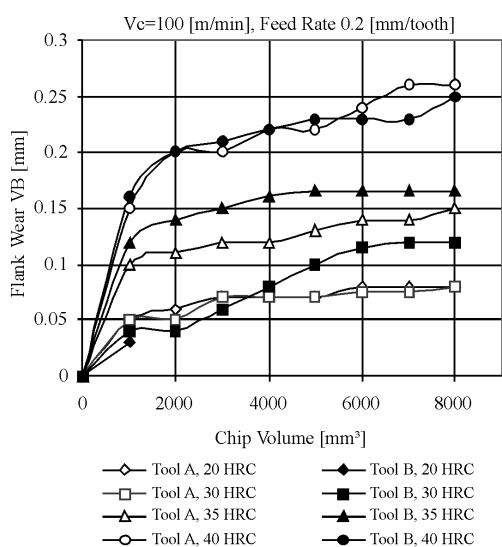
Figure 3: Flank wear on the tools at the cutting speed of 100 m/min in the milling of the investigated samples

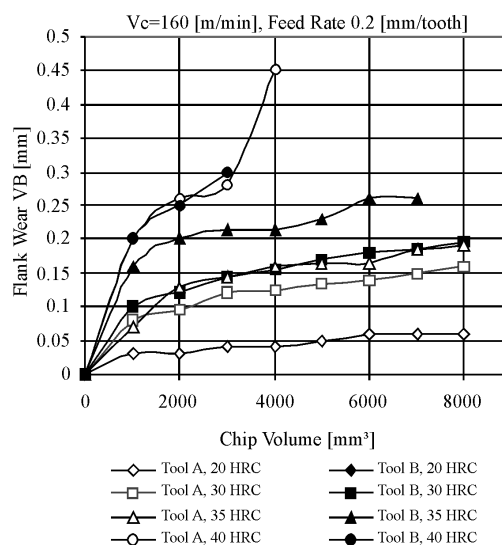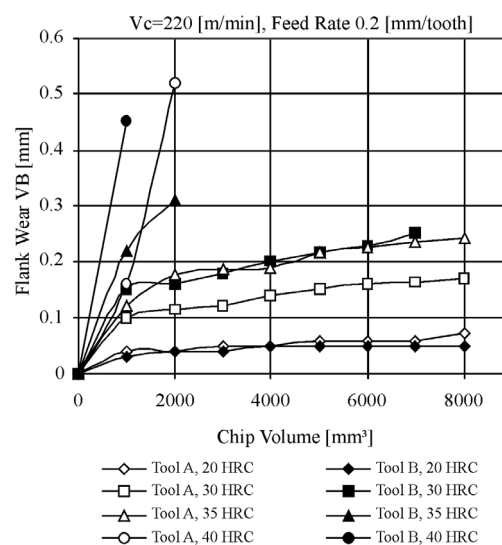**Slika 3:** Čelna obraba orodij pri hitrosti rezanja 100 m/min pri rezkanju preiskanih vzorcev

Figure 4: Flank wear on the tools at the cutting speed of 160 m/min in the milling of the investigated samples.

Slika 4: Čelna obraba orodij pri hitrosti rezanja 160 m/min pri rezkanju preiskanih vzorcev

Figure 5: Flank wear on the tools at the cutting speed of 220 m/min in the milling of the investigated samples.

Slika 5: Čelna obraba orodij pri hitrosti rezanja 220 m/min pri rezkanju preiskanih vzorcev

m/min is illustrated in **Figure 4**. When the high martensitic sample was machined, the flank wear increased very rapidly on both tools. It exceeded the limit when the chip volume of 3000 mm³ was removed from the samples. It is interesting to note that in the machining of the low and medium martensitic samples, the Tool A had lower flank-wear values than the Tool B. Tool B (coated) was fractured at the beginning of the milling process of the normalized sample again so the data was missed for this case. Furthermore, it also failed in the milling of the dual-phase sample with 35 HRC after a chip volume of 7000 mm³ was removed.
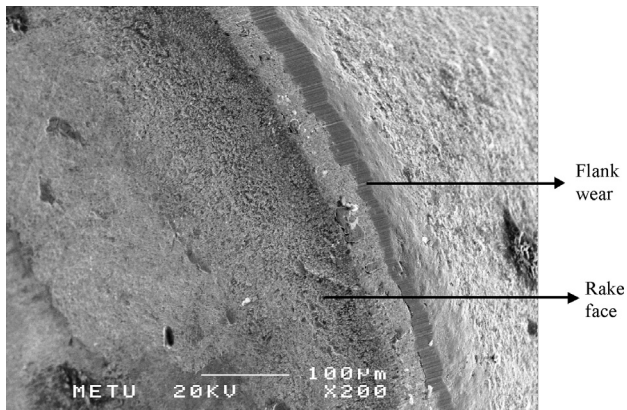
Figure 6: Typical SEM view of the flank wear on Tool A after machining of the normalized specimen at the cutting speed of 160 m/min.

Slika 6: Tipična SEM-slika čelne obrabe orodja A po obdelavi normaliziranega vzorca pri hitrosti rezanja 160 m/min

Figure 5 presents the tool-wear behavior versus chip volume during the milling of the investigated samples at a cutting speed of 220 m/min. The effect of the sample hardness on the flank wear of the tools was clearly seen. Increasing the cutting speed of the tool caused faster tool wear in all cases. Tool B exceeded the flank-wear limit for the dual-phase samples with 35 HRC and 40 HRC before removing the chip volume of 2000 mm^3. Furthermore, Tool B fractured after having seven passes over the dual-phase sample having 30 HRC. At the cutting speed
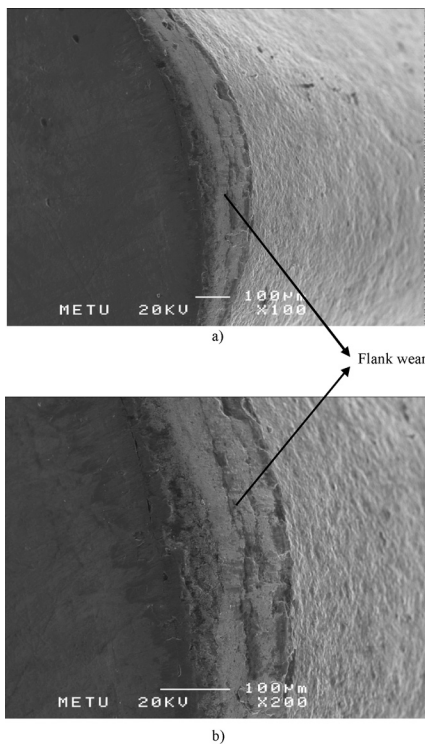

Figure 7: View of Tool B after machining of the low martensitic dual-phase steel a) X100, b) X200

Slika 7: Videz orodja B po obdelavi jekla z malo martenzita; a) povečava 100-kratna, b) 200-kratna
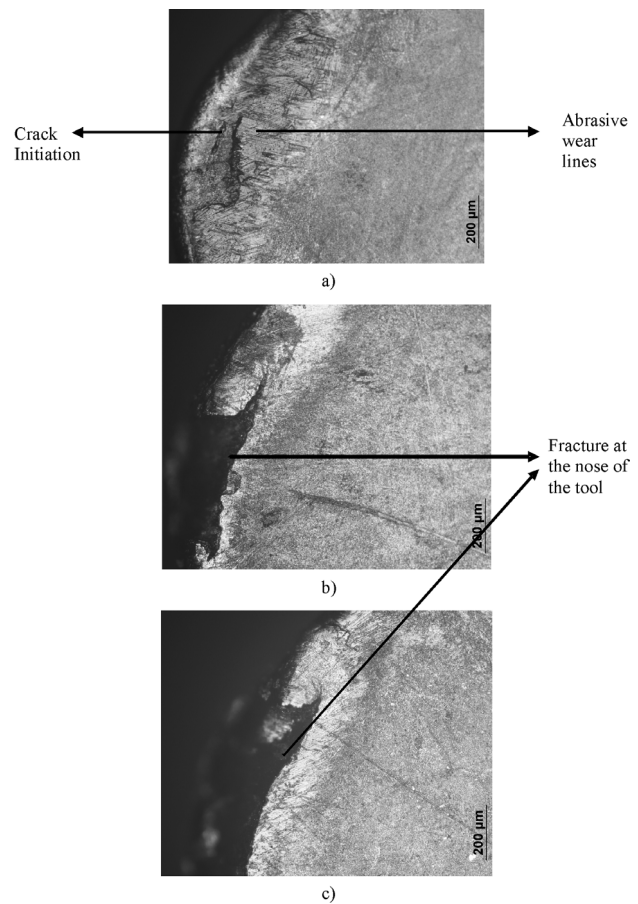

Figure 8: A typical failure of the coated tool after milling: a) the normalized specimen, b) the dual-phase specimen with 30 HRC, c) the dual-phase specimen with 40 HRC (100-times)

Slika 8: Značilna oblika poškodb prekritega orodja po rezkanju: a) normalizirani vzorec, b) dualno jeklo s trdoto 30 HRC, c) dualno jeklo s trdoto 40 HRC (pov. 100-kratna)

of 220 m/min, the normalized specimen was machined by both tools without causing any fracture. **Figures 6 and 7** show a typical SEM view of the flank wear observed on the tools after machining. An increase in the cutting speed of the process increases the temperature of the cutting zone significantly. This leads to a softening of the chip and the formation of a BUE. For this reason, the removal of the BUE from the cutting tool becomes much easier. On the other hand, in the intercritically annealed samples, the hardness values are much higher than the normalized one. So that BUE formation is not so severe in these samples.

Even though the performances of both tools are close to each other at all cutting speeds in the machining of high martensitic dual-phase steel, Tool A exhibited a better performance than Tool B in the machining of other types of samples. The adhesion of the chips to the coated tool was found to a much greater extent, especially for the cutting speeds of 100 m/min and 160 m/min. Furthermore, the coating material of TiN was easily removed from the tool by an abrasive wear mechanism for the harder samples. Therefore, its protection ability was
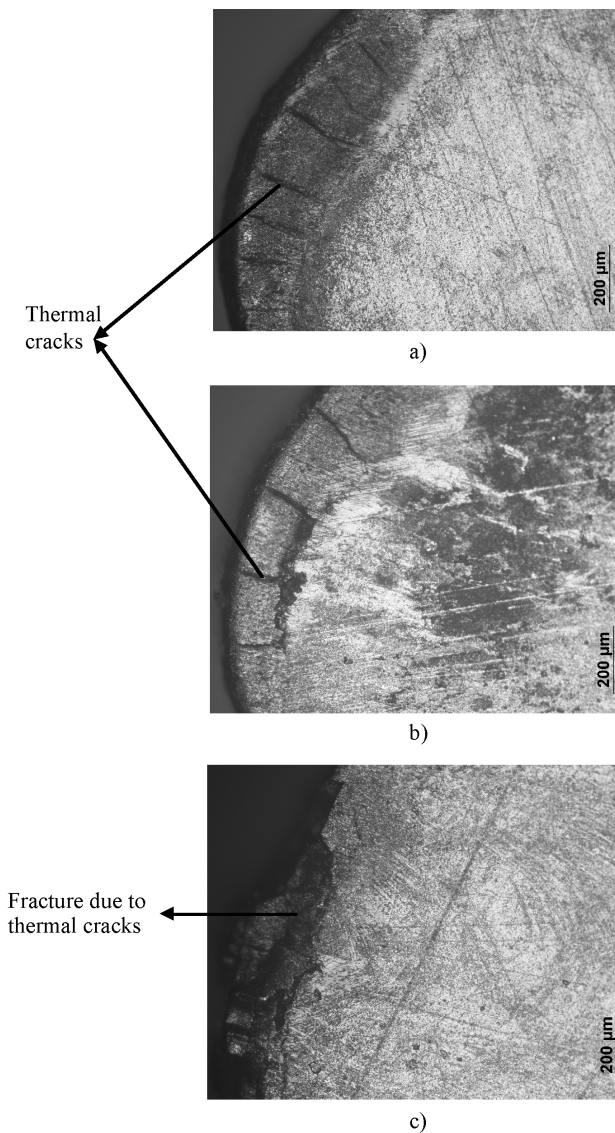
Thermal cracks

Fracture due to thermal cracks

Figure 9: A typical view of the cracks on the uncoated tool after milling the dual-phase sample with: a) 30 HRC, b) 35 HRC, c) 40 HRC (100-times)
Slika 9: Značilen videz razpok na nepokritem orodju po rezkanju dualnih vzorcev s: a) 30 HRC, b) 35 HRC, c) 40 HRC (pov. 100-kratna)

Figure 10: Surface roughness of the machined samples
Slika 10: Hrapavost površine obdelanih vzorcev

largely destroyed by the hard martensite phase in the dual-phase steels. It is generally expected that the coating material reduces the friction between the tool and the workpiece and causes lower temperatures and longer tool lifetimes. However, lower temperatures prevent the softening and effective removal of the BUE from the cutting zone. As mentioned before, higher the BUE accumulation takes place in the cutting zone, the higher the mechanical stresses form on the tool. **Figure 8** illustrates the obtained wear of Tool B after the milling of various samples. It is clear that the mechanical cracks dominate the failure mechanism for this tool. The abrasive wear caused by the chip on the rake face can be seen. On the other hand, thermal cracks were widely
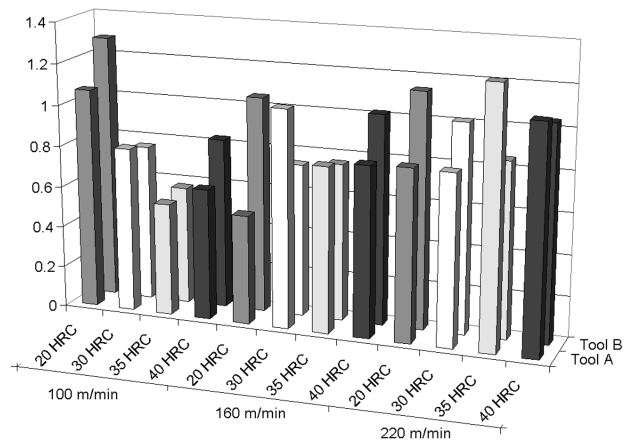
observed in Tool A, especially at the cutting speeds of 160 m/min and 220 m/min (**Figure 9**). The crater wear accelerated the fracture of Tool A significantly.

The surface roughness for the machined samples with Tools A and B is presented in **Figure 10**. It changed between 0.5 μm and 1.3 μm, depending on the cutting speed and the type of workpiece material. When the coated tool was used, the highest surface-roughness values were recorded for the normalized samples. In addition to that, there seemed to be a low tendency to increase the surface roughness of the dual-phase samples with increasing the cutting speed for the milling with either Tool A or B. The surface roughness was mainly influenced by the BUE formation.

4 CONCLUSIONS

The results of the machinability experiments for dual-phase steel using a milling operation led to the following conclusions:

- The machinability of the dual-phase steel decreased substantially with an increase in the martensite content.
- An increase in the cutting speed led to faster tool-flank wear on both the uncoated and coated tools.
- The highest BUE formation was observed on the coated tool (Tool B) in the milling of the normalized samples.
- Thermal cracks dominated the failure mechanism of the uncoated tool, whereas the mechanical cracks governed that of the coated tool.
- The surface roughness of the dual-phase samples had a tendency to slowly increase with an increasing cutting speed.

For future studies, the effect of the feed and the depth of the cut on the tool wear can be investigated to

understand the machinability of the dual-phase micro-structure in details.

5 REFERENCES

[1] J. Y. Koo, G. Thomas, Thermal cycling treatments and microstructures for improved properties of Fe-0.12 % C-0.5 % Mn steels, *Mater Sci. Eng.*, 24 (**1976**), 187

[2] Y. Tomota, K. Kuroki, T. Mori, I. Tamura, Tensile deformation of Two-Ductile-Phase Alloys: Flow curves of α-γ Fe-Cr-Ni alloys, *Mat. Sci. Eng.*, 24 (**1976**), 85

[3] R. G. Davies, The mechanical prooperties of zero-carbon ferrite-plus-martensite structures, *Met. Trans.*, 9A (**1978**), 451

[4] H. K. D. H. Bhadeshia, D. V. Edmonds, Analysis of the Mechanical Properties and Microstructure of a High-Silicon Dual -Phase Steel, *Metal Sci.*, 14 (**1980**), 41

[5] N. K. Balliger, T. Gladman, Work hardening of dual phase steels, *Metal Sci.* 15 (**1981**), 95

[6] M. Sudo, M. Higashi, H. Hori, T. Iwai, S. Kambe, Z. Shibata, Effects of microstructures on the mechanical properties of multi-phase sheet steels. *Trans. ISIJ*, 21 (**1981**), 820

[7] N. Matsumura, M. Tokizane, Microstructure and mechanical properties of dual-phase steel produced by intercritical annealing of lath martensite, *Trans. ISIJ*, 24 (**1984**), 648

[8] T. Hüper, S. Endo, N. Ishikawa, K. Osawa, Effect of volume fraction of constituent phases on the stress-strain relationship of dual phase steels, *ISIJ Int.*, 39 (**1999**), 288

[9] S. S. M. Tavares, P. D. Pedroza, J. R. Teodosio, T. Gurova, Mechanical properties of a quenched and tempered dual phase steel, *Scr. Mater.*, 40 (**1999**), 887

[10] S. Sun, M. Pugh, Properties of thermomechanically processed dual-phase steels containing fibrous martensite, *Mater. Sci. & Eng.*, A 335 (**2002**), 298

[11] J. Lis, A. K. Lis, C. Kolan, Processing and properties of C-Mn steel with dual-phase microstructure, J. Mater. Process Technol., 162–163 (**2005**), 350

[12] M. Erdogan, S. Tekeli, The effect of martensite volume fraction and particle size on tensile properties of a surface-carburized AISI 8620 steel with a dual-phase core microstructure, *Mater Charact*, 49 (**2003**), 445

[13] X. Liang, J. Li, Y-H. Peng, Effect of water quench process on mechanical properties of cold rolled dual phase steel microalloyed with niobium, *Mater Lett*, 62 (**2008**), 327

[14] Y. J. Chao, Jr. JD. Ward, R. G. Sands, Charpy impact energy, fracture toughness and ductile-brittle transition temperature of dual-phase 590 steel, *Mater Des.*, 28 (**2007**), 551

[15] M. Sarwar, T. Manzoor, E. Ahmad, N. Hussain, The role of connectivity of martensite on the tensile properties of a low alloy steel, *Mater. Des.*, 28 (**2007**), 1928

[16] O. Topçu, M. Übeyli, On the microstructure and mechanical characterisations of a low carbon and micro-alloyed steel, *Mater. Des.*, 30 (**2009**) 8, 3274

[17] O. Topçu, M. Übeyli, T. Demir, On the hardenability of an intercritically heat treated microalloyed steel, *Instr. Sci. and Tech.*, 38 (**2010**), 178

[18] A. S. El-Gizawy, Machining characteristics of dual phase steel, *Materials and Manufacturing Processes*, 5 (**1990**) 3, 377

[19] H. Sueyoshi, R. Tanaka, Heat-treatment and machinability of the tri-phase steel composed of ferrite, martensite, and graphite, *Nippon Kinzoku Gakkai-si*, 54 (**1990**) 2, 231

[20] H. Sueyoshi, H. Tanaka, K. Suenaga, R. Tanaka R., Tool wear and chip-disposability in the cutting of the tri-phase steel composed of ferrite, martensite, and graphite, *Nippon Kinzoku Gakkai-si*, 54 (**1990**) 5, 589

[21] ASTM Standards, Designation E 18-93, Standard test methods for Rockwell hardness and Rockwell superficial hardness of metallic materials; 1993

DEGRADATION OF A Ni-Cr-Fe ALLOY IN A PRESSURISED-WATER NUCLEAR POWER PLANT

DEGRADACIJA ZLITIN Ni-Cr-Fe V TLAČNOVODNIH JEDRSKIH ELEKTRARNAH

Roman Celin, Franc Tehovnik

Institute of metals and technology, Lepi pot 11, 1000 Ljubljana, Slovenia
roman.celin@imt.si

In the early days of pressurized-water nuclear-power-plant design Ni-based alloys were selected because of their good mechanical properties and corrosion resistance. Alloy 600 was used for some reactor-coolant pressure-boundary components and Alloy 82/182 was used for welds. Industrial experience in the past three decades has shown that Alloy 600 components and Alloy 82/182 welds are susceptible to primary-water stress-corrosion cracking (PWSCC). PWSCC is the intergranular or transgranular cracking due to the combined action of stresses, temperatures and components in contact with the primary water (reactor coolant). PWSCC leaks and cracks were detected on the reactor-coolant pressure-boundary components. In this work some characteristics of the Alloy 600 and Alloy 82/182 welds and their PWSCC degradation are presented.

Key words: Ni-Cr-Fe alloy, stress corrosion cracking, nuclear power plant, repair

V začetni fazi konstruiranja tlačnovodnih jedrskih elektrarn so bile zaradi dobrih mehanskih lastnosti in korozijske odpornosti izbrane zlitine na osnovi Ni. Za nekatere komponente na tlačni meji reaktorskega hladila je bila izbrana zlitina z oznako Alloy 600, za zavarjene spoje pa zlitini z oznako Alloy 82/182. Izkušnje industrije z uporabo zlitine Alloy 600 in Alloy 82/182 v zadnjih treh desetletjih pa so pokazale, da so le-te občutljive za napetostno korozijsko pokanje. Napetostno korozijsko pokanje je pojav interkristalnih ali transkristalnih razpok, ki nastanejo zaradi skupnega vpliva napetosti, temperature in stika komponente z reaktorskim hladilom. Zaradi napetostnega korozijskega pokanja so bile na komponentah tlačne meje reaktorskega hladila odkrite razpoke in netesna mesta. Namen prispevka je predstavitev lastnosti zlitin Alloy 600 in Alloy 82/182, njihova uporaba v jedrskih elektrarnah ter napetostno korozijsko pokanje.

Ključne besede: zlitina Ni-Cr-Fe, napetostno korozijsko pokanje, jedrska elektrarna, popravilo

1 INTRODUCTION

Alloy 600 was originally selected for use in smaller-diameter piping penetrations in pressurized-water-reactor (PWR) nuclear plants because of its good corrosion resistance and a coefficient of thermal expansion similar to that of low-alloy steel vessels and piping material. Most of these penetrations are attached to the vessel or piping with Alloy 82 or 182 (nickel-chromium-iron) J-groove welds. Alloy 82/182 weld materials have also been used for field-butt welds.

Primary-water stress corrosion cracking (PWSCC) of Alloy 600 nozzles and Alloy 82/182 weld metal became a source of concern in non-steam generator tubing in the mid-1980s. Some significant PWSSC events in the past twenty years are listed below[1]:

- 1991 – A through wall crack leak to the top of the reactor vessel was detected during a pressure test at the nuclear power plant Bugey 3 in France.
- 2000 – Cracks were discovered in Alloy 182 welds joining the low-alloy-steel reactor vessel hot-leg nozzles to stainless-steel pipes at Ringhals 4 (Sweden) and VC Summer (United States).
- 2002 – The most severe event was the NPP Davis-Besse case. PWSSC and the significant boric acid corrosion of carbon steel material caused a serious degradation of the reactor vessel closure head.

- 2003 – A small leak was discovered on a pressurizer relief nozzle at Tsuruga 2 (Japan) due to an axial crack in the Alloy182/82 butt weld between the low-alloy-steel nozzle and the stainless-steel relief-valve pipeline.
- 2005 – Calvert Cliffs NPP (United States) identified crack indications in an Alloy 182/82 dissimilar metal weld on a 2-in. (51-mm) diameter hot-leg drain nozzle. Two axial crack indications were contained entirely within the weld and butter area.

The list of components that are known to contain Alloy 600/82/182 in at least some nuclear-power-plant designs includes:

- reactor vessel heads,
- reactor vessel hot-leg and cold-leg nozzles,
- reactor vessel bottom-mounted instrument penetrations,
- steam generator primary nozzles and tubes,
- pressurizer and heat exchangers,
- reactor coolant loop-pipe branch connections.

Some of the generic locations of Alloy 600/82/182 are shown in **Figure 1**.

The main types of affected welds are:

- J-groove welds of the control rod drive mechanism (CRDM) penetrations (**Figure 2**), reactor vessel
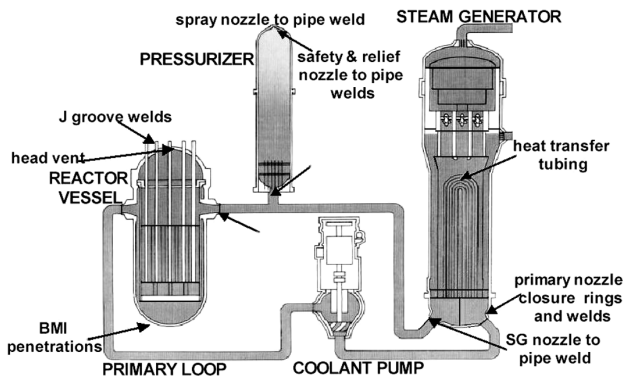
Figure 1: Generic locations of Alloy 600 components and Alloy 182/82 welds
Slika 1: Splošne lokacije komponent iz zlitine 600 in zvarov zlitin 82/182

bottom-mounted instrumentation penetrations (BMI), steam generator (SG) drain lines, pressurizer instrument nozzles and hot-leg instrument nozzles;

• butt welds or full-penetration dissimilar-metal welds of reactor pressure vessels and pressurizer nozzles (**Figure 3**).

Alloy 600

Inconel Alloy 600 with UNS N06600 or W. No. 2.4816 is a standard nickel-chromium-iron engineering material for heavy-duty applications. The limiting chemical composition[2] of the Alloy 600 is shown in **Table 1**.

Table 1: Alloy 600 chemical composition in mass fractions (w/%)
Tabela 1: Kemijska sestava Alloy 600 v masnih deležih (w/%)

Ni	Cr	Fe	C	Mn	S	Si	Cu
>72	14–17	6–10	≤0.15	≤1.0	≤0.015	≤0.5	≤0.5

Alloy 600 is a stable, austenitic solid-solution material. The high nickel content gives the alloy a good corrosion resistance in many organic and inorganic compounds. Chromium provides the resistance to sulphur compounds and the resistance in oxidizing conditions at high temperatures. The alloy can be hardened and strengthened only by cold work.
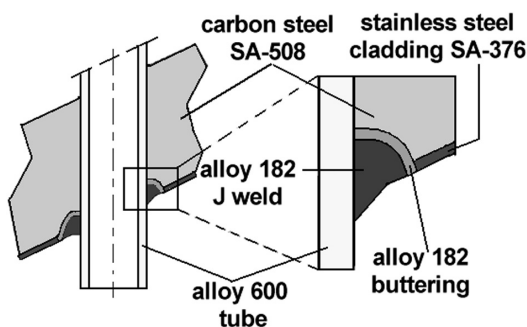

Figure 2: J-groove weld on a reactor-vessel head
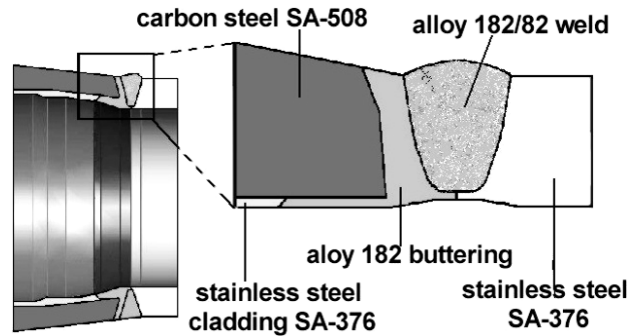**Slika 2:** J-zvar na glavi reaktorske posode

Figure 3: Nozzle-to-pipe dissimilar-metal weld
Slika 3: Zvar med cevnim nastavkom in cevovodom iz različnih materialov

The phases precipitating in the microstructure are titanium nitrides, titanium carbides and chromium carbides. The nitride particles are stable at all temperatures below the melting point and are unaffected by any heat treatment. At temperatures between 540 °C and 980 °C the chromium carbide precipitates from the solid solution at the grain boundaries and in the matrix. **Figure 4** shows the austenitic microstructure of Alloy 600 with carbide particles visible in the polished and etched metallographic specimen.

Alloy 600 components can be fabricated by press forging, hammer forging, hot rolling, forming and machining from a bar product (ASME II SB-166) or cold drawing and hot finishing from a pipe and tube product (ASME II SB-167).[2] The typical mechanical properties[3] for various forms and conditions are listed, for information only, in **Table 2**.

The alloy's strength and oxidation resistance at high temperatures make it useful for many applications for
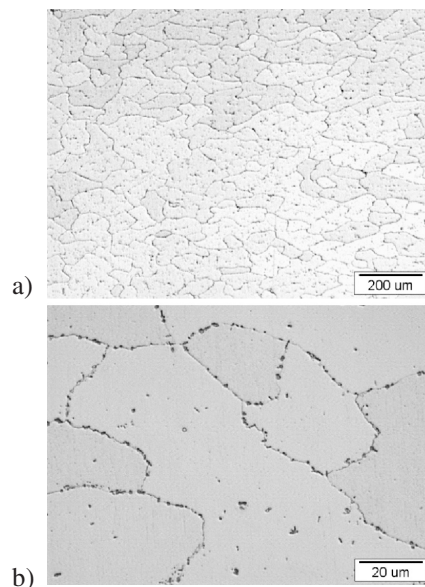

Figure 4: Alloy 600 austenitic microstructure (a) with chromium carbide particles at the grain boundaries (b)
Slika 4: Avstenitna mikrostruktura zlitine 600 (ao) z zrni kromovega karbida na mejah kristalnih zrn (b)

Table 2: Mechanical properties of Alloy 600 (for information only)
Tabela 2: Mehanske lastnosti zlitine 600 (samo za informacijo)

Product Form	Condition	Tensile strength (MPa)	Yield strength (MPa)	Elongation (%)
Rod and Bar				
Cold drawn	Annealed	550–690	170–345	55–35
	As drawn	724–1034	550–860	30–10
Hot finished	Annealed	552–689	205–345	55–35
	Hot finished	586–827	240–620	50–30
Plate				
Hot rolled	Annealed	55–725	205–345	55–35
	As rolled	580–760	240–450	50–30
Tube and Pipe				
Hot finished	Hot finished	520–690	170–345	55–35
	Annealed	520–690	170–345	55–35
Cold drawn	Annealed	550–690	170–345	55–35

furnace components in the heat-treatment industry. In the aeronautical industry Alloy 600 is used for a variety of engine and airframe components that must withstand high temperatures, for example, exhaust liners and turbine seals.

In pressurized-water reactor (PWR) nuclear power plants, Alloy 600 has been used for steam-generator tubes, control rod drive mechanism (CRDM) nozzles, reactor vessel bottom mounted instrument (BMI) penetrations, pressurizer heater sleeves and other pressure-retaining components.

The Alloy 600 was selected for use in nuclear power plants because of:
- Its good mechanical properties, similar to those of austenitic stainless steels.
- Its good general corrosion resistance in high-temperature water environments and resistance to caustic stress-corrosion cracking better than austenitic stainless steels.
- It can be welded to carbon, low-alloy and austenitic stainless steels.
- It is a single-phase alloy requiring no post-weld heat treatment, also when submitted to post-weld heat treatments required for low-alloy steel parts to which it is welded. The resulting sensitization (decreased chromium levels at grain boundaries associated with the precipitation of chromium carbides at the boundaries) does not result in a high susceptibility to chloride attack exhibited by austenitic stainless steels exposed to such heat treatments.
- Its thermal expansion properties, between those of carbon/low-alloy steels and austenitic stainless steels, make Alloy 600 a good transition metal between these steels.

2 PRIMARY-WATER STRESS-CORROSION CRACKING (PWSCC)

PWSCC is the initiation and propagation of intergranular cracks through the material in a seemingly brittle manner, with little or no plastic deformation of the bulk material and without the need for cyclic loading. Generally, it occurs at stress levels close to the yield strength of the bulk material, but does not involve significant material yielding.

An analysis of damaged components showed that PWSCC has a tendency to occur most quickly in parts which were[1]:
- fabricated from more susceptible or higher-strength materials,
- machined or cold worked prior to welding,
- installed using methods that can produce high residual stresses, such as welding or roll expansion,
- operating at high temperatures,
- not stress relieved after installation.

Over the past three decades a significant number of laboratory studies and industry events reported on the PWSCC failure mechanism for components from Alloy 600 with Alloy 182/82 welds. The results of the tests and data from industry have shown that the occurrence of the PWSCC depends on the simultaneous contribution of:
- susceptible material,
- corrosive environment (primary water (reactor coolant)),
- high stresses including residual stress and operating stress.

2.1 Material

The fabrication process, heat treatments, and chemical compositions affect the formation of the material's microstructure and are the main contributors to the PWSCC susceptibility. Alloy 600 bars, rods, plates, pipes and stripes are usually heat treated to reduce the yield strength and increase the material toughness to an acceptable level. A higher heat-treatment temperature and a longer duration result in a lower yield strength. The fabrication process, heat treatment, and chemical compositions affect the formation of the material's
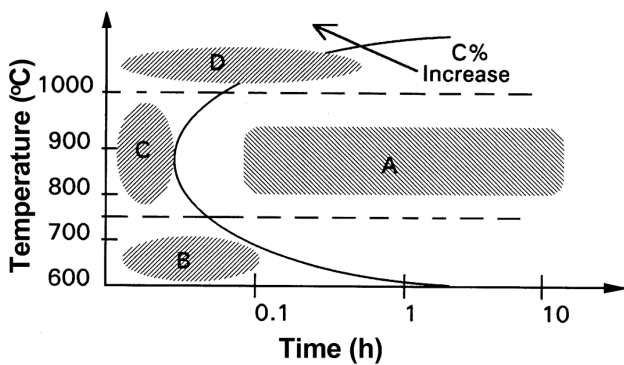
Figure 5: Carbide-precipitation diagram for Alloy 600
Slika 5: Diagram izločanja karbidov za Alloy 600

Note: 1 mil/d is $\approx 1.0 \cdot 10^{-6}$ m/h or $\approx 29 \cdot 10^{-10}$ m/s
Figure 6: Influence of hydrogen concentration on the crack growth rate of PWSCC in Alloy 600 at 338 °C
Slika 6: Vpliv koncentracije vodika na hitrost napetostnega korozijskega pokanja za zlitino 600 pri temperaturi 338 °C

microstructure and are the main contributors to the PWSCC susceptibility.

The heat-treatment temperature, annealing time and the carbon content are interrelated and affect the alloy's microstructure. A carbide-precipitation diagram for the Alloy 600 material shown in **Figure 5** could be used to assess the effect of the heat-treatment temperature and time on the microstructure.[4,5] The kinetics of precipitation depends on the velocity of the diffusion processes, which is greater at high temperature. The amount of carbide precipitates depends on the annealing time.

A high-temperature (1066 °C) heat treatment for a sufficient time (zone D in **Figure 5**) could form an intergranular carbide-particles network without the de-chromization of the area of the adjacent grain boundary. Stress-relief annealing in the range 700–800 °C in zone C in **Figure 5** also limits the intragranular carbide formation and improves the material's resistance to PWSCC. A post-fabrication heat treatment in zones B and A will result in PWSCC-susceptible material.

The mass fraction of carbon-content ($w(C)/\%$) is an important factor in the microstructure formation of Alloy 600 due to heat treatment. The lower $w(C)$ moves the x-curve of the carbide-precipitation diagram in **Figure 5** to the right and improves the conditions for intergranular carbide formation.

Generally, in Alloy 600 a good grain-boundary carbide network increases the PWSCC resistance. However, the susceptibility of Alloy 600 also depends on the surface cold work due to machining, grinding and reaming. A surface layer with a high cold work of the highly susceptible material, for example, components that were machined from bar stock and with weld root grinding, is considered to be highly PWSCC susceptible.

2.2 Environment

There are several environmental parameters that are influential on the PWSCC initiation and growth. The most significant is the primary-water temperature. The results of laboratory tests indicated that PWSCC is a
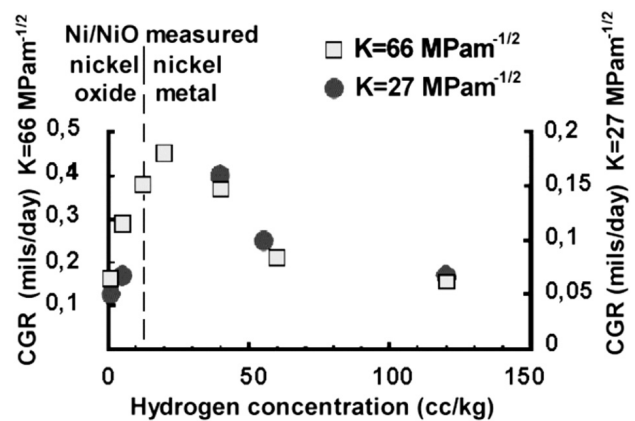
thermally activated process and that the crack initiation and growth rate are strongly temperature dependent.[6]

Like many temperature-dependent processes, the correlation between the PWSCC growth rate and the temperature can be expressed with the Arrhenius equation[7]:

$$\dot{a} = C \exp\left(-\frac{Q}{RT}\right) \qquad (1)$$

where:
$\dot{a}$ = growth rate
Q = activation energy for the crack growth phase
R = ideal gas constant
T = temperature (K)
C = constant

The other influential environmental parameters are chemical additives to the primary water. The chemistry of the primary water (reactor coolant) is maintained by the chemical and volume control system, which is designed to allow the operators to regulate the water's chemical composition. The major use of this system is to control the primary-water boron content as a function of the nuclear reactor's power level. With the addition or removal of lithium hydroxide the reactor coolant's pH value is controlled. The system is also designed to allow the addition of hydrogen during normal operation. Hydrogen gas is dissolved in the reactor coolant to scavenge all the dissolved oxygen, which may be present in the primary water. The effect of the lithium concentration and pH value on the PWSSC is minimal.[8]

Tests using crack growth rate (CGR) specimens have shown that crack growth tends to be faster when the water's electrochemical potential, depending on hydrogen concentration, is close to the potential where the Ni/NiO phase reaction occurs.[8,9] Higher or lower values of the hydrogen concentration decrease the crack growth rates (**Figure 6**).

2.3 Stress

Allowable stresses for a nuclear power plant component are specified in ASME Boiler and Pressure Vessel Code Section III. These requirements apply to operating loadings, such as internal pressure, differential thermal expansion, dead weight, and seismic loading. On the other hand, the industry design standards do not typically address residual stresses that can be induced in the parts during fabrication. These residual stresses are often much higher than the stresses in operation. In most cases the residual stresses are ignored by the standards since they are considered as secondary and self-relieving. However it is the combination of operating-condition stresses and residual stresses that lead to PWSCC.[10] For the case of penetrations attached to the reactor-vessel heads by partial penetration J-groove welds, high residual stresses are caused by the surface machining prior to installation. This machining causes a thin, strongly deformed layer on the surface, increasing the material yield and the tensile strength near the machined surface.

The second source of residual stresses in the J-groove weld is shrinkage, which occurs when welding the nozzle into the high-restraint vessel shell, pulls the nozzle wall outward. This creates yield-strength level residual-hoop stresses in the nozzle base metal and higher-strength cold-worked surface layers. These high residual-hoop stresses contribute to the initiation of axial PWSCC cracks on the cold-worked surface layer and to the subsequent growth of these axial cracks in the lower-strength nozzle base material. Residual stresses in the nozzles and welds can lead to crack initiation from the inside surface of the nozzle, opposite from the weld and from the outside surface of the nozzle near or from the surface of the J-groove weld.

Based on the industrial experience and laboratory tests data, the crack growth rate model taking into consideration the temperature dependence and stresses was developed.[11–16] The recommended crack growth rate model of detected PWSCC flaws in thick-walled Alloy 600 components exposed to the primary water is:

$$\dot{a} = \exp\left[-\frac{Q_g}{R}\left(\frac{1}{T}-\frac{1}{T_{ref}}\right)\right]\alpha(K-K_{th})^{\beta} \qquad (2)$$

where:

$\dot{a}$ = crack growth rate at temperature T/(m/s)

Q_g = 130 kJ/mole activation energy for crack growth

R = universal gas constant $8.314 \cdot 10^{-3}$ kJ/(mole K)

T = absolute operating temperature at the location of the crack

T_{ref} = absolute reference temperature used to normalize data 598.15 K

α = crack growth amplitude 2.67×10^{-12} at 325 °C

K = crack tip stress-intensity factor (MPa m$^{1/2}$)

K_{th} = crack tip stress-intensity factor threshold 9 MPa m$^{1/2}$

β = exponent 1,16

2.4 Dissimilar metal welds

The conventional welding processes can be used to produce nickel alloy joints. Some of the characteristics of nickel alloys require the use of slightly different welding techniques than normally used for stainless-steel welds.

Weld Alloys 82 and 182 have been commonly used to weld Alloy 600 to itself and to other materials. These alloys are also used for nickel-based alloy weld deposits (buttering) on weld preparations and for cladding on areas such as the insides of reactor-vessel nozzles and steam-generator tube sheets. Alloy 82 with UNS N06082 or W. Nr. 2.4806 is a bare electrode material and is used for gas tungsten arc welding (GTAW), also known as tungsten inert gas (TIG) welding. Alloy 182 with UNS W86182 or W. Nr. 2.4807 is a coated electrode material and is used in shielded metal arc welding (SMAW). The compositions of the two alloys are different[2], leading to different susceptibilities to PWSCC. Alloy 182 has a lower chromium content (13–17 %) than Alloy 82 (18–22 %) and has a higher susceptibility to PWSCC, probably as a result of the lower chromium content. A comparison between these weld metals is shown in **Table 3**.[2]

Table 3: Comparison between Alloy 182 and Alloy 82 weld metals (w/%)
Tabela 3: Primerjava kemijske sestave Alloy 82 in Alloy 182 (w/%)

	Ni	Cr	Fe	Ti	Ni + Ta	C
Alloy 182	≥59	13–17	≤10	≤1.0	1.0–2.5	≤0.1
Alloy 82	≥67	18–22	<10	≤0.75	2.0–3.0	≤0.1
	Mn	**S**	**Si**	**Cu**	**P**	**Co**
Alloy 182	5–9.5	≤0.015	≤1.0	0.5	≤0.03	≤0.12
Alloy 82	2.5–3.5	≤0.015	≤0.50	0.5	≤0.03	≤0.10

The location of dissimilar-metal welds between low carbon and austenitic steel tubing and piping are shown in **Figure 1**. Such transition joints are necessary because of the corrosion resistance of stainless steel, while low-carbon steels are commercially more appropriate.[17] For example, the reactor pressure vessel and steam
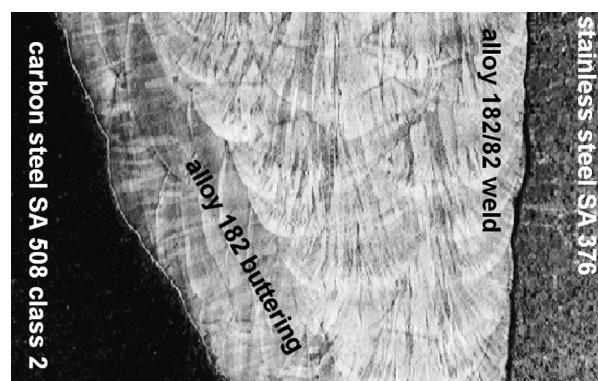

Figure 7: Dissimilar-metal weld cross-section
Slika 7: Prečni prerez zvara med različnima kovinskima materialoma

generators are made of low-carbon steels, whereas the primary piping is made of stainless steel. Therefore, to join the low-carbon steel components to stainless-steel piping Alloy 182/82 welding consumables were used (**Figure 3**). The macrostructure of a typical multiple-passes dissimilar-metal weld is shown in **Figure 7**.

A distinguished columnar pattern of dendrites can be seen through many weld passes. The dendrites, growing in the opposite direction to the heat flow, tend to be perpendicular to the base material at the weld–base-material boundary and tend to become vertical (root-to-crown direction) as the weld thickness increases. The dendrites in the centre of the weld are mainly vertical.

The boundaries between these similarly oriented dendrites are called solidification subgrain boundaries (SSGBs) and tend to have low angular mismatches, as well as low energy, and are believed to form paths relatively infrequently for PWSCC only. Where different sheaves of dendrites intersect or overlap, larger angular mismatches often occur between the grains. In this case, the resulting grain boundaries, termed solidification grain boundaries, can be high energy and are believed to be more common paths for PWSCC.

The EPRI study[18] concluded that PWSCC crack growth rates for the alloy 82/182 weld metal behave in accordance with the following relationship:

$$\dot{a} = \exp\left[-\frac{Q_g}{R}\left(\frac{1}{T} - \frac{1}{T_{ref}}\right)\right]\alpha f_{alloy} f_{orient} K^{\beta} \qquad (3)$$

where:

$\dot{a}$ = crack growth rate at temperature T in m/s

Q_g = 130 kJ/mole activation energy for crack growth

R = universal gas constant 8.314×10^{-3} kJ/(mole K)

T = absolute operating temperature at location of crack, K

T_{ref} = absolute reference temperature used to normalize data 598.15 K

α = power law constant 1.5×10^{-12} at 325 °C (598,15 K)

f_{alloy} = 1.0 for Alloy 182 and 0.385 for Alloy 82

f_{orient} = 1.0 except 0.5 for crack propagation that is clearly perpendicular to the dendrite solidification direction

K = crack tip stress-intensity factor (MPa m$^{1/2}$)

β = exponent 1.6

3 MITIGATION, REPAIR AND REPLACEMENT

3.1 Mitigation

Since PWSCC became a serious issue a number of techniques have been evaluated to delay or mitigate the occurrence of degradation processes. These techniques can be divided into three categories[19]:
1. Mechanical surface enhancement (MSE),
2. Environmental barriers or coatings,
3. Chemical or electrochemical corrosion potential (ECP) control.

MSE techniques represent processes that reduce surface tensile residual stresses or induce compressive surface stresses on a component or weld surface. Examples of MSE techniques are shot peening and electro-polishing. Environmental barrier or coating techniques represent processes that protect the material surface in aggressive environments. Coating examples include nickel plating and weld-deposit overlays. Chemical or ECP control techniques represent changes to the environment that alter the corrosion process or produce corrosion potentials outside the critical range for PWSCC. Examples of chemical or ECP control include zinc additions to the primary water and modified primary-water chemistry (e.g., dissolved hydrogen levels, lithium concentrations, and boron concentrations). In some nuclear power plants a component temperature reduction has also been applied.

3.2 Repair and replacement

Pressure boundary-components repair or replacement is the alternative to mitigation techniques, especially when a leakage is detected. ASME Code XI specifies that the flaws, detected during in-service inspection, must be removed or reduced to an acceptable size in accordance with Code-accepted procedures.[20] For PWSCC in Alloy 600/182/82 components, several approaches have been used, such as flaw removal, flaw embedment and weld overlay.

For relatively shallow or minor cracking, the flaws may be removed by grinding. This approach is going to eliminate flaws and return the component to ASME Code compliance. However, there will still be susceptible material exposed to the PWR environment that originally caused the cracking. Simple flaw removal is thus not meant to be a permanent solution, unless in future component replacement is planned.

One of the approaches to repair is to embed the flaw under a PWSCC-resistant material, typically Alloy 52 weld metal deposited over the susceptible Alloy 182/82
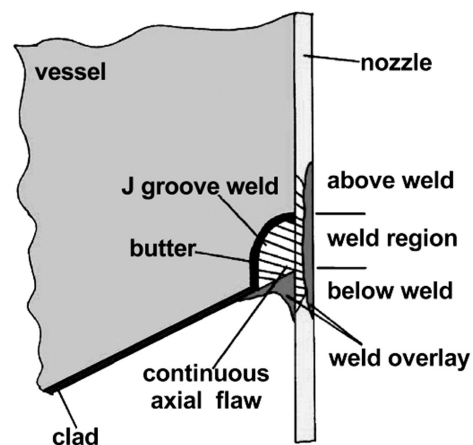

Figure 8: J groove weld-flaw embedment repair
Slika 8: Popravilo J-zvara s prekritjem napake

weld surface. The embedment must satisfy all ASME BPVC Section XI flaw-evaluation requirements.

Another form of repair that has been used extensively to repair cracked and leaking pipe welds is the weld overlay (**Figure 8**). The weld-overlay procedure has been recognized as a Code-acceptable repair in ASME Section XI.

In many cases mitigation techniques and/or repairs were successful. To satisfy Code and regulatory requirements, maintenance and inspection programs were specially developed and implemented for PWSSC-susceptible components. Additional maintenance and inspection activities mean more inspection costs for improved techniques to detect PWSCC and extra costs due to outage-time extension. The replacement of the components offers many advantages when considering the long-term operation of nuclear power plant. The new components are designed to eliminate all the susceptible materials, replacing them with PWSSC-resistant materials, such as Alloy 690 and the associated weld metals Alloys 52 and 152. The main components that have been replaced are steam generators, reactor vessel heads and pressurizers.

4 CONCLUSION

Alloy 600 component items were used in pressurized water reactors (PWRs) due to the material's inherent resistance to general corrosion in a number of aggressive environments and because it has a coefficient of thermal expansion very close to that of low-alloy steel. Over the past thirty years, primary-water stress-corrosion cracking (PWSCC) has been observed in Alloy 600 components and in Alloy 182/82 welds.

In some cases PWSSC cracks caused relatively quick and simple plugging of the leaking, small-diameter tubes in steam generators. On the other hand, many times PWSSC degradation resulted in long plant outages to replace leaking pressurizer heater sleeves, a leaking reactor-vessel hot-leg outlet nozzle weld and several CRDM nozzles. Many plants around the world have replaced their steam generators and reactor-vessel closure heads. The replacements were performed because of the high cost of repairs, the risk of leakage or the high cost of inspections necessary to ensure a satisfactory level of safety and reliability.

5 REFERENCES

[1] Materials Reliability Program PWSCC of Alloy 600 Type Materials in Non-Steam Generator Tubing Applications – Survey report through June 2002: Part 1: PWSCC in Components Other Than CRDM/CEDM Penetrations (MRP-87), EPRI, Palo Alto, CA: 2003. 1007832

[2] ASME Boiler and pressure vessel Code, Section II: Materials

[3] SMC-027, Specials Metals Corporation, 2008, www.specilasmetals.com/documents

[4] Y. S. Garud, T. L. Gerber: Intergranular stress corrosion cracking of Alloy 600 tubes in PWR primary water – Review and assessment for model development, 1983, EPRI-NP-3057

[5] G. Frederic, P. Hernalsteen, J. Stubbe, Qualification of remedial methods to prevent primary-side stress corrosion cracking of steam generator tubing: Volume 3, Global heat treatment, Final report, 1987, EPRI-NP-5249-Vol. 3

[6] R. Bandy, D. van Rooyen, Corrosion, 40 (**1983**), 425–430

[7] P. H. Hoang, A. Gangadharan, S. C. Ramalingam, Nuclear Engineering and Design, 181 (**1998**), 209–219

[8] C. Soustelle, M. Foucault, P. Combrade: PWSCC of alloy 600: a parametric study of surface film effects, Proc. of the 9th Inter. Symp. on Environmental Degradation of Materials in Nuclear Power System – Water Reactors, TMS, 1999, p. 105

[9] S. A. Attanasio, J. V. Mullen, J. W. Wuthrich, W. Wilkening, D. S. Morton: Stress corrosion crack growth rates (SCCGRs) for Alloy 182 and 82 Welds, Proc. of the Conf. on Vessel Penetration Inspection, Crack Growth and Repair, US NRC NUREG/CP-0191, 2005

[10] Companion Guide to the ASME Boiler & Pressure Vessel Code, Third Edition, Ch. 44, Jeff Gorman, Steve Hunt, Pete Riccardella, Glenn A. White, PWR reactor vessel Alloy 600 issues, 2007

[11] W. H. Bamford, J. P. Foster, Crack Growth and Microstructural Characterization of Alloy 600 PWR Vessel Head Penetration Materials, EPRI, Palo Alto, CA: 1997. TR-109136

[12] T. Cassagne, D. Caron, J. Daret, Y. Lefèvre, Stress Corrosion Crack Growth Rate Measurements in Alloys 600 and 182 in Primary Water Loops Under Constant Load, Ninth Inter. Symp. on Environmental Degradation of Materials in Nuclear Power Systems—Water Reactors Newport Beach, CA, August 1–5, 1999

[13] D. Gómez-Briceño, J. Lapeña, F. Blázquez, Crack Growth Rates in Vessel Head Penetration Materials, Proc. of the Inter. Symp. Fontevraud III: Contribution of Materials Investigation to the Resolution of Problems Encountered in Pressurized Water Reactors, Chinon, France, September 12–16, French Nuclear Energy Society, Paris, 1994, p. 209–214

[14] M. L. Castaño, D. Gómez-Briceño, M. Alvarez-de-Lara, F. Blázquez, M. S. Garcia, F. Hernández, A. Lagares, Effect of cationic resin intrusions on IGA/SCC of Alloy 600 under primary water conditions, Proc. of the Inter. Symp. Fontevraud IV: Contribution of Materials Investigation to the Resolution of Problems Encountered in Pressurized Water Reactors (France, September 14–18, 1998), French Nuclear Energy Society, Paris, 2 (**1998**), 925–937

[15] G. A. White, J. Hickling, L. K. Mathews, Crack growth rates for evaluating PWSCC of thick-wall Alloy 600 material, Proc. of the 11th Inter. Symp. on Environmental Degradation of Materials in Nuclear Power Systems-Water Reactors, NACE International, (**2003**), 166–179

[16] G. A. White, J. Hickling, C. Harrington, MRP Development of crack growth rate disposition curves for primary water stress corrosion cracking (PWSCC) of thick-section Alloy 600 components and Alloy 82, 182 and 132 Weldments, 2005 EPRI International PWSCC of Alloy 600 Conference, Santa Ana Pueblo, NM, March, 7–10, 2005

[17] M. Sireesha, V. Shankar, S. K. Albert, S. Sundaresan, Materials science and Engineering, A292 (**2000**), 74–82

[18] Materials Reliability Program, Crack growth rates for evaluating primary water stress corrosion cracking (PWSCC) of Alloy 82, 182, and 132 Welds (MRP-115NP), EPRI, Palo Alto, CA: 2004. 1006696

[19] S. Fyfitch, Alloy 600 PWSCC Mitigation: past, present, and future, Proc. of the Conf. on Vessel Penetration Inspection, Crack Growth and Repair, US NRC NUREG/CP-0191, 2005

[20] ASME Boiler and Pressure Vessel Code, Section XI: Rules for in service inspection of nuclear power plant components

INVESTIGATION INTO THE MECHANICAL PROPERTIES OF MICRO-ALLOYED AS-CAST STEEL

RAZISKAVE MEHANSKIH LASTNOSTI MIKROLEGIRANIH JEKEL

Bommannan Chokkalingam[1], S. S. Mohamed Nazirudeen[2], Sukaswami S. Ramakrishnan[3]

[1,2]Department of Metallurgical Engineering, PSG College of Technology, Coimbatore- 641 004. Tamil Nadu, India
[3]Mechanical Engineering, Karunya University, Coimbatore- 641 114. Tamil Nadu, India
bchokkalingam@gmail.com

The effects of micro-alloying on the hardness, tensile strength, room-temperature impact energy and elongation of low-carbon as-cast steel have been investigated and compared with non-micro-alloyed as-cast steel. Elements such as vanadium, niobium, titanium and zirconium were added in combination as micro-alloys. The results show that the addition of these elements in the cast steel increases the hardness and tensile strength by 31 % and 10.3 %, respectively, while the elongation and impact energy decrease to 47.5 % and 43.7 %, respectively. This method of alloying refines the microstructure of the cast steel in the as-cast form.

Key words: cast steel, micro-alloying, tensile strength, hardness, toughness

Raziskan je vpliv mikrolegiranja na trdoto, raztržno trdnost, žilavost pri sobni temperaturi in razteznost ogljikove jeklene litine in primerjan z vplivom na litino brez mikrolegiranja. Kombinacije elementov: vanadija, niobija, titana in cirkonija, so bile dodane v litino. Rezultati kažejo, da dodatek teh elementov poveča trdoto in trdnost do 31 % oz. do 10,6 % in zmanjša raztezek za 47,5 %, žilavost pa za 43,7 %. Mikrolegiranje napravi mikrostrukturo jeklene zlitine bolj drobnozrnato.

Ključne besede: jeklena litina, mikrolegiranje, raztržna trdnost, trdota, žilavost

1 INTRODUCTION

In general, based on the method of production, steels can be classified as either wrought or cast steels. Wrought steel products are shaped by plastic deformation, whereas cast steel products are produced by casting methods. Normally, both these processes are used to produce steel products. In particular, the production of intricate internal shapes and complicated designs is easier in cast steel. Moreover, economic production of fewer quantities is an added advantage of the casting process over wrought steel processes. However, the mechanical properties of cast steels are lower when compared with wrought steels. Hence, the improvement in mechanical properties is further required for cast steel due to its wide use in applications like railways, chemical plants, automobiles and petroleum refineries, etc.

Generally, the mechanical properties are improved by alloying. The different types of alloying methods are low-level, medium-level, high-level and micro-level alloying. Among these alloying techniques, micro-alloying[1,2] is one of the methods in which the alloying elements such as vanadium, niobium, titanium and zirconium are added individually up to 0.10 %. The total micro-alloying additions of all these alloying elements combined to be within 0.20 %. This method is widely practiced in wrought steel processing, whereas it is less used in cast steel. A study of the combined addition of vanadium, niobium, titanium and zirconium in cast steel was not found in the existing literature. Hence in this work, the effect of a combined addition of all these alloying elements together in the cast steel was investigated. The microstructure, hardness, tensile strength, impact energy and elongation of micro-alloyed cast steel were investigated and compared with those of non-micro-alloyed cast steel.

2 EXPERIMENTAL PROCEDURE

The melting was performed using a medium-frequency coreless induction furnace with a holding capacity of 50 kg and a basic lining. The non-micro-alloyed and micro-alloyed cast steels' chemical compositions are given in **Table 1**. The mild steel scrap was melted initially and the alloys ferro-manganese, ferro-silicon were added into the melt. The micro-alloyed cast steel composition was achieved by the addition of the necessary alloys after testing the melt using a vacuum spectrometer. The vanadium level was maintained at 0.10 %, while the niobium, titanium and zirconium additions were maintained at 0.05 %, 0.025 % and 0.025 %, respectively. The micro-alloying elements vanadium, niobium and titanium were added into the molten metal in forms of ferro-vanadium, ferro-niobium and ferro-titanium, while ferro-zirconium was added in the ladle during the tapping of the molten metal from the furnace at 1610 °C. The de-oxidisers aluminium and

Table 1: Chemical composition of experimental cast steels in mass fractions, (w/%)
Tabela 1: Kemična sestava preizkusnih jeklenih litin v masnih deležih, (w/%)

Experimental Steels	Elements in mass fractions, w/%								
	C	Si	Mn	P	S	V	Nb	Ti	Zr
Non-micro-alloyed steel (NMA)	0.23	0.42	1.20	0.02	0.03	0.0	0.0	0.0	0.0
Micro-alloyed steel (MA)	0.23	0.42	1.20	0.02	0.03	0.10	0.05	0.025	0.025

calcium silicide were added in the ladle during tapping the molten metal from the furnace. Both molten steels were poured into standard Y-block sand moulds.

The metallographic examinations were made with a light microscope using broken specimens from Charpy impact tests that were also used in the SEM and EDS analyses. These analyses were performed using a scanning electron microscope, JEOL JSM 6360, with an energy-dispersive spectroscopy (EDS) analyzer (LN2 type detector). The accelerating voltage at the time of the EDS was 25 kV, the working distance was 17mm and the probe current was 1.0 nA. The hardness was measured by using a Zwick hardness tester with an indentation load of 10 kg. The impact energy was measured with the Charpy method using standard test pieces (55 mm length, 10 mm square with V notch (45°, 2 mm deep with 0.25 mm radius at the base notch). The tensile test was performed in a Microtek tensile testing machine.

3 RESULTS AND DISCUSSION

3.1 Effects of micro-alloying elements

The purposes of adding micro-alloying elements to the cast steel are either to get fine grains or to form precipitates. The various factors contributing to the increase in hardness of the micro-alloyed cast steel are variations in the pearlite content, the ferrite grain size and the formation of fine carbonitride precipitates. Among these factors, the increase in hardness and strength is mainly due to carbonitride precipitates. Based on earlier studies[3-6], carbonitride precipitates form in the matrix, precipitate at the gamma/alpha interphase and with random precipitation.

The micro-alloying elements titanium and niobium precipitate at elevated temperatures[6-12] and generally, both elements form a precipitate in the matrix. The second and third type of carbonitrides formed when there are sufficient amounts of titanium and niobium present in the form of a solid solution in austenite during the transformation stage at the upper critical temperature.

The micro-alloying element vanadium precipitates as vanadium carbide at lower temperatures on the advancing gamma/alpha interface. It forms either as an interphase precipitate or random precipitate in the supersaturate ferritic matrix. Fine carbonitride precipitates distributed mainly in ferrite grains are very effective at strengthening. Earlier microhardness studies on ferrite grains[5-8] revealed that the increase in the strength/hardness of micro-alloyed cast steels is mainly due to

precipitation hardening, and the effect of solid-solution strengthening is lower. The solid solution of micro-alloying atoms is negligible due to the lower concentration of micro-alloying atoms after the formation of carbonitrides. The increase in the strength and hardness of vanadium micro-alloyed cast steel is due to the formation of vanadium carbonitrides V (CN)[5,6,10,12]. The increase in the amount of micro-alloying elements increases the volume fraction of the precipitates.

Zirconium is a nitride and also a strong oxide forming element. In the solid-state zirconium nitride[11,12] has a high melting point and a high hardness. The zirconium carbide forms at a higher temperature, whereas the zirconium nitride forms at a lower temperature. It was found that the zirconium addition improves the hardness and does not decrease the impact toughness. The zirconium addition causes sulfide inclusions to shape as globular rather than elongated, which improves the toughness and ductility of the micro-alloyed cast steel.

3.2 Microstructures

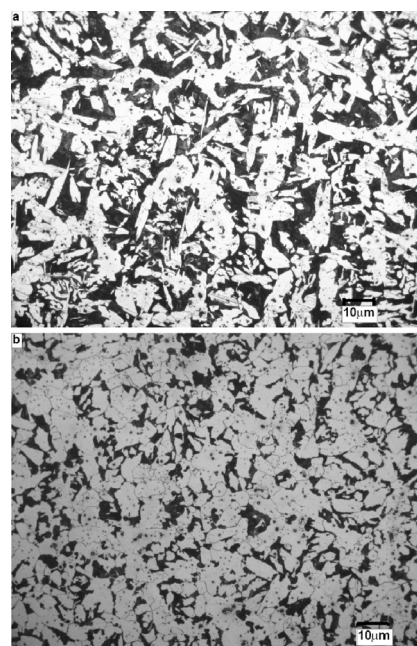The microstructure of non-micro-alloyed and micro-alloyed as-cast steels is shown in **Figure 1** (a) and (b)

Figure 1: Microstructures of cast steel a) Non-micro-alloyed (NMA), b) Micro-alloyed (MA)
Slika 1: Mikrostruktura jeklene litine a) brez mikrolegiranja (NMA), z mikrolegiranjem (MA)
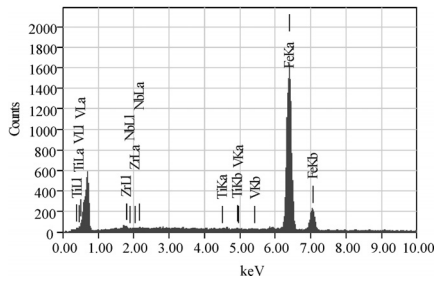
160

Figure 2: EDS analysis of micro-alloyed cast steel
Slika 2: EDS-analiza mikrolegirane jeklene litine

respectively. The microstructure in **Figure 1b** clearly shows a finer grain size in the micro-alloyed than in the non-micro-alloyed cast steel.

The EDS analysis of the micro-alloyed cast steel is shown in **Figure 2**. This analysis confirms the presence of the elements V Nb, Ti and Zr in the micro-alloyed cast steel.

3.3 Fracture surface

The fractured surfaces of all the broken impact specimens were examined using scanning electron microscopy with the aim to understand the mechanisms of the fracture of both. The fracture surfaces are shown in **Figure 3** (a) and (b). Changes were observed in the fracture with respect to the size, shape, and depth of the micro-voids, and the size and shape of the fracture facets.

The fracture appearance in **Figure 3a** is an inter-granular brittle fracture characterized by coarse facets with numerous very small solidification defects, while **Figure 3b** shows a normal brittle fracture with fine cleavage facets without solidification defects.

The causes of the intergranular fracture in the cast steel are sulphur distribution, cooling rate, larger grain size, aluminium and nitrogen contents. The various methods to control these defects are controlling the aluminium and nitrogen contents in the liquid steel, the use of vacuum melting to remove nitrogen to a low level, the addition of cerium to form stable nitrides, and grain refinement by the addition of alloying elements such as titanium, zirconium, vanadium, niobium and boron. Grain refinement is an effective method among these to reduce the intergranular fracture and solidification defects. A finer grain size was obtained by the addition of micro-alloying elements and solidification defects were also not found in the fractured surface of the micro-alloyed cast steel specimen.

3.4 Mechanical properties

The mechanical properties hardness, tensile strength, room-temperature impact energy and percentage elongation given in **Table 2** show the average properties of various test specimens at different positions. The results indicate that the addition of micro-alloying increases
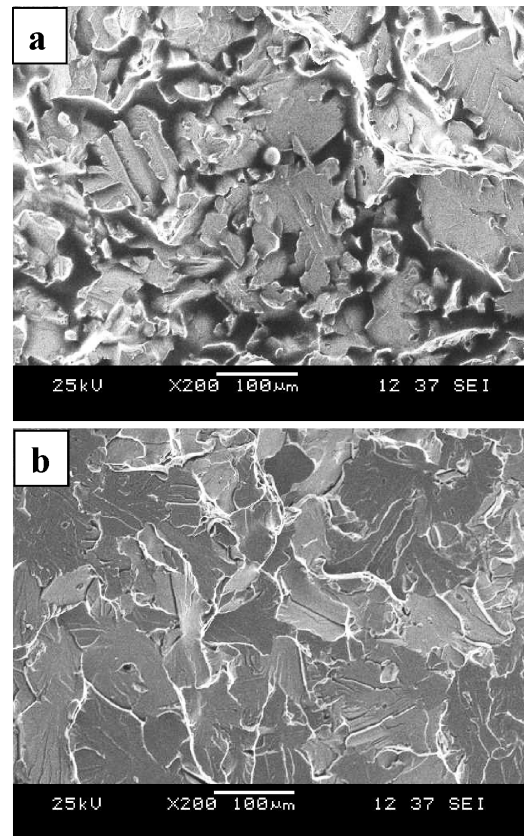

Figure 3: Fracture analysis of cast steel a) Non-micro-alloyed (NMA), b) Micro-alloyed (MA)
Slika 3: Površina preloma jeklene litine a) brez mikrolegiranja (NMA), b) z mikrolegiranjem (MA)

significantly the tensile strength and the hardness, whereas it decreases the percentage elongation and the room temperature impact toughness considerably. The increase of hardness and tensile strength to 31 % and 10.3 %, respectively, was observed in the V, Nb, Ti and Zr micro-alloyed as-cast steel compared to the non-micro-alloyed as-cast steel. The elongation and room-temperature impact toughness of the micro-alloyed as-cast steel decreases to 47.5 % and 43.7 %, respectively, compared to the non-micro-alloyed as-cast steel.

Table 2: Mechanical properties of experimental cast steels
Tabela 2: Mehanske lastnosti preizkusnih jeklenih litin

Experimental steels	Hardness, HV	UTS, MPa	Elonga-tion, %	Impact tough-ness, J
Non-micro-alloyed steel (NMA)	168	580	17	16
Micro-alloyed steel (MA	220	640	9	9

4 CONCLUSIONS

The effect of steel micro-alloying with vanadium, niobium, titanium and zirconium as micro-alloying elements on the hardness, tensile strength, percentage

elongation and room-temperature impact toughness were investigated in as-cast steel. The results obtained are: as follows

An increase in hardness to 31 % was obtained for micro-alloyed cast steel compared with non-micro-alloyed cast steel and the highest hardness of 220 HV was obtained for micro-alloyed cast steel.

The tensile strength was increased by 10.3 % in micro-alloyed cast steel when compared to non-micro-alloyed cast steel with the highest strength of 640 MPa obtained.

The elongation and the impact toughness of the micro-alloyed as-cast steel showed a decrease of 47.5 % and 43.7 %, respectively, when compared to those of the non-micro-alloyed as-cast steel.

A smaller grain size was obtained in the micro-alloyed as-cast steel.

5 REFERENCES

[1] S. Seshan: Studies on microalloyed cast steels; Proceedings of the sixth Asian foundry congress, Calcutta, (**1999**), 181–187

[2] V. Raghavan: Physical metallurgy principles and practice, 2nd ed; Prentice hall of India limited, New delhi, (**2006**), ISBN – 81-203 – 3012 – 9, 106, 193

[3] B. D. Jana, A. K.Chakrabarti, K. K. Ray: Study of cast microalloyed steels; Materials science and technology, 19 (**1993**), 80–86

[4] B. Kalandyk, H. Matysiak, J. Glownia: Microstructure strength relationship in microalloyed cast steels; Reviews on advanced material science, 8 (**2004**), 44–48

[5] H. Najafi, J. Rassizadehghani, A. Halvaaee: Mechanical properties of as cast microalloyed steels containing V, Nb and Ti; Material science and technology, 23 (**2007**), 699–705

[6] J. Rassizadehghani, H. Najafi, M. Emamy, Eslami Saeen: Mechanical properties of V, Nb and Ti bearing as cast micro alloyed steels; Journal of material science and technology, 23 (**2007**), 779–784

[7] Guang Xu, Xiaolong Gan, Guojun Ma, Feng Luo, Hang Zoe: The development of Ti alloyed high strength microalloy steel; Materials and Design, 31 (**2010**), 2891–2896

[8] D. Rasouli, Sh. Kamanah Asl, G. H. Akbar Zadeh, Daneshi: Optimization of mechanical properties of a micro alloyed steel; Materials and Design, 30 (**2008**), 2167–2172

[9] L. Bejar Gomez, A. Medina Flores, H. Carreon, I. Alfonsa, J. Bernal Ponce, J. A. Ascencio: Production and characterization of niobium and titanium microalloyed steels; Revista Maexicana De Fisica , 55 (**2009**), 110–113

[10] Hamidreza Najafi, Jafar Rassizadehghani, Siroos Asgari: As cast mechanical properties of vanadium/niobium microalloyed steels; Materials Science and Engineering A, (1–2) (**2008**), 1–7

[11] H. A. Akbarzadeh, M. Tamizifar, Sh. Mirdamadi, A. Abdolhossini: Mechanical properties and micro structures of Zr – microalloyed cast steel; ISIJ International, 45 (**2005**), 1201–1204

[12] D. A. Skobir, M. Godec, M. Balcar, M. Jenko: The influence of the microalloying elements of HSLA steel on the microstructure and mechanical properties; Mater. Tehnol., 44 (**2010**), 343–347

THE EFFECT OF ELECTROMAGNETIC STIRRING ON THE CRYSTALLIZATION OF CONCAST BILLETS

KRISTALIZACIJA KONTINUIRNO ULITIH GREDIC V ELEKTROMAGNETNEM POLJU

Karel Stransky[1], Frantisek Kavicka[1], Bohumil Sekanina[1], Josef Stetina[1], Vasilij Gontarev[2], Jana Dobrovska[3]

[1]Faculty of Mechanical Engineering, Brno University of Technology, Technicka 2, 616 69 Brno, Czech Republic
[2]University of Ljubljana, Aškerčeva 12, 1000 Ljubljana, Slovenia
[3]VSB – Technical University of Ostrava, Tr. 17. listopadu, 708 33 Ostrava, Czech Republic
stransky@fme.vutbr.cz

Electromagnetic stirring (EMS) applied on a steel caster (concasting machine) is basically a magneto-hydraulic process that influences the crystallisation processes and the solidification of billet steel. From the viewpoint of physics and chemistry, the course of the process is co-determined by a number of relevant parameters, the physical and thermokinetic characteristics of the concast steel and also the electrical and magnetic quantities. EMS suppresses the growth of columnar crystals of billets and reduces the tendency to crack during casting and at low temperatures. A caster was used for the testing of two induction stirrers – one on the actual mould and the other beneath the mould – to determine the effect of EMS on the formation of the structure of non-alloyed steel. As part of these tests, certain parts of the billets had been cast without the use of stirrers, while other parts underwent alternate switching on and off of the stirrers for as many as nine combinations of modes. Samples were taken from the sections of these billets, fine-ground and etched to make the dendritic structure visible. The mode with the highest efficiency was when both stirrers ran simultaneously. The growth of the columnar crystals, which pointed inward, was limited to ¼-to-⅓ of the width of the billet when there was no stirring. Experimental research was also confronted with the results acquired from the application of the models of the temperature field and chemical heterogeneity and the physical-similarity theory.

Keywords: concasting, electromagnetic stirring, dendritic structure, quality of billets, defects

Elektromagnetno mešanje (EMS), ki se uporablja v kontinuirnem livnem stroju, je osnovni magnetno-hidravlični proces pri spremembi kristalizacije in pri strjevanju jeklenih gredic. S stališča fizike in kemije proces določajo ustrezni parametri in materialne, fizikalne in termokinetične značilnosti kontinuirno ulitega jekla in tudi električni in magnetni vplivi. EMS preprečuje rast stebričastih kristalov v gredicah in zmanjšuje nagnjenje za tvorbo razpok med ulivanjem pri nizkih temperaturah. Livni stroj je bil uporabljen za preizkus dveh indukcijskih mešal (enega dejansko v kokili in drugega pod njo) za določitev vpliva EMS na tvorbo strukture nelegiranega jekla. Kot del teh preizkusov so bili določeni deli gredic uliti brez uporabe mešal,, drugi pa so bili izpostavljeni izmeničnemu priklopu in izklopu mešala za več kot devet kombinacij. Vzorci so bili odvzeti po prerezu gredic, dobro zbrušeni in jedkani, tako da je bila dendritna struktura vidna. Najboljši učinek je bil dosežen pri istočasnem delovanju obeh meša. Rast stebričastih kristalov, ki so bili usmerjeni v notranjost, je bila omejena na ¼ do ⅓ širine gredice, kjer ni bilo mešanja. Eksperimentalne raziskave so bile tudi primerjane z rezultati, ki so bili doseženi z uporabo modelov temperaturnega polja, kemijske heterogenosti in teorije fizikalnih podobnosti.

Ključne besede: kontinuirno ulivanje, elektromagnetno mešanje, dendritna struktura, kakovost gredic, napake

1 INTRODUCTION

Currently, casters use rotating stators of electromagnetic melt-stirring systems. These stators create a rotating magnetic induction field with an induction of B, which induces eddy-current J with velocity v in a direction perpendicular to B. The induction B and the current J create an electromagnetic force, which works on every unit of volume of steel and brings about a stirring motion in the melt. The vector product ($v \times B$) demonstrates a connection between the electromagnetic field and the flow of the melt. The speeds of the liquid steel caused by the EMS are somewhere from 0.1 m/s to 1.0 m/s. The stirring parameters are within a broad range of values, depending on the construction and technological application of the stirrer. The power output is mostly between 100 kW and 800 kW, the electric current between 300 A and 1000 A, the voltage up to 400 V and with billet casting the frequency is from 5 Hz to 50 Hz.

The EMS applied on the steel caster is basically a magneto-hydraulic process affecting the crystallisation processes and solidification of billet steel. The complexity of the entire process is enhanced further by the fact that the temperatures are higher than the casting temperatures of the concast steel. The temperature of the billet gradually decreases as it passes through the caster down to a temperature lying far below the solidus temperature. From the viewpoint of physics and chemistry, the course of the process is co-determined by a number of relevant material, physical and thermokinetic characteristics of the concast steel and also the electrical and magnetic quantities. There is also a wide range of construction and function parameters pertaining to the caster and EMS as well as the parameters relating to their mutual arrangement and synchronisation. Numerous works from recent years relate that the exact mathematical modelling of EMS on a caster is still unsolvable [1–3]. The basic EMS experiment was conduc-
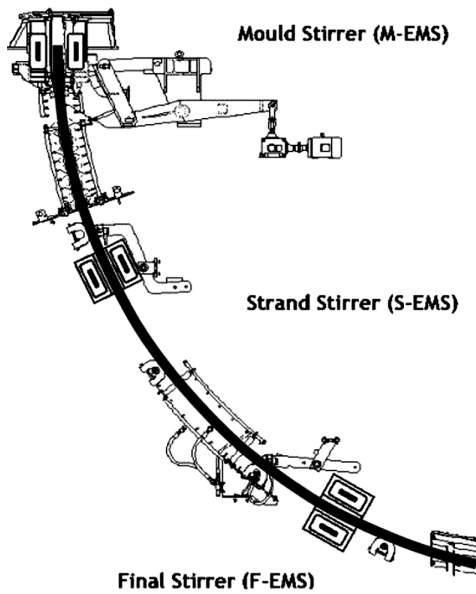
Figure 1: The positions of the MEMS and SEMS stirrers
Slika 1: Lega mešal MEMS in SEMS

ted on a CONCAST billet caster where two individual mixers were working, as in **Figure 1**. The first stirrer, entitled MEMS (Mould Electromagnetic Stirring), is mounted directly on the mould and the second stirrer, entitled SEMS (Strand Electromagnetic Stirring), is mounted at the beginning of the flow directly after the first cooling zones but in the secondary-cooling zone. Here the outer structure of the billet is already created by a compact layer of crystallites; however, in the centre of the billet there is still a significant amount of melt that is mixed by the SEMS.

2 CONDITIONS OF THE EXPERIMENT

The first stirrer (MEMS) stirs the melt still in the mould while the billet is undergoing crystallization and solidification. The second stirrer (SEMS) works at a time when the melt is already enclosed by a shell of cry-stallites around the perimeter of the billet and inside the billet there is less melt than above in the active zone of the first stirrer.

When both stirrers were switched off, the crystalli-sation and solidification continued in the normal way, i.e., the solidifying melt did not undergo a forced rotational movement.

Samples were taken throughout the course of the experiment – from parts of the billet cast using the MEMS and SEMS and without and also using either one. The samples were taken in the form of cross-sections (i.e., perpendicular to the billet axis). The samples were fine-ground and etched with the aim of making visible the dendritic structure which is characteristic for individual variants of the solidification of the billet.

The verification of the influence of MEMS and SEMS on the macrostructure of the billet was carried out

on two melts of almost the same chemical composition (**Table 1**).

Table 1: Chemical composition of experimental melts [mass fractions, *w*/%]
Tabela 1: Kemijska sestava eksperimentalne taline [masni deleži, *w*/%]

Melt	C	Mn	Si	P	S	Cu	Cr	Ni	Al	Ti
A	0.14	0.31	0.22	0.014	0.009	0.03	0.05	0.02	0.02	0.002
B	0.13	0.32	0.22	0.018	0.012	0.09	0.06	0.04	0.02	0.002

Table 2: The billet concasting modes and sampling
Tabela 2: Načini litja gredic in vzorčevanje

Melt	Concasting mode –sampling	Superheating of steel above liquidus °C	MEMS stirring A	SEMS stirring A	Fig.
A	1A	37	210	0	
	2A	31	0	0	Fig. 5
	3A	33	0	29	
	4A	30	210	57	Fig. 6
B	1B	35	210	0	
	2B	30	0	0	
	3B	27	0	57	
	4B	24	210	57	
	5B	24	210	29	

(Note: Detailed records of the experimental verification of the effects of MEMS and SEMS during concasting on the relevant device pertain to **Table 2**. The data are appended with a time history of the MEMS and SEMS connection and with information relating to the lengths of individual billets and the points from which the actual samples had been taken (i.e., the cross-sections from which the dendritic structures had been created).

The timing of the concasting process of the billets – without the involvement of the stirrers and with the working of the EMS of individual variants of stirrers (MEMS and SEMS) – is given in **Table 2**. The speed of the concasting (i.e., the movement, the proceeding of the billet through the mould) of the billet was maintained constant during the experimentation at a value of
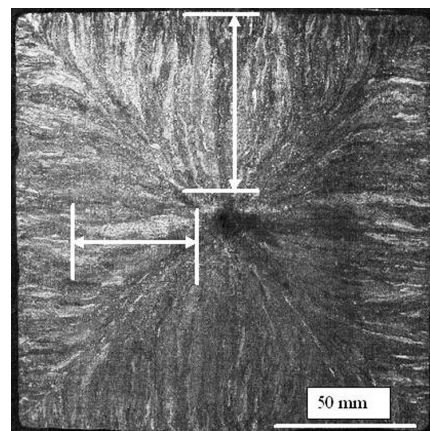

Figure 2: Dendrite growth in the concasting structure without EMS – mode 2A
Slika 2: Rast dendritov v strukturi pri kontinuirnem ulivanju brez EMS – način 2A

2.7 m/min. **Table 2** shows that as many as nine concasting variants were verified. The lengths of individual experimental billets – from which samples had been taken – were always a multiple of the metallurgical length. The average superheating of the steel above the liquidus was (32.8 ± 3.1) °C in melt A and (28.0 ± 4.6) °C in melt B, which lies within the standard deviation of the temperature measurements.

3 EVALUATING EXPERIMENTS

Evaluation of all nine variants of concasting (**Table 2**) indicates that the arrangement of the dendrites in the cross-section follows the same tendency in the first phase of crystallization. The structure is created by columnar crystals – dendrites – perpendicular to the walls of the billet (**Figure 2**). In the billets that were not stirred the dendrites gradually touch one another on the diagonals of the cross-section. Here their growth either ceases, or the dendrites bend in the directions of the diagonals and their growth continues all the way to the centre of the billet. The columnar dendrites that grow from the middle part of the surface maintain their basic orientation – perpendicular to the surface – almost all the way to the centre of the billet. In the central part of the cross-section there is an obvious hollow on all nine macroscopic images. This is most probably a shrinkage. The above-described mechanism of dendrite growth during concasting without stirring is frequently the object of interest (**Figure 2**).

Inside the billets, when using the MEMS stirrer (or both MEMS and SEMS), the kinetics of solidification and dendrite growth is initially the same as without stirring. This also creates columnar dendrites that touch along the diagonals; however, soon their growth ceases close to the surface. Dendrites, which are called equiaxed dendrites, continue to grow – their orientation is more random and only partly directed towards the centre of the billet (**Figure 6**).

It appears that this dendrite growth mechanism manifests itself the most when both stirrers are working simultaneously (**Table 2**: 4A, 4B and 5B). If MEMS and SEMS are working simultaneously, the stirring effect significantly prevents the formation of columnar crystals. If only MEMS is working and SEMS is switched off (1A and 1B), then the prevention of columnar crystals is less evident. The working mode of SEMS alone (modes 3A and 3B) cannot be clearly differentiated from the changes in the dendritic structure in relation to the structure formed without stirring (2A and 2B).

Figure 3 (the macro-ground dendritic structure) shows the depth of the columnar band of dendrites in the direction away from the surface of the billet (**Figure 3** – see arrows) and its value, which (with the simultaneous stirring of MEMS and SEMS) is (23.4 ± 1.8) mm. The same qualified guess was made for the ordinary billet casting (i.e., without stirring). Here, the depth of dendrites can be guessed almost all the way to the central shrinkage at 70 mm (**Figure 2** – see arrows). It is known that additives and impurities during solidification are often concentrated in the points of contact of the growing dendrites, where the maximum of segregated additives and impurities and the greatest probability of technological defects occurs.

In the given case, this undesirable effect can be expected along the diagonals, which have a length of up to 100-to-103 mm towards the central shrinkage. This point of contact of the dendrites during the simultaneous working of SEMS and MEMS is only (29.8 ± 1.9) mm, i.e., 3.4-times less. The central area of the billet containing a hollow as a result of a shrinkage is then filled with dendrites growing into a vacuum (i.e., underpressure) (**Figure 4**).

4 DISCUSSION

Under the assumption that the maximum of defects (i.e., pores, impurities, additives and micro-shrinkages)
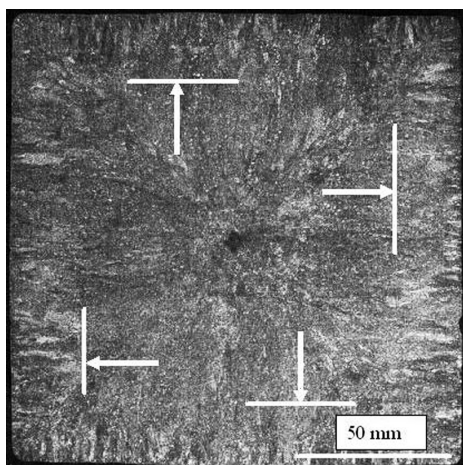

Figure 3: The growth of dendrites in the billet structure using the MEMS and SEMS – mode 4A
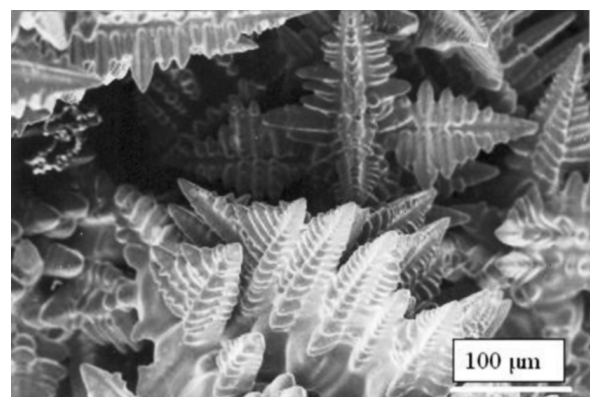**Slika 3:** Rast dendritov v strukturi gredice pri uporabi mešal MEMS in SEMS – način 4A

Figure 4: Dendrites in the centre of the billet
Slika 4: Dendriti v centru gredice

are formed along the diagonals it is possible to expect that in the areas of the corners – specifically on the edges – the nucleation of cracks will be higher than on the walls of the billet. If the first approximation of the fracture toughness of the relevant billet made from low-carbon steel is $K_{IC} \approx 75.0$ MPa m$^{1/2}$, then in the ordinary concasting process it can be assumed that the length of the contact of columnar dendrites along the diagonal will be approximately $\Delta l_{normal} = 101.5$ mm (**Figure 2**). On the other hand, if both electromagnetic stirrers (MEMS and SEMS) are engaged simultaneously, the contact length of the columnar dendrites along the diagonal decreases to $\Delta l_{el.mg} = 29.8$ mm (**Figure 3**). Along these lengths (i.e., the areas) it could be expected that during concasting the concentration of the primary defects will increase where according to the mechanical fracture theory the following equations should apply for the preservation of the continuity of the surface:

$K_{IC} \geq \sigma_{normal} \sqrt{\pi \Delta l_{normal}} \, \varphi(\Delta l_{normal} / w),$

$K_{IC} \geq \sigma_{el.magn.} \sqrt{\pi \Delta l_{el.magn.}} \, \varphi(\Delta l_{el.magn.} / w).$

The first equation applies to normal concasting without EMS and the second to billet casting with both MEMS and SEMS engaged simultaneously. The component $\varphi(\Delta l/w)$ is the shape factor, which in the first approximation could be the same in both equations, thus making it possible to estimate the stress and strain at the peaks of the dendrites touching each other along the diagonals.

$$\sigma_{normal} = \frac{K_{IC}}{\sqrt{\pi \Delta l_{normal}}} = \frac{75}{\sqrt{\pi \cdot 0.0298}} = 245.1 \text{ MPa} \quad (1)$$

which is the limit stress and strain for normal concast billets without EMS, i.e.

$$\sigma_{el.magn.} = \frac{K_{IC}}{\sqrt{\pi \Delta l_{el.magn.}}} = \frac{75}{\sqrt{\pi \cdot 0.1015}} = 132.8 \text{ MPa} \quad (2)$$

which is the limit stress and strain in the area of the edges of the billets during concasting if both, the MEMS and SEMS stirrer, are engaged. A comparison of both limit stresses and strains indicates that the billets (otherwise cast under the same conditions) cast without stirring are almost twice as susceptible to cracking along the edges as billets cast using both stirrers.

A similar assumption can be made even in the case of assessing the effect of columnar dendrites in the central part of the surface of the billet where, without stirring, their length grows from the surface of the wall all the way to the central shrinkage (**Figure 2**), while with the stirrers the dendrites are significantly shorter. The boundaries of the dendrites are, however, much less damaged by technological defects (vacancies, etc.) than the areas of their touching – of the peaks along the

diagonals. Long-term statistical monitoring of the quality of (150 × 150) mm billets and the chemical composition has proven that the application of EMS has significantly reduced the occurrence of defects (in this case, cracks).

5 CONCLUSIONS

This paper introduces the results of a very demanding experimental verification of the effect of electromagnetic stirring (EMS) on the dendritic structure of steel during the concasting of (150 × 150) mm billets. Nine different variants of concasting were verified during ordinary concasting without EMS, with MEMS mounted on the mould, with SEMS mounted in a secondary cooling zone and using both MEMS and SEMS.

Macroscopic grinding was conducted on the samples taken from cross-sections of individual billets in order to make the dendritic structure visible and evaluate it. The greatest effect of the EMS was experimentally observed during the mixing using both MEMS and SEMS simultaneously. The area of the columnar dendrites oriented perpendicular to the surfaces of the walls has a thickness limited to ¼-to-⅓ of the billet thickness. In the remaining central part of billets stirred in this way the structure which dominates is the equiaxed dendrite structure. Long-term statistical monitoring of the quality of billets has proven that the application of EMS reduces the occurrence of defects.

6 REFERENCES

[1] S. Kunstreich: La Revue de Metallurgie CIT, (**2003**), 395–408
[2] S. I. Chung, J. K, Yoon.: Ironmaking and Steelmaking, 23 (**1996**) 5, 425–432
[3] J. Park, H. Kim, H.Jeong, G. Kim, M. J. Cho, J. S. Chung, M. Yoon, K. R. Kim, J. Choi: ISIJ International, 43 (**2003**) 6, 813–819
[4] J. Stetina, F. Kavicka, J. Dobrovska: Mathematical model for the calculation of the temperature field of a billet in real time, Book of Abstracts and CD ROM of the 13th International Heat Transfer Conference, Sydney, Australia, **2006**, p.26
[5] J. Stetina, F. Kavicka, K. Stransky, J. Dobrovska, J. Heger: The numerical and experimental investigation of a concasting process, The Proceedings of the 11th International Conference on Computational Methods and Experimental Measurements CMEM XI, Halkidiki, Greece, **2003**, p.721–730
[6] J. Štětina, F. Kavička, J. Heger: The influence of thermophysical properties on a numerical model of solidification, Proceedings of The 2002 ASME Pressure Vessels and Piping Conference. New York, The American Society of Mechanical Engineers, **2002**, p. 147–152, ISBN 0-7918-1949-3